Highly Ordered Anodic Porous Alumina Formation by Self-Organized Anodizing

1 AUTHOR:

Grzegorz D. Sulka
Jagiellonian University
64 PUBLICATIONS   **1,152** CITATIONS

1
Highly Ordered Anodic Porous Alumina Formation by Self-Organized Anodizing

Grzegorz D. Sulka

1.1
Introduction

Nanotechnology, in combination with surface engineering focused on a fabrication of various nanostructures and new materials, has recently attracted a vast amount of research attention, and has become a subject of intense scientific interest. Particularly, the inexpensive formation of periodically ordered structures (e.g., nanopore, nanotubes and nanowire arrays) with a periodicity lower than 100 nm, has triggered extensive activities in research. The present, huge progress in nanotechnology is a direct result of the modern trend towards the miniaturization of devices and the development of specific instrumentation that could visualize the nanoworld and allow surfaces to be studied at nanoscale resolution. Among various technologies that allow the visualization and characterization of nanomaterials and nanosystems, scanning probe microscopy (SPM) techniques and especially, scanning tunneling microscopy (STM) or atomic force microscopy (AFM), must definitely be quoted [1,2]. Recently, the basis of STM/AFM instrumentation, including a near-field imaging process and the use of piezoelectric actuators, has been successfully adapted to several techniques [3]. Consequently, scanning near-field optical microscopy (SNOM), photon scanning tunneling microscopy (PSTM), magnetic force microscopy (MFM) or scanning thermal profiling (STP) have begun to be used widely, not only for the surface imaging and characterization of materials in nanometer scale but also for providing additional information on surface properties [3].

The strong reduction of the dimensions and precise control of the surface geometry of nanostructured materials has resulted in the occurrence of novel and unique catalytic, electronic, magnetic, optoelectronic and mechanical properties. The unique properties of the nanostructure, or even of an integral functional unit consisting of multiple nanostructures, are the result of the collective behavior and interaction of a group of nano-elements acting together and producing responses of the system as a whole [4]. The potential of highly ordered nanomaterials for future technological applications lies mainly in the field of various nanophotonic,

photocatalytic, microfluidic and sensing devices, as well as functional electrodes and magnetic recording media.

A huge variety of nanodevices based on nanostructured materials has been reported recently in the literature. For instance, two-dimensional (2D) photonic crystals are seriously taken into account as very useful nanostructures used for the construction of various important functional devices [5]. Photonic crystals are periodic dielectric structures having a band gap that prohibits the propagation of a certain frequency range of electromagnetic waves. The integration of photonic crystals made from patterned semiconductor nanostructures with active optoelectronic devices has been studied [6,7]. Photonic crystals have been proposed as mirrors in a single-mode semiconductor laser with small cavity length, and also as a tunable laser with a tuning range of over 30 nm [7]. Recently, three-dimensional (3D) photonic crystals have been prepared by the electrochemical etching of silicon and subsequent pore-widening treatment [8]. The array of nanochannels with a diameter of 30 nm fabricated on silicon can be used for separation, cell encapsulation, and drug release [9]. Silicon nanowires as highly sensitive biosensor devices, allowing the electrical detection of selective adsorption biomolecules, such as specific proteins related to certain types of cancer, has also been reported [10]. Nanoparticles, nanowires and nanotubes have been extensively studied by Vaseashta *et al.* [11] in order to determine their biocompatability and their further possible use in the detection of molecular binding for molecules such as DNA, RNA, proteins, cells, and small molecules. Semiconductor quantum dots (QDs), in conjugation with biomolecules, have been used to produce a new class of fluorescent probes and QD–antibody complexes [12]. These nanoscale semiconductor QDs, which have affinities for binding with selected biological structures, have been used to study the dynamics of various biological processes, including neuronal processes [12]. Self-assembly QDs have also been used for manufacturing a quantum-dot field-effect and quantum-dot memory devices [13]. Electrochemical biosensors with a unique electrocatalytic properties used for electro-analytical purposes have been fabricated on a basis of carbon nanotubes [14–16] and other nanoporous materials [17,18]. Nanoporous, well-ordered materials have been used for gas moisture measurement and the successful fabrication of humidity sensors [19,20]. Currently, there is a great demand in the microelectronics industry for the ideal magnetic medium consisting of a 2D array of ordered islands with nanometer dimensions. Patterned magnetic media fabricated directly by various lithography techniques and regular arrays of magnetic dots and wires obtained by a template synthesis approach have been one of the more widely discussed possibilities for useful devices to extend the density of recording and information storage [21–26]. Magnetic structures have been also used for the fabrication of a nanoscale single domain magnetoresistive bridge sensor, and for a new ultra-high-resolution tip of the magnetic force microscope [27]. A single-electron memory device, in which one bit of information can be stored by one electron [28], an organic photovoltaic device based on polymer nanowires [29], or a fast-response hydrogen sensor based on arrays of palladium wires [30,31] have also been presented. Only limited applications of nanostructured materials for the manufacture of nanodevices have been presented in this chapter. However, major

reviews of various devices based on nanowires, nanotubes and nanoporous materials have been reported in the literature [2,32–36].

Lithography patterning techniques can be used directly to create various nanoparticles, nanowires and nanotubes arranged with highly ordered arrays [37]. By using lithography techniques, all of the processing steps to accomplish the pattern transfer from a mask to a resist and then to devices, can be successfully performed with ultra-high precision, and even nanosize resolution. Lithography techniques can be also employed for the preparation of nanoporous membranes and various templates used for the subsequent deposition of metals [38]. The fabrication of high-ordered nanostructures with the periodicity less than 50 nm is beyond what a conventional optical lithography could afford [39,40]. Advanced non-optic lithographic techniques, such as electron-beam [41–45], ion-beam [46,47], X-ray [48], interference or holographic lithographies [49–51], can replicate patterns with a sufficient resolution of few nanometers, but required sophisticated facilities. Moreover, the high cost of lithographic equipment makes these techniques unavailable to many researchers. Notwithstanding the undeniable advantages of these techniques, certain major drawbacks exist. For example, a low aspect ratio (the ratio of length to diameter) of the formed nanostructure and the high cost of its preparation limit the applications of lithography techniques to the laboratory scale.

Therefore, in order to overcome such drawbacks of conventional lithographic methods, nanoimprint lithography (NIL) as a high-throughput and low-cost method has been developed for fabricating nanometer-scale patterns [52,53]. In nanoimprint lithography, a nanostructured mold is pressed into a resist film existing on a substrate, and in this way a thickness contrast pattern in the resin is created. The duplicated nanostructure in the resist film is then transferred to the substrate by reacting ion etching. Today, the use of this method has rapidly spread quickly and it is now used for the preparation of arrays of various materials [27,54,55].

Among several nanolithographic techniques, scanning probe lithography employing STM and AFM has been considered one of the best tools for atomic level manipulation and forming nanostructures [56–59]. The surface nanostructuring within this method is based on the chemical vapor deposition (CVD) process, local electrodeposition or voltage pulses.

Nanosphere lithography (NSL) employs a hexagonal, close-packed monolayer or bilayer of spheres formed on a supporting substrate (e.g., Au, Si, glass). Spheres on the substrate are arranged by a self-organized process upon solvent evaporation or drying [37,60–62]. Close-packed monolayers of submicron-diameter monodisperse polymer spheres are then formed from a chemical solution spread over the substrate surface. NSL is a simple and inexpensive process which can generate structures even on a curved surface with a high throughput. Self-assembled, hexagonally arranged nano-sized latex, polystyrene or silica spheres have been used as a lithography shadow mask to generate a variety of 2D metal nanoparticle arrays. Au [18], Ni [63], Fe_2O_3 and In_2O_3 [64] hexagonal, close-packed nanoarrays have been obtained by a subsequent deposition or etching through the nanosphere mask. Well-ordered arrays of nanostructures of complex oxides including $BaTiO_3$ and $SrBi_2Ta_2O_9$ has been obtained by NSL in a combination with pulsed laser deposition [65].

Surfaces with periodic structure can be produced by a self-organized process occurring during the ion irradiation of surface, optical or electron-beam lithography, molecular beam epitaxy, arc discharge or evaporation, and laser-focused atomic deposition [22,23,37]. Facets and steps appear spontaneously, or strain relief can create a self-organized nanopattern on the metal or semiconductor surface [22,66–68]. The local periodicity of nanostructure and limited surface area of ordered domains are insuperable disadvantages of the method.

Enormous progress has been made in the preparation of various highly ordered and uniform nanostructures through wet chemical processes employing microemulsion systems, reverse micelles and self-assembled close-packed monolayers or bilayers [23,69,70]. The self-assembled growth of nanoparticles with highly monodisperse diameters or nanowires occurs by the decomposition or reduction of precursors in a solution [71–76], solid matrix [77], and reverse micelles [78]. For example, Co monodisperse nanoparticles with a diameter of 6 nm and self-ordered into spherical superstructures, as well as a hexagonal close-packed self-organized array of $Fe_{50}Pt_{50}$, have been prepared by reduction in solution [71]. The nanoscale patterning and fabrication of nanostructured materials do not necessarily require sophisticated methods and equipment, and remarkable examples of nanoparticles and nanowires synthesis have been presented. Extraordinary hopper- and flower-shaped silver oxide micro- and nanoparticles have been prepared electrochemically by the anodization of silver wires [79]. Ag nanowires have been successfully synthesized from a solution containing surfactant by a simple ultraviolet (UV) photochemical reduction method [80]. Lamellar mono- and bilayers have been used as microreaction matrices to form nanoparticles and nanowires. Selective copper and cobalt deposition on e-beam patterned thiol self-assembled monolayers on a solid support has also been studied [81]. The smallest structures produced in this way were 30 nm-wide Co or Cu lines and 30 nm dots. The ability of surfactants and lipids to form self-assembled monolayers or bilayers on a solid support has been used for the nanostructuring of materials [82,83]. The Langmuir–Blodgett film of surfactant-stabilized Si and SiO_2 nanowires, parallel aligned with a controlled pitch, has been used as a template for the transfer of its arrangement into a chromium substrate over areas up to $20\,cm^2$ [84]. Soft chemical routes based on sol–gel techniques and wet impregnation methods, often with modern modifications, have been employed successfully to synthesize a large number of inorganic nanotubes, nanorods such as: CeO_2, ZrO_2, HfO_2, TiO_2, Al_2O_3 [85–89] and hierarchically ordered mesoporous SiO_2, Ni_2O_5 [90] or nanocomposite materials [91].

Based on the electrochemical techniques used for nanostructure manufacture, a great number of sophisticated nanomaterials have been prepared on various substrates. Highly oriented pyrolytic graphite (HOPG) with a low-energy electrode surface has been used extensively for nanoparticle and nanowire electrodeposition. Monodispersed in size Ni [92,93], Cd, Cu, Au, Pt and MoO_2 nanoparticles [93,94] have been deposited on the HOPG surface. The electrochemical step edge decoration method has been applied for the selective deposition of metal at step edges existing at HOPG. A great variety of nanomaterials, including Mo [95,96], Cu, Ni, Au, Ag, Pd [97–102], MoO_2 [95,96], MnO_2 [103], MoS_2 [104], Bi_2Te_3 [105] nanowires,

3D Co nanocrystal array [106], Ag nanoflakes and nanorods [107], have been prepared using this method. The synthesis of nanostructures through electrochemical means has also been studied on different substrates. Copper nanowires with a diameter of between 10 and 20 nm have been prepared on a glass substrate covered with a thin layer of CuI under a direct current electric field [108]. Spontaneous displacement reactions have been successfully employed for electroless Ag deposition into patterned Si [109], Pt, Pd, Cu and Ag on a HOPG surface with crystals of a ferrocene derivative [110], and Cu on AlN substrate with a patterned copper seed layer [111].

A template synthesis has recently proved to be an elegant, inexpensive and technologically simple approach for the fabrication of various nanoscale sophisticated materials. These alternative methods overcome many of the drawbacks of lithographic techniques, and exploit templates which differ in material, pattern, range of order and periodicity, feature size and overall size of templates. Templating methods employing a variety of porous membranes and films are commonly used for the synthesis of high-density, ordered arrays of nanodots, nanotubes and nanowires. Recently, scientific attention has been focused on two types of template: track-etched polymeric and porous alumina membranes [36]. Although the origin of the template, used for nanofabrication, may also be lithographic, the high cost of its preparation drastically limits the applications. Although the aspect ratio achievable is not high, lithographically prepared templates have the undeniable advantage of exploiting a much wider spectrum of substrate choice than do porous membranes. The most significant drawback of membrane-templating methods is a poor long-range order in the formed nanostructure, even though a short-range order is maintained satisfactorily. Nickel nanowire arrays have been prepared by electrodeposition into the porous single-crystal mica template with a uniform size of pores and orientation [112,113]. Mesoporous thin films (MTFs) as templates have been used for the successful synthesis of ordered arrays of Ge [114], Co and Fe_3O_4 [115] nanowires. Cobalt dots [116,117], monodisperse Au microwire arrays [118] and Sn nanotubes [119] have also been deposited on the porous silicon substrate. During the past decade, an enormous variety of metallic nanowires has been synthesized electrochemically within the pores of the nuclear track-etched polycarbonate membrane. Since it has been discovered that the deposition of materials in porous membranes proceeds preferentially on the pore walls [120,121], polycarbonate membranes are widely used for the fabrication of Co [122–132], Ni [122,133,134], Cu [124,134,135], Pb [136] nanowires, ferromagnetic NiFe [133,137] or CoNiFe [137] nanowire arrays and Co/Cu [124,138–142], NiFe/Cu [138,140–143], Ag/Co [144] multilayered nanowires. An electrochemical deposition method using the polycarbonate membrane, has been also employed for a successful preparation of Co, Fe, Ni [145], Bi [146] rods, conducting polypyrrole nanotubes and polypyrrole–copper nanocomposites [146]. The physical process of solvent volatilization from the polycarbonate membrane filled with an appropriate solution has been used for the synthesis of manganite oxide-based ($La_{0.325}Pr_{0.300}Ca_{0.375}MnO_3$) nanowires and nanotubes [147]. Cobalt nanoparticles with a very fine diameter of 3.5 nm have been synthesized in the perfluorinated sulfo-cation exchange polymeric membrane by using the ion-exchange

method [148]. Recently, ordered thin films of diblock copolymer have been used to fabricate periodic arrays of holes with nanometer dimensions [46,149–151]. The template strategy employing a thin film of the self-assembly diblock copolymer in combination with electrodeposition, has been used to prepare Co nanowires with a diameter of 12 or 24 nm [152] and highly ordered nanoelectrode arrays [153]. The concept of using anodic porous alumina membranes as templates for fabrication-ordered nanowire and nanotube arrays seems to be the most widespread among research groups, and will be discussed in Section 1.5.

A considerable effort has been also placed on developing alternative nanopatterning methods. For example, a variety of methods have been developed for the fabrication of ordered structures on a nanometer length scale, including physical vapor deposition (PVD) [154,155], catalyzed vapor-phase transport processes [156,157], CVD based on the vapor–liquid–solid (VLS) growth mechanism [4,36,158], a direct self-assembly route that exploits a mask with protruding patterns [159], laser-assisted direct imprinting [160], self-patterning methods based on the instability of ultrathin films during a high-temperature treatment [161], and template synthesis in conjunction with the pressure injection filling technique [36]. An extraordinarily novel method based on the unidirectional solidification of monotectic alloys such as Al–In and NiAl–Re and subsequent electrochemical etching has been developed for the preparation of Al and NiAl nanoporous arrays [162–164].

1.2
Anodizing of Aluminum and Anodic Porous Alumina Structure

Currently, much effort has been undertaken to develop an effective and technologically simple method used for the synthesis of nanostructures over a macroscopic surface area. Today, the research spotlight is especially focused on self-organized nanostructured materials with a periodic arrangement of nanopores due to the high expectations regarding their applications. A highly desired densely packed hexagonal array nanoporous structure can be obtained by anodization, which is a relatively easy process for nanostructured material fabrication. The electrochemical formation of self-organized nanoporous structures produced by the anodic oxidation of semiconductors or metals, except aluminum, has been reported for only a few materials such as Si [165–172], InP [173,174], Ti [175–183], Zr [181,184–186], Nb [187–190], Hf [191] and Sn [192]. During recent years, the anodization of aluminum, due to its great commercial significance, represents one of the most important and widespread method used for the synthesis of ordered nanostructures consisting of close-packed cells in a hexagonal arrangement with nanopores at their centers.

Over the past decades, the anodizing of aluminum has raised substantial scientific and technological interest due to its diverse applications which include dielectric film production for use in electrolytic capacitors, increasing the oxidation resistance of materials, decorative layers by incorporation of organic or metallic pigments during the sealing of anodized materials, and increasing abrasion wear resistance

[193–196]. Recently, a self-organized process that occurs during the anodization of aluminum in acidic electrolytes has became one of the most frequently employed method for the synthesis of highly ordered nanostructures.

1.2.1
Types of Anodic Oxide Film

In general, the anodizing of aluminum can result in two different types of oxide film: a barrier-type anodic film, and a porous oxide film. It was generally accepted that the nature of an electrolyte used for anodizing aluminum is a key factor which determines the type of oxide grown on the surface [197–199]. Recent progress in the anodizing of aluminum in various media highlights the depth of the problem of electrolyte influence on porous oxide layer formation. The capability of porous anodic oxide development from the initially formed barrier-type film was reported elsewhere [200–204]. Nevertheless, it has long been believed that a strongly adherent, non-porous and non-conducting barrier-type of anodic film on aluminum can be formed by anodizing in neutral solutions (pH = 5–7) in which the anodic oxide layer is not chemically affected and stays practically insoluble. These films are extremely thin and dielectrically compact. The group of electrolytes used for this barrier-type film formation includes boric acid, ammonium borate, ammonium tartrate and aqueous phosphate solutions, as well as tetraborate in ethylene glycol, perchloric acid with ethanol and some organic electrolytes such as citric, malic, succinic, and glycolic acids [200,202,205,206]. Recently, a compact, and dense anodic oxide layer has been obtained by the anodization of aluminum in 5-sulfosalicylic acid [207]. In contrast, porous oxide films were reported mainly for the anodizing of aluminum in strongly acidic electrolytes, such as sulfuric, oxalic, phosphoric and chromic acid solutions, where the resulting oxide film can be only sparingly soluble [197,208]. For anodic porous alumina, the film growth is associated with localized dissolution of the oxide, as a result of which pores are formed in the oxide film. However, the porous anodic layer formation has been recently reported for various acidic electrolytes such as malonic [209–211], tartaric [211–213], citric [214–217], malic [213], glycolic [213] and even chromic acid [218]. Anodic porous oxide films have been also obtained in unpopular electrolytes, including a mixed solution of phosphoric and organic acids with cerium salt [219], or in a mixture of oxalic acid, sodium tungstate, phosphoric and hypophosphorous acids [220]. The porous oxide film was also observed for anodization carried out in a fluoride-containing oxalic acid electrolyte [221]. The formation of nanopores by self-organized anodization has also been studied in a mixture of sulfuric and oxalic acids [222]. In fact, these results show that is no distinct difference in the selection of an electrolyte used for the formation of barrier or porous films during the anodization of aluminum. Moreover, the transition from a barrier-type film to porous oxide occurs easily. The anodizing time is a key factor responsible for the development of porous oxide structure on previously formed barrier-type film [202,222]. Some excellent reviews on barrier-type oxide films have been produced [200,202,203,205], whilst details of the porous oxide layers are reported elsewhere [195,198,200,202,203,205,208,224]. The porous

oxide film formation resulting in a self-organized, highly ordered nanopore array is one subject of this chapter.

The anodic behavior of aluminum in electrolytes used for anodizing is not limited to the formation of a barrier-type film or a porous oxide layer. A fiber-like porous oxide morphology has been reported for the anodization of aluminum in chromic [225] and sulfuric acid [213,226]. The completely different morphology of the oxide layer formed by anodizing in oxalic or sulfuric acid has been observed by Palibroda *et al.* [227]. A cross-sectional view of an anodized layer exhibits hemispherical and spherical patterns that appear during anodization as a result of simultaneous gas evolution and the formation of a gel-like, nascent oxide. In addition, other anodic behaviors such as localized pitting corrosion in monobasic carboxylic acids (e.g., formic, acetic) [200] and in the presence of halide ions [200,202,228,229], burning [211,216,230] or crystallographic dissolution [231] have also been reported.

1.2.2
General Structure of Anodic Porous Alumina

The specific nature of a porous oxide layer on aluminum has attracted scientific attention over several decades, and determined fully the present applications of anodized aluminum in nanotechnology. Self-organized anodic porous alumina grown by the anodization of aluminum can be represented schematically as a closed-packed array of hexagonally arranged cells containing pores in each cell-center (Figure 1.1). High-ordered nanostructures are often characterized by given parameters such as a pore diameter, wall thickness, barrier layer thickness and interpore distance (cell diameter). The uniform pore diameter, which is easily controllably by altering the anodizing conditions, can range from a few nanometers to hundreds of nanometers. The depth of fine parallel channels can even exceed $100\,\mu m$, a characteristic which makes anodic porous alumina one of the most desired nanostructures with a high aspect ratio and high pore density. A parallel growth of controlled dimensional pores can proceed throughout the complete anodized material.
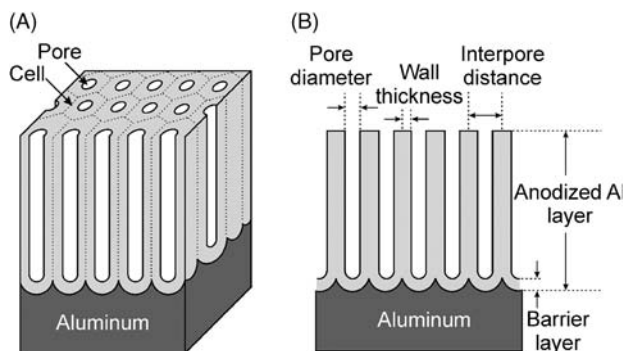

Figure 1.1 Idealized structure of anodic porous alumina (A) and a cross-sectional view of the anodized layer (B).

Growth of the oxide layer takes place at the metal/oxide interface at the pore bottoms, and involves the conversion of a preexisting, naturally occurring film on the surface into the barrier-type film and further into a porous oxide layer. During the porous oxide growth, a thin and compact barrier layer at the pore bottom/electrolyte interface is continuously dissolved by locally increased field, and a new barrier layer at the metal/oxide interface is rebuilt. For steady-state film growth, there is a dynamic equilibrium between the rate of film growth and its field-assisted dissolution. All of the major anodic film parameters are directly dependent on forming a voltage attendant, steady-state growth of the porous oxide layer. During the steady state of oxide growth, current density under potentiostatic anodizing or anodizing potential under galvanostatic anodizing remains almost unchanged. The cylindrical, insection pores appear as a result of such steady-state growth.

1.2.2.1 Pore Diameter

Generally, for the anodic porous alumina structure, the pore diameter is linearly proportional to the anodizing potential with a proportionality constant λ_p of approximately 1.29 nm V^{-1} [208]:

$$D_p = \lambda_p \cdot U \tag{1}$$

where D_p is a pore diameter (nm) and U denotes an anodizing potential (V). The dependence of the diameter on the voltage is not sensitive to the electrolyte. In describing the anodic porous alumina structure, researchers usually list the outer layer of oxide close to the surface, and the inner layer close to the pore bottoms. The diameter of pores in the inner oxide layer does not change significantly with anodizing time [197,203]. A higher diameter of pores observed in a region close to the film surface is the result of an irregular initial growth of the pores during the very early stages of pore development, and their further reorganization in an hexagonal arrangement. It should be noted that an enhanced chemical dissolution of oxide, resulting in the development of widened pores, may occur also during anodizing at a sufficiently high temperature, or in strong acidic solutions [200,203]. The solvent chemical action along the cell walls, and especially in the outer oxide layer, increases the diameter of pores measured at the surface of the anodic film [232].

During the early stage of collecting research data concerning the structure of anodic porous alumina, it was believed that pore diameter was independent of the forming potential [197]. However, later studies have reported the pore diameter as a parameter which depends upon the anodizing potential or current density [233]. According to O'Sullivan and Wood [208], the pore diameter for anodizations conducted at a constant anodizing potential can be calculated as follows:

$$D_p = D_c - 2 \cdot W = D_c - 1.42 \cdot B = D_c - 2 \cdot W_U \cdot U \tag{2}$$

where D_c is the cell diameter, interpore distance (nm), W is the wall thickness (nm), B is the barrier layer thickness (nm), and W_U is the wall thickness per volt (nm/V).

For potentiostatic conditions of anodization, wall thickness divided by the anodizing voltage gives the thickness of oxide-wall per applied volt (W_U). The empirical dependence of pore diameter on the anodizing potential or the ratio of anodizing potential to a critical value of the potential (U_{max}) has been reported by Palibroda [234]:

$$D_p = 4.986 + 0.709 \cdot U = 3.64 + 18.89 \cdot \frac{U}{U_{max}} \qquad (3)$$

The critical potential is an experimentally determined maximum anodizing potential which can be applied during anodization, without triggering intense gas evolution on the aluminum. In describing a 10% porosity rule, Nielsch *et al.* [235] suggested that a diameter of pores formed by the anodizing aluminum under optimum self-ordering conditions, leading to a quasiperfect hexagonal arrangement of pores, can be calculated from the following equation:

$$D_p = \sqrt{\frac{2\sqrt{3} \cdot P}{\pi} k \cdot U} \qquad (4)$$

where P is porosity ($P = 0.1 = 10\%$) and k is the proportionality constant ($k \cong 2.5$).

Obviously, the temperature of the electrolyte and the hydrodynamics conditions in the electrolytic cell affects the pore diameter. At higher temperatures of anodizing (e.g., near room temperature) a significant acceleration of chemical dissolution of the outer oxide layer, especially in a strong acidic solution is expected. On the other hand, stirring of the electrolyte during anodizing under the constant anodizing potential causes a significant increase in the local temperature at the inner oxide layer, and the recorded current density increases [236]. As a result of the increasing local temperature, a chemical dissolution of oxide in the inner layer, as well as the electrochemical formation of anodic oxide layer, are accelerated. The effect of electrolyte stirring on a pore diameter is shown schematically in Figure 1.2.

These experimental data show that the effect of electrolyte temperature and electrolyte concentration on pore diameter can be totally different for potentiostatic and galvanostatic conditions of anodizing [208,237,238]. For instance, the pore
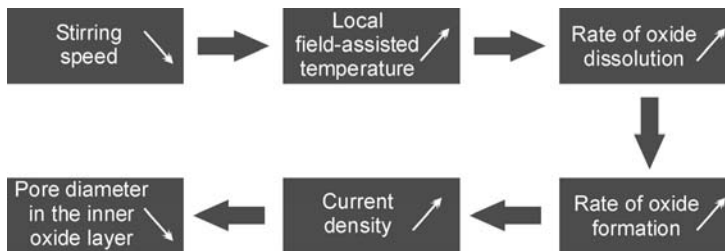

Figure 1.2 Effect of stirring on the pore diameter of nanostructures obtained by anodization of aluminum.

Table 1.1 Relationship between pore diameter and potential for anodization conducted in 2.4 M H_2SO_4 at various anodizing temperatures [240].

Potential range (V)	Temperature ($^\circ$C)	$D_c = f(U)$ (nm)
15–25	−8	$1.06 + 0.80 \cdot U$
	1	$12.35 + 0.53 \cdot U$
	10	$9.34 + 0.72 \cdot U$

diameter has been found to depend on temperature for the constant potential anodizing in a phosphoric acid solution [208]. With increasing temperature of the electrolyte, an increase in pore diameter in the outer oxide layer has been noted. At the same time, a decrease in pore diameter in the inner oxide layer has been observed. It was found that the concentration of electrolyte does not significantly influence the pore diameter [208], although more recently it has been suggested that the pore diameter decreases with decreasing pH of the solution [239] and temperature [240]. A decrease in pore diameter with increasing concentration of the acidic electrolyte or decreasing pH can be attributed to the decreasing threshold potential for a field-assisted dissolution of oxide at pore bottoms, resulting in an enhanced rate of anodic oxide formation [235]. The temperature influence on the pore diameter has been reported recently in detail for sulfuric acid [240]. The linear relationships have been established for a variety of anodizing temperatures (Table 1.1).

A summary of the influence of anodizing parameters on the pore diameter of a nanostructure formed under potentiostatic conditions is presented schematically in Figure 1.3.

When anodizing under a galvanostatic regime, the pore diameter is affected by current density, electrolyte temperature, and acid concentration. As might be
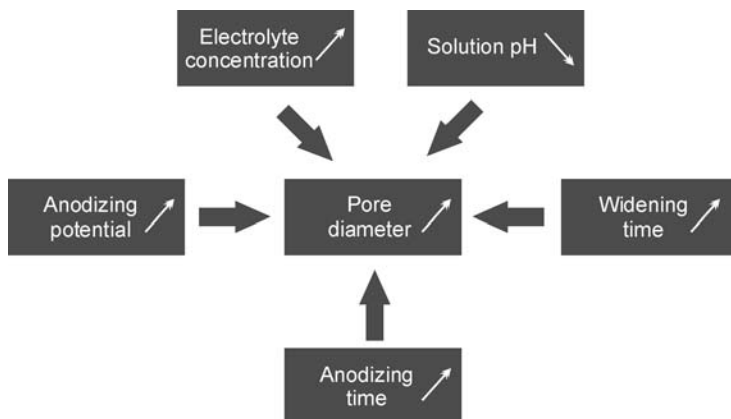

Figure 1.3 Parameters influence on the pore diameter of nanostructure formed by anodization of aluminum at potentiostatic regime.

expected, with increasing current density the pore diameter increases [233]. An increase in the temperature of phosphoric acid, when used as an electrolyte, results in a decrease in the pore diameter measured in the inner oxide layer, although only slight changes in pore diameter are observed in the outer oxide layer [208]. Additionally, the pore diameter decreases with increasing concentration of phosphoric acid. On the other hand, there was no observable evidence of the influence of anodizing temperature on pore diameter for anodization conducted in oxalic and sulfuric acids [237,238]. The final pore diameter of the nanostructure formed by the anodization of aluminum is a superposition of those parameters influences. Therefore, a significant variation in pore diameter determined for similar anodizing conditions and electrolytes is reported in the literature.

1.2.2.2 Interpore Distance

It is generally accepted that the interpore distance of anodic porous alumina is linearly proportional to the forming potential of the steady-state growth of anodic porous alumina with a proportionality constant λ_c of approximately $2.5 \, \text{nm} \, \text{V}^{-1}$ [235]:

$$D_c = \lambda_c \cdot U \tag{5}$$

According to Keller *et al.* [197], the cell diameter can be calculated precisely from the following equation:

$$D_c = 2 \cdot W + D_p = 2 \cdot W_U \cdot U + D_p \tag{6}$$

The linear dependence of interpore distance on anodizing potential is assumed on the hypothesis that pore diameter is independent of anodizing voltage. O'Sullivan and Wood [208] have found that the wall thickness is about 71% of the barrier layer thickness. Taking into account this fact, the following expression can be proposed:

$$D_c = 1.42 \cdot B + D_p \tag{7}$$

An in-depth study of aluminum anodization in sulfuric and oxalic acid has been conducted by Ebihara *et al.* [237,238]. Experimental equations describing the relationship between the interpore distance and anodizing potentials have been established as follows:

$$H_2SO_4 \, [238]: \quad D_c = 12.1 + 1.99 \cdot U \quad (U = 3-18 \, \text{V}) \tag{8}$$

$$C_2H_2O_4 \, [237]: \quad D_c = 14.5 + 2.00 \cdot U \quad (U \leq 20 \, \text{V}) \tag{9}$$

$$D_c = -1.70 + 2.81 \cdot U \quad (U \geq 20 \, \text{V}) \tag{10}$$

The dependence of anodizing potential on interpore distance has been observed by Hwang *et al.* [241]. For anodization in oxalic acid conducted under anodizing

Table 1.2 Relationship between interpore distance and potential
for anodization conducted in 2.4 M H_2SO_4 at various anodizing
temperatures [240].

Potential range (V)	Temperature (°C)	$D_c = f(U)$ (nm)
15–25	−8	$12.23 + 1.84 \cdot U$
	1	$12.20 + 2.10 \cdot U$
	10	$12.72 + 1.87 \cdot U$

potential ranges between 20 and 60 V, the linear equation can be expressed as
follows:

$$D_c = -5.2 + 2.75 \cdot U \tag{11}$$

The interpore distance has been found to be slightly dependent or independent on
the temperature of anodization at the constant anodizing potential regime [208]. For
anodizing carried out in oxalic acid, the interpore diameter has been found to be
independent of the electrolyte temperature [241]. Contrary to this, for self-organized
anodizing in sulfuric acid, an influence of temperature on interpore distance has
been observed [240]. For the highest studied temperature of anodization, 10 °C, the
calculated interpore distance increased by about 8–10% in comparison to that at a
temperature of 1 or −8 °C. Equations describing the interpore distance as a function
of anodizing potential are collected in Table 1.2 for a variety of temperatures.

The study performed by O'Sullivan and Wood [208] showed that increasing the
concentration of electrolyte decreases the interpore distance. In the case when anod-
izing is carried out in phosphoric acid at constant current density, increasing the
temperature of anodizing as well as increasing the electrolyte concentration causes a
decrease in the interpore distance in nanostructures [208]. An unchanged cell size was
observed when anodizing was conducted in phosphoric and oxalic acids [237,238].

The interpore distance can be also calculated from 2D Fourier transforms of
anodic alumina triangular lattice. The 2D Fourier transform provides unique infor-
mation about the structure periodicity in the inverse space. According to Marchal
and Demé [242], the interpore distance for the triangular lattice with the hexagonal
arrangement of nanopores can be calculated from the following expression:

$$D_c = \frac{4\pi}{\sqrt{3} \cdot Q_{10}} \tag{12}$$

where Q_{10} is the position of the first Bragg reflection of the hexagonal arrangement
of nanopores.

1.2.2.3 Wall Thickness

Among other morphological features of anodic porous oxide described by Keller
et al. [197], a wall thickness per volt for some acidic electrolytes frequently used for
anodization of aluminum (Table 1.3) appears to be of importance.

Table 1.3 Wall thickness per volt for various anodizing electrolytes [197].

Electrolyte	0.42 M H_3PO_4	0.22 M $H_2C_2O_4$	1.7 M H_2SO_4	0.35 M H_2CrO_4
Anodizing temperature (°C)	24	24	10	38
Wall thickness per volt (nm V^{-1})	1.00	0.97	0.80	1.09

The transformation of Eq. (1) gives the following form for the wall thickness calculation:

$$W = \frac{D_c - D_p}{2} \tag{13}$$

According to O'Sullivan and Wood [208], the wall thickness built during anodizing in phosphoric acid is related to the barrier layer thickness as follows:

$$W = 0.71 \cdot B \tag{14}$$

For anodization conducted in the oxalic acid solution, Ebihara *et al.* [237] found that the proportionality between wall thickness and barrier layer thickness varies slightly with anodizing potential in the range of 5 to 40 V. For anodizing potentials between 5 and 20 V, a relationship between W and B with a proportionality constant of about 0.66 has been observed, while for higher anodizing potential a gradual increase in the proportionality constant to the final value of about 0.89 has been reported.

1.2.2.4 Barrier Layer Thickness

During the anodization of aluminum, a very thin, dense and compact dielectric layer is formed at pore bases. The barrier layer has the same nature as an oxide film formed naturally in the atmosphere, and allows the passage of current only due to existing faults in its structure. The existing compact barrier layer at the pore bottoms makes the electrochemical deposition of metals into pores almost impossible. On account of this limit, the thickness of the barrier layer is extremely important and can determine any further applications of nanostructures formed by the anodization of aluminum. The thickness of the barrier layer depends directly on the anodizing potential. The dependence is about 1.3–1.4 nm V^{-1} for barrier-type coatings, and 1.15 nm V^{-1} for porous structures [195].

Some variations have been reported in the barrier layer thickness with anodizing potential or the concentration of electrolyte. Evidence of experimental values of B_U, known as an anodizing ratio and defined as a ratio between the thickness of the barrier layer and anodizing potential, are listed in Table 1.4 for a variety of electrolytes.

An inspection of the data in Table 1.4 shows that variation of the barrier layer thickness per volt depends on whether oxide films are formed at a constant potential or at constant current density regimes [208]. The increasing temperature

Table 1.4 Anodizing ratio (B_U) for various anodizing electrolytes.

Electrolyte	Current density[a] ($mA\,cm^{-2}$) or anodizing potential[b] (V)	Concentration (M)	Temperature (°C)	B_U ($nm\,V^{-1}$)	Reference(s)
H_3PO_4	100^a; 80^b	0.4 (3.8%)	20	0.89^a; 1.14^b	[208]
			25	0.90^a; 1.09^b	
			30	1.05^a; 1.04^b	
		1.5 (13%)	25	1.10^a; 1.04^b	
		2.5 (21%)		1.17^a; 0.82^b	
	$(20-60)^b$	0.42 (4%)	24	1.19^b	[197,243]
	87^b		25	0.99^b	[232]
	103^b			0.96^b	
	117.5^b			1.08^b	
	87^b	1.70 (15%)		0.99^b	
	87^b	3.10 (25%)		0.97^b	
$H_2C_2O_4$	$(20-60)^b$	0.22 (2%)	24	1.18^b	[197,243]
	3^b	0.45 (4%)	30	1.66^b	[237]
	10^b			1.40^b	
	20^b			1.19^b	
	30^b			1.10^b	
	40^b			1.06^b	
H_2SO_4	15^b	1.70 (15%)	10	1.00	[243]
		1.10 (10%)	21	1.00^b	[244]
		1.70 (15%)		0.95^b	
		5.6–9.4 (40–60%)		0.80^b	
		12.8 (75%)		0.95^b	
		16.5 (90%)		0.10^b	
	3^b	2.0 (17%)	20	1.45^b	[238]
	10^b			1.23^b	
	15^b			1.05^b	
	18^b			0.92^b	
H_2CrO_4	$(20-60)^b$	0.26 (3%)	38	1.25^b	[244]
$Na_2B_4O_7$	60^b	0.25 (pH = 9.2)	60	1.3^b	[201]
$(NH_4)_2C_4H_4O_6$	$(25-100)^b$	0.17 (3%, pH = 7.0)	–	1.26^b	[223]
Citric acid	$(260-450)^b$	0.125	21	1.1^b	[217]

[a]Constant current density anodizing.
[b]Constant potential anodizing.

of anodization decreases the thickness of the barrier layer for anodizing at the constant potential. An opposite relationship is observed, however, for the constant current density anodization. The increasing concentration of phosphoric acid at the constant temperature either decreases or increases the barrier layer thickness for the potentiostatic or galvanostatic anodizing regime, respectively. This can be attributed

to the fact that, at constant current density, a constant electric field is maintained across the given barrier layer. The increasing thickness of the barrier layer with increasing electrolyte concentration suggests that ionic conduction becomes easier under the set current density, and that most of the ionic current passes through microcrystallites in the barrier layer. On the other hand, the observed decrease in barrier layer thickness with increasing electrolyte concentration and anodizing temperature is a direct result of an enhanced field-assisted dissolution of oxide at the oxide/electrolyte interface.

Recently, the barrier layer thickness has been determined for other less-popular anodizing electrolytes such as glycolic, tartaric, malic and citric acids [213]. The effect of anodizing potential on the thickness of the barrier layer for the anodic porous alumina formed in various electrolytes is shown in Figure 1.4.

In general, the anodizing ratio (B_U) determined for various anodizing electrolytes is very close to $1\,\mathrm{nm\,V}^{-1}$ (the diagonal, dotted line in Figure 1.4) over the whole range of anodizing potential. These results suggest a general constant relationship between the anodizing ratio and anodizing potential.

Nielsch *et al.* [235] suggested that for optimum self-ordering conditions of anodizing, leading to a 10% porosity of the nanostructure and perfect hexagonal arrangement of nanopores, the barrier layer thickness is proportional to the interpore distance as follows:
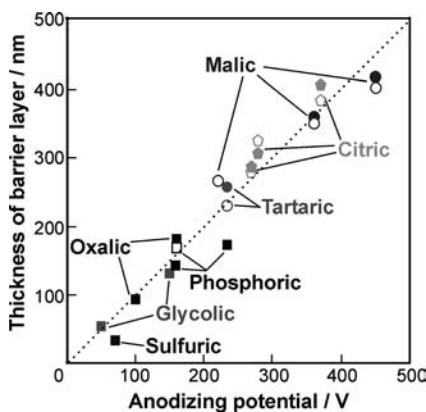
$$B \cong \frac{D_c}{2} \tag{15}$$

Figure 1.4 Anodizing potential influence on the barrier layer thickness for anodic porous alumina formed in sulfuric, oxalic, glycolic, phosphoric, tartaric, malic, and citric acid solutions. (Solid symbols: measured values; open symbols: calculated values from the half-thickness of the pore walls). (Reproduced with permission from Ref. [213], © 2006, The Electrochemical Society.)

Table 1.5 Effect of anodizing potential on the barrier layer thickness formed at 20 °C.

Electrolyte	Anodizing potential (V)	$B = f(U)$ (nm)	Reference
Potentiostatic anodising			
0.42 M H_3PO_4	$U < 38$	$0.28 + 1.10 \cdot U$	[245]
	$U > 38$	$1.58 + 1.03 \cdot U$	
0.45 M $H_2C_2O_4$	$U < 57$	$5.90 + 0.90 \cdot U$	[246]
	$U > 57$	$0.96 + 0.97 \cdot U$	
Galvanostatic anodising			
0.45 M $H_2C_2O_4$	$U < 55$	$0.92 + 1.09 \cdot U$	[247]
	$U \geq 55$	$5.02 + 0.92 \cdot U$	

Recently, Vrublevsky *et al.* [245–247] reported empirical equations used for calculating the barrier layer thickness in anodic alumina formed by anodizing in 0.42 M H_3PO_4 and 0.45 M $C_2H_2O_4$ solutions. By using a re-anodizing technique and assuming that the anodizing ratio equals 1.14 nm V^{-1}, the thickness of the barrier layer has been evaluated for anodic film formation at 20 °C. The equations expressing the thickness of the barrier layer as a function of anodizing potential, $B = f(U)$, are presented in Table 1.5.

The wall thickness, as well as the barrier layer thickness, in nanostructures formed by anodization can be easily altered by post-treatment procedures involving chemical etching; this is known as a process of isotropic pore widening.

1.2.2.5 Porosity

The porosity of nanostructures formed by aluminum anodizing depends heavily on the rate of oxide growth, the rate of chemical dissolution of oxide in acidic electrolyte, and anodizing conditions such as: the type of electrolyte, the concentration of electrolyte, time of anodization, anodizing potential, and temperature. The most important factor governing the porosity of the structure is the anodizing potential and pH of the solution. There is a great inconsistency among experimental data on the porosity of nanostructures, with the estimated porosity of anodic porous alumina varying from about 8% to 30%, and even more. An exponential decrease in porosity with increasing anodization potential has been reported for anodizing in sulfuric acid [238,248] and oxalic acid [237]. A decrease in the porosity of nanostructures with increasing anodizing potential has been observed for constant potential anodizations conducted in sulfuric, oxalic, phosphoric, and chromic acids [216,249,250]. On the other hand, a slight increase in porosity is observed with increasing anodizing potential for anodization carried out in sulfuric acid [251]. As might be expected, the porosity of nanostructures may also be affected by the anodizing time, an extension of which usually results in increasing porosity of the nanostructure formed in tetraborate [201] and phosphoric acid [252] solutions. Increasing the anodizing temperature decreases the porosity of the nanostructure formed in oxalic acid [253]; the opposite effect has been observed in sulfuric acid [240].

The porosity is defined as a ratio of a surface area occupied by pores to the whole surface area. For a single regular hexagon with one pore inside, the porosity formulation can be written as follows:

$$\alpha = \frac{S_{pores}}{S} = \frac{S_p}{S_h} \tag{16}$$

Assuming that each single pore is a perfect circle, the following equations for S_p and S_h can be further evolved:

$$S_p = \pi \cdot \left(\frac{D_p}{2}\right)^2 \tag{17}$$

$$S_h = \frac{\sqrt{3} \cdot D_c^2}{2} \tag{18}$$

Substitution of Eqs. (17) and (18) into Eq. (16) leads to the following expression for the porosity of a nanostructure with hexagonally arranged cells:

$$\alpha = \frac{\pi}{2\sqrt{3}} \cdot \left(\frac{D_p}{D_c}\right)^2 = 0.907 \cdot \left(\frac{D_p}{D_c}\right)^2 \tag{19}$$

The porosity of the hexagonally arranged nanostructure can be also calculated from the expression given by Ebihara *et al.* [237,238]:

$$\alpha = 10^{-14} n \cdot \pi \cdot \left(\frac{D_p}{2}\right)^2 \tag{20}$$

where n is a pore density (1 cm^{-2}) being an overall number of pores per cm^2 and D_p is a pore diameter (in nm).

Nielsch *et al.* [235] reported that, for a perfect hexagonal arrangement of nanopores formed by self-organized anodization under optimum anodizing conditions, the ratio between pore diameter and interpore distance is almost constant and is equal to ~0.33–0.34. Consequently, the optimum porosity for the best chosen anodizing conditions should be 10%. The optimal anodizing conditions depend mainly on the applied anodizing potential; for anodizing conducted in sulfuric, oxalic and phosphoric acids, the anodizing potentials that guarantee the perfect hexagonal order in a nanostructure are limited to values of 25, 40, and 195 V, respectively. The applied anodizing potential (which is different from the optimal value for a certain electrolyte) results in a significantly larger or smaller porosity of the nanostructure. The porosity rule has been derived only for self-ordering of alumina at the optimum anodizing conditions. In general, the self-organized anodic porous alumina requires a porosity of 10% independently of the anodizing potential, type of electrolyte and anodizing conditions.

Taking into account the ratio of pore diameter to cell diameter as a constant value for the self-ordering anodizing, Ono *et al.* [216,249,250] have suggested the following expression for porosity:

$$\alpha = \left(\frac{D_p}{D_c}\right)^2 \tag{21}$$

Most importantly, it should be noted that the relationship in Eq. (21) is only a rough approximation of Eq. (19) with a conceptual error of about 10%.

A different equation for porosity has been proposed by Bocchetta *et al.* [253]:

$$\alpha = \frac{S_{pores}}{S} = \frac{S - S_{ox}}{S} = 1 - \frac{m_p}{\rho h S} \tag{22}$$

where S_{ox} is the oxide surface, and m_p, h and ρ are the mass, thickness, and density of the porous layer, respectively. The density of anodic porous alumina formed by anodizing at 70 V in 0.15 M oxalic acid has been estimated at $3.25\,\mathrm{g\,cm^{-3}}$. A wide variety of experimental values of porosity result from the different anodizing conditions used, in addition to the problem of completely different equations being used for the calculation.

It was mentioned previously that pore diameter can be altered by the widening process, which is based on the chemical etching of porous alumina walls in acidic solutions. A very interesting formula has been proposed for the porosity of nanostructure formed by anodizing in 0.42 M phosphoric acid at 140 V and 20 °C [252]. After anodization, the pores were widened in a 2.4 M H_2SO_4 solution at 20 °C, with the widening time being varied from 60 to 300 min:

$$\begin{aligned}\alpha = {}&0.196 + 6.54{\cdot}10^{-4}t_a + 2.62{\cdot}10^{-4}t_w + 7.27{\cdot}10^{-7}t_a^2 \\ &+ 4.36{\cdot}10^{-7}t_a t_w + 8.73{\cdot}10^{-8}t_w^2\end{aligned} \tag{23}$$

where t_a (min) and t_w (min) denote the anodization time and widening time, respectively.

1.2.2.6 Pore Density

The highly ordered nanomaterial with a close-packed arrangement of nanopores or nanotubes is seen as an "object of desire" for the microelectronics industry. Due to the hexagonal symmetry of the cells, anodic porous alumina is a nanostructure with the highest packing density, and consequently the number of pores created during anodization represents one of the most important features of porous alumina.

For the hexagonal distribution of cells in the nanostructure, the density of pores defined as a total number of pores occupying the surface area of $1\,\mathrm{cm^2}$ is expressed by

$$n = \frac{10^{14}}{P_h} = \frac{2{\cdot}10^{14}}{\sqrt{3}{\cdot}D_c^2} \tag{24}$$

where P_h is a surface area of a single hexagonal cell (in nm^2) and D_c is given in nm. The substitution of D_c by Eq. (5) leads to the expression as follows:

$$n = \frac{2 \cdot 10^{14}}{\sqrt{3} \cdot \lambda_c^2 \cdot U^2} \cong \frac{18.475 \cdot 10^{12}}{U^2} \tag{25}$$

A different approach to the pore density calculation has been proposed by Palibroda [234,254]:

$$n = 1.6 \cdot 10^{12} exp\left(-\frac{4.764 \cdot U}{U_{max}}\right) \tag{26}$$

where U_{max} has the same meaning as in Eq. (3). For certain anodizing conditions, this critical value of potential (U_{max}) can easily be estimated from Eq. (3), when the pore diameter and anodizing potential are known.

As might be expected from Eqs. (24) and (25), an increasing anodizing potential or interpore distance leads to a decrease in the number of pores formed within the structure [237,238,255]. For anodizing in oxalic acid, increasing the temperature of anodizing decreases the pore density [253]. Pakes *et al.* [201] studied a variation of pore density with anodizing time in disodium tetraborate solution (pH 9.2) at 60 V and 60 °C, and found pore density to decrease slightly with anodizing time at the initial stages of anodizing. This behavior was attributed to the rearrangement of pores, this being a consequence of the transformation of incipient pores into the true pores.

1.2.3
Incorporation of Anions

The incorporation of anions into the structure of anodic oxide layer depends heavily on the film type of the formed oxide. The formation of porous alumina during anodizing leads to a higher anion content in the structure than for barrier-type coatings. It is generally accepted that incorporated electrolyte species are present in the oxide films in a form of acid anion derived from the electrolyte used for anodizing [200]. Published data show an agreement with respect to the content of incorporated acid anions in the bulk of the oxide layer. The typical content of incorporated anions observed for some popular electrolytes are presented in Table 1.6.

Over the past few decades, much research effort has been focused on the determination of profiles of incorporated anions along the width of the oxide layer thickness. A wide variety of techniques has been employed for a depth profiling analysis of the barrier-type oxide layer, including Auger electron spectroscopy (AES) [256], impedance measurements [206], Rutherford backscattering spectroscopy (RBS) [257–259], secondary ion mass spectrometry (SIMS) [260], electron probe microanalysis (EPMA) [261], glow discharge optical emission spectroscopy (GDOES) [201,261–267], and X-ray photoelectron spectroscopy (XPS) [268]. An

Table 1.6 Percentage of incorporated anions in the porous oxide layer [195,200].

Electrolyte	H_2CrO_4	H_3PO_4	$H_2C_2O_4$	H_2SO_4
Anion content (%)	0.1–0.3	6–8	2–3	10–13

excellent review on methods used to study the distribution of incorporated anions in anodic oxide layers was prepared by Despić and Parkhutik [202], in which the kinetics of anion incorporation into the growing alumina films was also discussed.

Schematic profiles of anion concentration in the barrier-type oxide layer are presented in Figure 1.5 for electrolytes frequently used in the formation of highly ordered nanostructures. Sulfate and chromate profiles are drawn on basis of data obtained by the GDOES method [261,262,265,266], whilst the oxalate profile is derived from the AES method [256]. The profile of phosphate anions concentration is a result of analysis of profiles obtained by both methods [256,262,265].

For the steady-state growth of anodic barrier-type film, oxide formation occurs simultaneously at the electrolyte/oxide and oxide/metal interfaces, and is associated with the opposite-direction-migration of Al^{3+} and O^{2-}/OH^- ions. However, a portion of the migrating Al^{3+} ions are ejected directly into solution and do not take a part in formation of the solid oxide film [203,256]. Barrier-type anodic films on aluminum are amorphous, and the transport numbers of Al^{3+} and O^{2-} are 0.44 and 0.56, respectively [256,259,266,267]. Therefore, for film growth at high efficiency, about 40% of the film material is formed at the film surface, and the remainder is formed at the oxide/metal interface. The electrolyte anions are adsorbed at the electrolyte/oxide interface at the pore bases. For steady-state porous film growth, the incorporation of anions into the oxide layer occurs at pores bases as a direct result of the migration of electrolyte species. Electrolyte species can be negatively, positively or not charged, and consequently can either be immobilized on the oxide surface or migrate inwards and outwards at a constant rate, which differs for the various electrolytes. For example, phosphate, sulfate and oxalate anions migrate inwards within the oxide film under the electric field, while chromate anions are characterized by an outward migration [257]. The migration rate of phosphate, oxalate and sulfate anions related to the migration rate of O^{2-}/OH^- ions have been determined
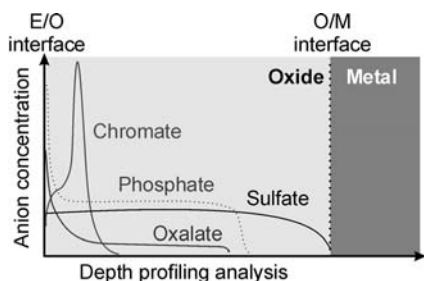

Figure 1.5 A typical depth profile of various anions concentration in the barrier-type oxide film formed by anodization of aluminum.

Table 1.7 Oxide composition and movement of some electrolyte species in the barrier-type amorphous alumina films.

Electrolyte	pH	Anion	Direction of migration	Relative rate of migration	$\frac{N_X}{N_{Al}} \cdot 10^{-2}$	Methods of determination	Reference(s)
0.1 M Na$_2$CrO$_4$	10.0	CrO$_4$$^{2-}$	Out	0.74	0.50 ± 0.01	RBS	[257,269]
0.1 M Na$_2$HPO4	9.4	HPO$_4$$^{2-}$	In	0.50 ± 0.05	3.6 ± 0.3	RBS	[257]
0.1 M (COONH$_4$)$_2$	6.4	COO$^-$	In	0.67	–	AES	[256]
0.1 M Na$_2$SO$_4$	5.8	SO$_4$$^{2-}$	In	0.32 ± 0.07	7.4 ± 0.6	RBS	[257]
1M Na$_2$SO$_4$	–			0.62	–	GDOES	[266]

$\frac{N_X}{N_{Al}}$ is a ratio of the total number of X and Al atoms in the film.

AES: Auger electron spectroscopy; GDOES: glow discharge optical emission spectroscopy; RBS: Rutherford backscattering spectroscopy.

[195,200]. The migration of chromate anions is outward similarly to Al^{3+} ions, and therefore its rate of migration was compared to Al^{3+} ions. The migration rate and composition of film for some anodizing electrolytes used for anodic porous alumina formation are listed in Table 1.7.

The incorporation of boron species was also reported for anodizing conducted under a constant anodizing potential of 60 V in 0.25 M Na$_2$B$_4$O$_7$ solution (pH 9.2) at 60 °C [201]. About 40% of the total anodic oxide layer thickness, when monitored from the top of the film, was found to be associated with incorporated electrolyte species.

There is a significant difference in the porous alumina film growth in comparison to the barrier-type coating formed on aluminum. For porous alumina film growth, film formation occurs only at the oxide/metal interface, and anions migrate into the barrier layer according to the electric field. The electric field at the barrier layer is not uniform due to the semi-spherical shape of the pore base, and is much higher near the pore base close to the electrolyte/oxide interface than at the cell base close to the oxide/metal interface [270]. For this reason, the incorporation of electrolyte anions proceeds more easily. The higher content of incorporated anions in porous alumina layers is also a direct consequence of a long-term exposure of oxide walls for an acid active penetration. The concentration of incorporated SO$_4$$^{2-}$ increases with increasing current density and temperature [271]. Moreover, the incorporation of SO$_4$$^{2-}$ anions along pores, as well as across the barrier layer and pore walls near the pore bases in anodic porous alumina formed in sulfuric acid, was described in detail [272,273]. The parabolic distributions of the incorporated species determined is shown schematically in Figure 1.6.

A significant amount of incorporated anions can be found on the pore bases, such that across the barrier layer a local maximum is reached and a gradual decrease is then observed. The analysis of incorporated anions in the cell walls showed that negligible amounts are observed at cell-wall boundaries, but that the concentration of SO$_4$$^{2-}$ increases steadily, reaches a maximum, and then decreases slightly in a region close to the cell-wall/electrolyte interface. The distribution of anions along the cell wall (along the oxide thickness) is similar to that observed in the barrier layer.
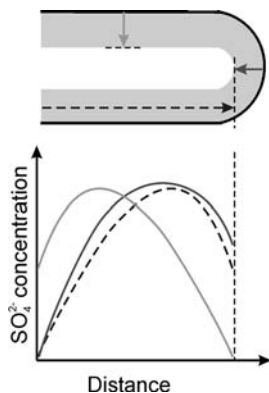
Figure 1.6 Schematic distribution diagram of SO_4^{2-} concentration in the anodic porous alumina formed in sulfuric acid. (After Ref. [272].)

1.2.4
Cell-Wall Structure

The properties of porous alumina films formed by anodizing are related to the electrolyte species incorporated into the oxide walls. For instance, the incorporation of anions modifies space charge accumulation in the porous and barrier-type alumina films [202]. Moreover, the mechanical properties of anodic alumina films, including flexibility, hardness and abrasion resistance, are greatly influenced by the incorporation of anions [200]. The content of incorporated species, and their distribution, depend on the anodizing conditions such as anodizing potential/current density and temperature. Consequently, different wall structures can be expected at different anodizing conditions. The duplex structure of the cell walls (Figure 1.7A) was proposed by Thompson *et al.* [200,274], whereby two different regions – the inner layer containing relatively pure alumina and outer layer with incorporated electrolyte anions – were distinguished. It was reported that the thickness of the inner layer increases in the order:

$$H_2SO_4 < C_2H_2O_4 < H_3PO_4 < H_2CrO_4 \tag{27}$$
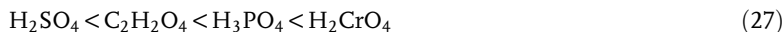
According to Thompson [274], there is a transition from solid to gel-like material in moving across the cell walls towards the pore interior. It was also found that the ratio of the inner to outer layer thickness depends on the electrolyte, and equals 0.05, 0.1 and 0.5 for sulfuric, oxalic and phosphoric acids, respectively [274]. Recently, the triplex structure of the cell walls (Figure 1.7B) was reported for anodized alumina formed by anodization conducted in phosphoric acid [275]. The outer and intermediate layers are contaminated by electrolyte species, mainly anions and protons. The outer layer is rich in anions and protons, whereas the intermediate layer contains mainly anions. The inner layer consists of pure alumina.
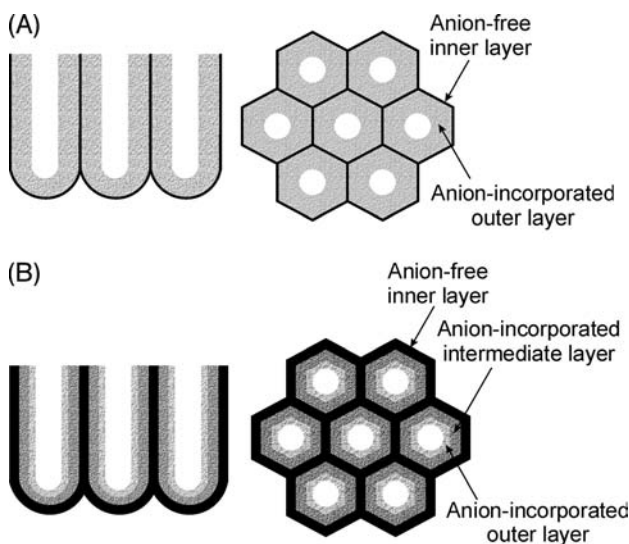
Figure 1.7 Schematic representations of the sectional and plan views of the duplex (A) and triplex (B) structures of porous alumina cell-walls formed in sulfuric and phosphoric acid, respectively. (After Refs. [274,275].)

Although the water content in the porous alumina film can vary between 1 and 15% [200,205], it is generally accepted that the amount of water in porous alumina depends on the anodizing conditions, sample handling, and the measuring technique. The porous oxide films are essentially dry when H_2SO_4 electrolyte is used for their preparation [276]. The porous oxide grown in acidic electrolytes does not contain any bonded water in the film bulk [202], but chemisorption of OH groups and water molecules can occur on the porous oxide layer. The adsorption of water onto the anodic porous alumina formed by anodizing in sulfuric acid was studied by Palibroda and Marginean [277], who found that the amount of adsorbed water on the porous oxide layer was equal to about 100 OH groups per nm^2 and was constant, independent of the sulfuric acid concentration used for anodizing, the temperature of anodizing, and the current density.

The formation of voids in the anodic alumina layer has been reported elsewhere [278–282]. Ono *et al.* [279,280] reported voids on the apexes of aluminum protrusions at the oxide/metal interface in the inner layer of cell walls (see Figure 1.8). These authors suggested that this occurred due to oxygen evolution, to existing tensile stress in the film, or to electrostriction pressure. The size of voids formed in the oxide layer were also found to increase with increasing anodizing potential [279,280]. Moreover, the formed voids could enlarge and merge under electron beam irradiation [281].

A clear and exhaustive explanation of the process of breakdown of anodic passive film and formation of voids was provided by Macdonald [283–285]. The proposed vacancy condensation mechanism of void formation involves a localized
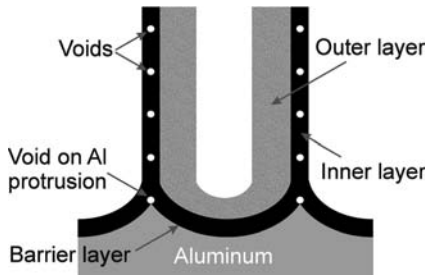
Figure 1.8 Voids in anodic porous alumina film. (After Ref. [285].)

condensation of cation and/or metal vacancies at the oxide/metal interface, and a subsequent detachment of the formed void. A schematic representation of voids formation in the anodic porous alumina is shown in Figure 1.9. When the anodizing process begins, vacancies are produced at the oxide/metal interface as a result of enhanced field-assisted ejection of Al^{3+} directly into the electrolyte. The condensation of vacancies begins at the defected area at the intersection of metal grain boundaries, and a void is formed. The growing void is detached from the apex of
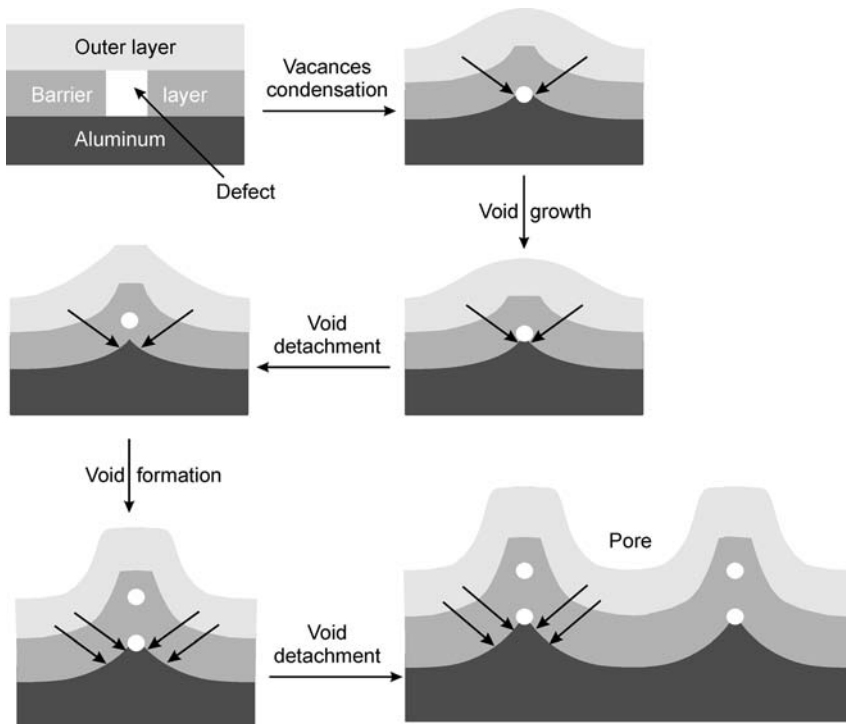

Figure 1.9 Schematic diagrams of the vacancy condensation mechanism for the formation of voids in the porous alumina layer. (After Ref. [285].)

the protrusion when the oxide/metal interface recedes into the aluminum bulk during oxide film formation. After undercutting the void, a new void nucleates on the apex of the protrusion because aluminum becomes rapidly saturated with vacancies. The new void grows, is then detached, and the overall process is repeated.

The vacancy condensation mechanism has been expanded for the description of voids formation in the outer and inner oxide layers [281]. The expanded model was based on the appearance in the oxide/metal interface of a few protrusion apexes after the vacancy detachment instead of that assumed in Macdonald's model.

1.2.5
Crystal Structure of Oxide

Most investigators have agreed that the anodic alumina films formed during anodization are amorphous oxides, or are amorphous with some forms of crystalline γ-Al_2O_3 or γ'-Al_2O_3. The recent observation of anodic films formed, over a wide range of anodizing conditions, does not confirm the presence of crystalline alumina in coatings [200]. The crystallization of γ or γ' alumina can be induced by electron beam irradiation of the sample in the scanning electron microscope [277], with crystallization occurring preferentially in the anion-free inner layer of the cell walls [286–289]. Ono *et al.* [290] found that the crystallization rate of films formed in various anodizing electrolytes decreases with the increasing content of incorporated anions and H_2O/OH^- in the film. The rate of crystallization increases in the following order:

$$H_2SO_4 < C_2H_2O_4 < H_3PO_4 < H_2CrO_4 \tag{28}$$
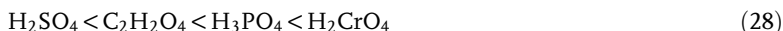
Crystallization in the amorphous alumina can occur during sealing and heating of the film [195,291]. A recent study of porous alumina films formed in phosphoric [275,292], oxalic [293] and sulfuric [291] acids, showed that the originally formed anodic porous alumina films are definitely amorphous. On the other hand, anodizing in chromic acid can result in amorphous alumina with traces of γ-Al_2O_3 [291].

1.2.6
Density and Charge of Oxide Film

The density of anodic alumina films varies significantly with anodizing conditions. For constant current anodizing conducted for 30 min in sulfuric acid, the density of oxide film was found to be $2.78 \, g \, cm^{-3}$ [233]. The notably greater value of $2.90 \, g \, cm^{-3}$ was obtained when the anodizing time was extended to 60 min [233]. Different values of the oxide density were obtained by Ebihara *et al.* [238] for anodization in $2 \, M \, H_2SO_4$. For anodizing potentials from 3 to 14 V and in the range of temperature from 10 to 40 °C, anodic alumina density varied between 3.2 and $3.46 \, g \, cm^{-3}$. It was also found that increasing the anodizing temperature, and increasing the electrolyte concentration as well as increasing the forming potential leads to a slight decrease in oxide density. According to Gabe [294], the density of oxide film formed by anodization in sulfuric acid can vary from 2.4 to $3.2 \, g \, cm^{-3}$. A slight variation in the

density of oxide films with anodizing temperature was found for anodizing in oxalic acid at the constant current density regime [237]. The density of oxide varied between 3.07 and 3.48 g cm^{-3} in the range of temperature from 10 to 40 °C, and increased with decreasing anodizing current density. Recently, the density of amorphous porous alumina was estimated at 3.2 g cm^{-3} [235,242,295]. The density of anodic alumina film formed in dehydrated, high-temperature electrolytes with organic solvents was reported as 2.4 g cm^{-3} [296].

Since anodic porous alumina membranes are often used as templates for nanomaterials fabrication, the charge present on the anodic oxide film is a parameter of major interest. The discussion concerning the space charge in anodic alumina oxide, its distribution and kinetics of space charge accumulation in porous alumina films, has been presented in detail [202]. It is generally accepted that the charge of the oxide film is a result of electrochemical processes occurring during anodization and incorporation of anions into the oxide film. The adsorption of species on anodic alumina membranes and solution–membrane interactions are fundamental factors which determine applications of the membrane for micro- and ultrafiltration, and in this respect especially biotechnological separation aspects are extremely important. The space charge in anodic porous alumina also has a negative influence on the dielectric parameters of oxides, as well as on the long-term drift of oxide properties [202]. A negative space charge in anodic porous alumina was reported [202], while in contrast the positively charged alumina film was discussed in the adsorption of SO_4^{2-} ions occurring during the anodization of aluminum in sulfuric acid [208]. The process of spontaneous adsorption of anions from aqueous solutions was studied for commercially available anodic porous membranes [297]. The maximum number of accessible sites for adsorption was found to be much higher than for neutral polycarbonate or nylon membranes. Moreover, at neutral pH a positive charge of anodic alumina membranes formed by anodization was estimated at 4.2 and 8.5 mC m^{-2} for phosphoric and oxalic acids, respectively. The positive charge in porous alumina attributed to the residual electrolyte in the structure was also reported recently [298]. According to Vrublevsky *et al.* [245], the oxide layer formed in 0.42 M phosphoric acid below 38 V is negatively charged, whilst above 38 V the positive charge of the oxide surface increases with increasing anodizing potential. For anodization conducted in 0.45 M oxalic acid, the anodizing potential at which the surface charge equals zero was estimated at 55 V [247].

1.2.7
Miscellaneous Properties of Anodic Porous Alumina

A growing scientific interest in the fabrication of anodic porous alumina films, and their further application for the synthesis of various nanomaterials, has given rise to many studies of porous alumina self-properties. The thermal characteristics of highly ordered porous alumina structures formed on aluminum have been studied widely [299–306], with thermal analyses being performed in order to collect data on chemical resistance [299,300], structural and optical properties [292,300–303], thermal conductivity and diffusivity along the channel axis [304], self-repair rearrangement of ordered

nanopore arrays induced by long-term heat treatment [305], and mechanical properties [306]. The fracture mechanism, Young's modulus, hardness, fracture toughness [306] and fracture behavior in cylindrical ordered porous alumina [307] were also investigated. The electrical properties of porous alumina films [298,308–311], electron energy-loss, associated with Cherenkov radiation during electron beams traveling parallel to the pores of a porous alumina membrane [312], and surface roughness factors of the film [313], were also studied. Contact angle studies on porous alumina were employed to characterize the liquid/surface interactions at the nanoscale and wetting properties of membranes in contact with different solvents and liquids [314]. It was found that aqueous solutions are not suitable to fill completely the nanopores, and the preferred solvents are dimethyl sulfoxide (DMSO) and N,N'-dimethyl formamide (DMF). Small-angle X-ray scattering (SAXS) techniques were employed for the *in-situ* investigation of filling behavior of porous alumina membranes with a pore diameter of 20 nm in contact with perfluoromethylcyclohexane as solvent [315].

The optical characterization of highly ordered porous materials can provide a variety of information on their nanostructural properties, and especially on pore volume fraction, pore shape, pore diameter, anodic layer thickness and the incorporation of additives occurring during anodizing [316–318]. It is widely recognized that porous alumina exhibits a blue photoluminescence (PL) band [319–326], with the emission bands being attributed to optical transition in the singly ionized oxygen vacancies (F^+ centers) or to electrolyte impurities embedded in the porous alumina membranes. The oxygen vacancies are produced in the alumina matrix as a result of enhanced consumption of OH^- in the electrolyte near the anode occurring during the anodization of aluminum [326]. In contrast, the influence of various additives, such as sulfosalicylic acid, Eu^{3+} and Tb^{3+} ions, on the photoluminescence spectra were investigated [322,327–329]. Weak optical radiation, in the visible range of the spectrum emitted during the anodizing of aluminum in acid electrolytes [known as galvanoluminescence (GL) or electroluminescence] was also studied [330–332]. The concentration of impurities and the pre-treatment of aluminum samples, including degreasing, chemical cleaning and electropolishing, were found strongly to affect GL intensity. Furthermore, the intensity of GL depends on anodizing conditions such as current density, temperature, and electrolyte concentration. It was also suggested that, depending on the nature of the electrolyte – whether organic or inorganic – there are two different mechanisms or two different types of luminescence center responsible for GL.

1.3
Kinetics of Self-Organized Anodic Porous Alumina Formation

1.3.1
Anodizing Regimes and Current/Potential-Time Transient

A hexagonal-shaped oxide cell can easily be formed by anodizing aluminum at a constant current density or constant anodizing potential regime. A typical current
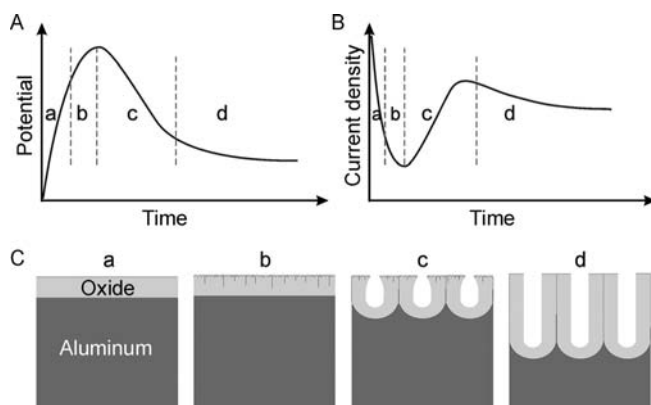
Figure 1.10 Schematic illustration of the kinetics of porous oxide growth in galvanostatic (A) and potentiostatic (B) regimes, together with stages of anodic porous oxide development (C).

density–time and anodizing potential–time transient recorded during the anodization of aluminum in 20% H_2SO_4 at 1 °C are shown in Figure 1.10. When a constant current is applied for porous alumina growth, the potential rises linearly with time until the local maximum is reached, and then decreases gradually to the steady-state-forming potential. During the initial period of anodization (Figure 1.10, stage a), the linear increase in potential is associated with a linear growth of high-resistant oxide film (barrier film) on aluminum. Further anodizing (stage b) results in the propagation of individual paths (pores precursors) through the barrier film. At the maximum of potential (stage c), the breakdown of the tight barrier film occurs and the porous structure begins to be built. Finally, the steady-state growth of porous alumina proceeds (stage d) and a forming potential is almost unchanged. At the start of the process conducted under the constant anodizing potential, current density decreases rapidly with time, and a minimum of current density is quickly achieved. A linear increase then leads to a local maximum. After reaching the maximum, the current density decreases slightly and a steady-state current density of the porous oxide formation is achieved.

The rate of current decrease, the time at which the minimum current is observed, and the steady-state-forming current density depends directly on the anodizing conditions, such as applied anodizing potential, temperature and electrolyte concentration. In general, the minimum of current density decreases with increasing electric field strength, increasing anodizing potential and temperature. The decrease in the minimum value of current is also observed with increasing concentration of acids. The minimum current density occurs earlier, with the higher anodizing potential and lower pH of the electrolyte.

Recently, the constant potential of anodizing instead of constant current regime has been commonly used for the fabrication of closed-packed highly ordered anodic porous alumina films with a desired pore diameter. According to Hoar and Yahalom [333], the relationship between current density and time observed under the
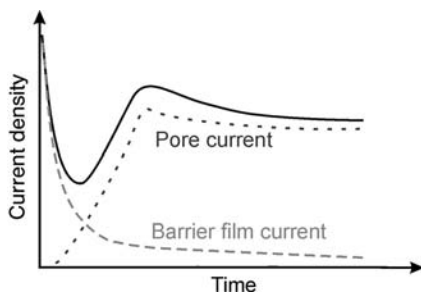
Figure 1.11 Schematic diagram of overlapping processes occurring during the porous oxide growth under constant anodizing potential regime. (After Ref. [333].)

constant anodizing potential is a resultant of two overlapping processes, as shown in Figure 1.11. A first, exponential decrease is connected with the barrier film formation, and the second represents the process of pore formation.

The potential-time transients recorded during anodizing was studied carefully by Kanankala *et al.* [334]. The theoretical model describing the potential–time behavior at the initial stage of anodizing conducted under the constant current regime in 0.21 M H_2SO_4 or 0.3 M $C_2H_2O_4$ was developed. The range of applied current density for anodizing varied between 20 and 50 mA cm^{-2}. The model was based on the rate of oxide formation and rate of oxide dissolution. The predicted potential–time curves fit perfectly with experimentally recorded data. It was also found that the time when the local current maximum appears on the potential–time curve can be estimated as follows:

$$t_{max} = \frac{75}{i} + 1.5 \tag{29}$$

where t_{max} is a time (in s) when the maximum is reached and i is a current density in mA cm^{-2}.

The effect of alloy type on the kinetics of porous oxide growth at constant anodizing potential in sulfuric acid was investigated, and anodizing current density–time transients were studied for various types of aluminum alloys at the anodizing potential of 15 and 18 V [335]. The rearrangement of pores, just before the current density reaches a steady-state value, was found not to occur for some alloys. The rearrangement of pores is usually indicated on the current–time curve (Figure 1.10B) as a local maximum presence at stage c. The lack of pore rearrangement was attributed to an accumulation of the alloying elements (e.g., Cu, Fe and Si) at the oxide/metal interface.

The presence of additives in the anodizing electrolyte can cause a slight modification in the kinetics of the process and the current–time transient. It is widely recognized that, during anodizing, a sulfonated triphenylmethane acid dye ("Light Green") concentrates at the pore base and reacts with released Al^{3+} ions [336,337]. As a result, the movement of Al^{3+} ions into the electrolyte (direct ejection) is strongly

inhibited and the field-assisted dissolution of oxide is significantly reduced. Consequently, a decreasing local current density at the pore base increases a radius of pore base curvature and interpore distance in the presence of an additive. The influence of "Light Green" as an additive on current density–time behavior was studied in detail for the anodizing conducted in sulfuric acid solutions under the constant potential of 15 V [338]. The decrease in current density with increasing concentration of the additive was also observed. It was found also that increasing the concentration of additive also decreases the slope of current density at the pore initiation stage (stage c in Figure 1.10B).

Recently, the mixing of both galvanostatic and potentiostatic regimes has been reported as a new and efficient method for the high-field anodization of aluminum [213,223,251,293,339]. The sample was pre-anodized at a constant current density and, after a certain period of time and after reaching a specified potential, the potentiostatic mode was switched. Depending on the applied initial current density, the duration of the constant current mode varied from a few seconds to 10 min [251]. The method was used successfully for aluminum anodization in sulfuric, oxalic, and phosphoric acids. The requisite anodizing conditions are collected in Table 1.8.

For oxalic acid pre-anodizing, the constant current density should be lower than $10\,mA\,cm^{-2}$ in order to avoid any breakdown of the oxide film and active film dissolution. In the case when pre-anodizing is conducted in phosphoric acid, the initial current density cannot exceed $15\,mA\,cm^{-2}$, and the steady-state current density during anodizing should be kept at about $70\,mA\,cm^{-2}$ to avoid any possible overheating of the sample in a high electric field [213]. It was also found that increasing concentration of Al^{3+} allows higher current densities to be achieved during pre-anodizing, and higher anodizing potentials after switching the mode to potentiostatic. In other words, the fresh electrolyte should be aged by additional electrolysis with the aluminum anode [251]. For this reason the additional pre-electrolysis of electrolyte was employed, with the amount of charge passed through sulfuric acid and other electrolytes (oxalic and phosphoric acids) being 30 and $2\,A \cdot h$, respectively.

Table 1.8 Conditions for the high-field anodizing of aluminum at various electrolytes.

Electrolyte	Concentration (M)	Temperature ($^{\circ}$C)	Current density of preanodizing (mA cm^{-2})	Time of constant current mode (s)	Anodizing potential (V)	Reference
H_2SO_4	1.1 (10%)	0.1	160	—	40	[251]
		0	200	420	70	[213]
$H_2C_2O_4$	0.03 (0.25%)	1	12	60	160	[213]
H_3PO_4	0.1 (1%)	0	16	120	235	[213]
H_3BO_3	0.5 (3%)	RT	1	—	1500	[293]
$(NH_4)_2C_4H_4O_6$	0.17 (3%)	—	1	—	25–100	[223]

RT: room temperature.

A completely novel anodizing technique which employed a pulse sequential voltage with a pulse frequency of 100 Hz was proposed by Inada *et al.* [340]. The technique was used for the strict control of pore diameter in the range of low anodizing potentials (below 3 V) where a linear dependence between pore diameter and forming voltage does not exist. It should be noted that the smallest pores formed by conventional anodizing have a diameter of 7 nm. However, by using the pulse method pores with diameters of 3 and 4 nm can be successfully formed at pulse sequential voltages of 1 and 2 V, respectively.

The anodizing of aluminum resulting in a porous film can be also realized in sulfuric and phosphoric acids under alternating current or potential regimes [341–344]. The observed potential/current–time transients and morphology of films were similar to the conventional anodizing conducted under constant current density or constant potential [343,344]. The percentage of incorporated SO_4^{2-} anions (13%) was the same as found for DC-anodizing [344], but a significant difference was seen to exist between the AC and DC-anodizing. Hydrogen evolution on anodized aluminum occurs during cathodic cycles of AC-anodizing; moreover, for AC-anodizing conducted in sulfuric acid a secondary reaction of SO_4^{2-} reduction proceeds during the cathodic half-cycles, and as a result of this reduction sulfur and/or sulfide is released [341]. In order to reduce the cathodic reduction of sulfate ions, a wide variety of additives (e.g., Fe^{3+}, As^{3+}, Co^{2+}) was studied [341,342]. In contrast, the side cathodic reduction of anions was not observed during AC-anodizing in phosphoric acid [343].

1.3.2
Pores Initiation and Porous Alumina Growth

The phenomena of anodic porous alumina film formation has been studied extensively over several decades, with considerable scientific effort directed towards elucidation of the mechanism of self-organized growth of the porous layer. Thus, several theories have been proposed and developed. Although the anodizing of aluminum was successfully and widely applied for the synthesis of high-ordered nanostructures, it remains unclear as to which physical factors control pore ordering during oxide growth, and especially how the surface features of the aluminum affect the ordering of pores

1.3.2.1 **Historical Theories**
The early theories of porous film growth take into account a passage through the barrier layer nascent oxygen formed from water in pores [345], peptization of aluminum hydroxide gel on aluminum [346], and current action on the barrier layer resulting in pores [347]. Baumman [348,349] proposed the existence of vapor film over the active layer at the bottom of pores where, at a gas/electrolyte interface, oxygen anions are generated. The growth of oxide kernels occurs simultaneously at the base of pores, and the porous structure is a result of oxide dissolution of previously formed breakthroughs (zig-zags).

Keller *et al.* [197] extended this theory and proposed the model in which, at the beginning of the anodizing process, formation of the homogeneous barrier film

occurs and further dissolution of the oxide in the barrier film is followed by the current which repairs the damage to the oxide layer. The passing current increases the local temperature of the electrolyte such that consequently oxide dissolution is enhanced and current breakdowns form pores in the oxide layer. The anodic structure exhibiting the hexagonally arrangement of cells is derived from pores due to the existing tendency of spherical distribution of potential and current about the certain point (pore). It should be noted that a closed-packed hexagonal arrangement of oxide cells is formed as a result of steric factors.

On the other hand, Akahori's hypothesis of porous oxide growth [350] suggested that, after formation of the barrier layer and pores, evaporation of the electrolyte and melting of aluminum occur at the bottom of pores due to the high local temperature. The oxygen ions are then formed at the end of pore in the gaseous electrolyte. Oxygen ions pass the oxide layer at the pore bottom and react with a liquid aluminum base.

A completely different approach to porous oxide growth was proposed by Murphy and Michelson [351]. According to these authors, the outer part of the barrier film formed on aluminum is transformed into hydroxide and hydrate compounds as a result of interaction with water. Simultaneously, the continuous build-up of dense oxide (inner layer) proceeds at the oxide/metal interface. Hydroxide and hydrate compounds have a tendency to bond or to adsorb water and anions from the electrolyte with creation of a gel-like matrix. Submicrocrystallites of aluminum oxide are embedded in this gel. In fact, oxidation takes place at the border between the barrier oxide film (inner layer) and the outer hydrated oxide layer. This model assumed also the transmission of current by Al^{3+} ions, and a responsibility of oxygen ions for the movement of the barrier layer towards the metal base. In this model pores are formed at defect sites where local differences in solubility or electrical breakdown exist.

An interesting view on the initial stages of aluminum oxide formation during anodization and further growth of the oxide layer was presented by Csokan [352]. At the start of the anodizing process, oxygen atoms or electrolyte anions are adsorbed or chemisorbed onto active sites (defects, faults and grain boundaries) on the aluminum surface. The mono or oligomolecular layer of oxide nuclei is then formed. Perpendicular oxide growth is much slower than at the edges of the nucleus, and as a result of this lateral growth the oxide covers the entire aluminum surface. The local differences in chemical solubility of the oxide film and in structural deformations (different state of energy) are directly responsible for the formation of pores. Csokan's theory explains not only the porous anodic alumina structure but also a fibrous structure formed on aluminum by anodizing. The internal stress influence on the oxide structure was also studied by Csokan [352], who found that structural deformations in the oxide films are produced by the isotropic and anisotropic mechanical stresses.

A different interpretation of fibrous anodic alumina structure was given by Ginsberg *et al.* [353–356], according to who the external part of the alumina tube walls is formed from amorphous alumina oxide, while the internal part consists of a gel containing hydroxide and embedded anions. Moreover, the interior of the tube is

filled with the electrolyte and plays an important role in oxygen exchange between electrolyte and metal.

Hoar and Yahalom [333] conducted extensive studies on the pore initiation process during anodizing of aluminum, and suggested that this was a consequence of proton entry into the barrier film when the field strength decreased sufficiently at the certain region. Proton-assisted dissolution of the oxide then occurred.

1.3.2.2 Field-Assisted Mechanism of Porous Film Growth

It is generally accepted that the porous structure of anodic alumina film develops from the barrier-type coating formed on aluminum at the start of anodization. Growth of the barrier film occurs due to the high field ionic conduction and at the constant field strength, defined as a ratio of the potential drop across the barrier film to its thickness [203]. Governed by the constant field strength, the uniform film with a uniform current distribution is developed on the whole surface, as shown in Figure 1.12A.
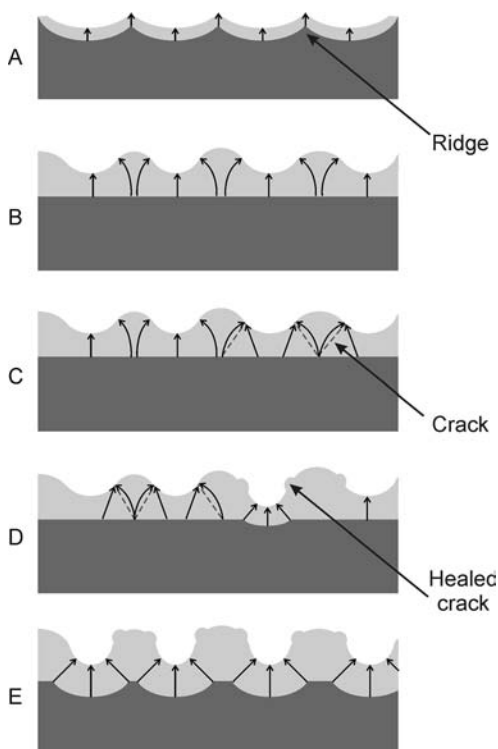

Figure 1.12 Schematic diagram showing current distribution during pore initiation and development of pores on anodized alumina. (After Refs. [200,224].)

The uniform growth results in a smoothing effect on the initial roughness of the aluminum. However, some local variations in field strength can appear on a surface with defects, impurities or preexisting features including subgrain boundaries, ridges and troughs as remains of pre-treatment procedures (e.g., mechanical or electrochemical polishing, etching) [200,208,274]. This non-uniform current distribution leads consequently to the enhanced field-assisted dissolution of oxide and a local thickening of the film (Figure 1.12B). The higher current above metal ridges, accompanied by a local Joule heating, results in the development of a thicker oxide layer [208,255,274]. Simultaneously, the enhanced field-assisted dissolution of oxide tends to flatten the oxide/metal interface. Recently, the effect of local heat transfer on current density was studied for anodizing in sulfuric acid [357]. It was found that increasing the local temperature enhances the local field-assisted oxide dissolution at the pore bases, and consequently increases the local current density. According to Thompson [200,203], the oxide layer grown above the ridges (flaw sites with impurities, scratches) is prone to generate a highly localized stress. Consequently, successive cracking of the film and its rapid healing at the high local current density occur (Figures 1.12C and D). Therefore, with a consumption of aluminum base and enhanced progress in the oxide thickness build-up above the flaw sites, the crack–heal events are more pronounced and the curvature of the film at the oxide/metal interface increases (Figure 1.12E). Shimizu *et al.* [224] suggested that a tensile stress at surface ridges leads to the formation of cracks which can act as conductive pathways for film growth and where rapid healing effect occurs. The preferential growth of oxide above flaw sites, and thickening of the barrier layer, proceed continuously until the moment when the current is concentrated in the thinner film region at the bottom of the future pore (Figure 1.12E). On the other hand, increasing pore curvature (increasing pore diameter) decreases the effective current density across the barrier layer. As a result, the growth of other pores from other incipient pores is initiated in order to maintain a uniform field strength across the barrier layer. When the curvatures of the oxide film at the oxide/metal interface have increased sufficiently and intersection of the scalloped regions has occurred, the steady-state conditions of pore growth are reached. For steady-state porous oxide growth, there is a dynamic equilibrium between oxide growth at the oxide/metal interface and field-assisted oxide dissolution at the electrolyte/oxide interface [208].

The generation of pores was recently studied on aluminum with a tungsten traces layer incorporated into the anodic pre-film formed in phosphoric acid [358]. During the subsequent anodization, the material was found to flow from the region of the barrier layer towards the cell wall regions. This was attributed to the existence of stresses associated with the film growth and field-assisted plasticity of the film material.

When conducted anodization in chromic acid, Thompson [203] suggested that interaction of electrolyte with the barrier film, resulting in the development of penetrating paths is responsible for the local field strength increase just beneath the tip of the penetration path. When the penetrating paths are more advanced, the local field strength increases and further enhanced field-assisted dissolution of paths occurs until an embryo pore at the oxide/metal interface is developed (Figure 1.13).
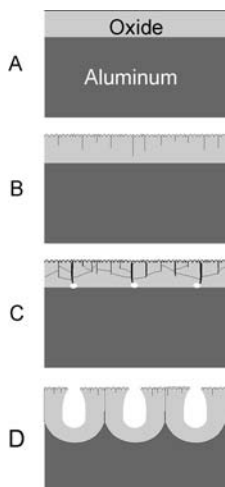
Figure 1.13 Development of penetrating paths and pores during anodizing in chromic acid. (After Ref. [203].)

1.3.2.3 Steady-State Growth of Porous Alumina

Although the anodization of aluminum has been investigated widely, some aspects of the complex process are not yet fully elucidated. It is not clear yet which oxygen-carrying anion species O^{2-} or OH^- ions are involved in the anodic process. The OH^- ions are generated in the anodizing electrolyte from water by simple splitting, or by the cathodic reduction of water and dissolved oxygen through the following reactions:

$$H_2O + 2e^- \rightarrow 2OH^- + H_2 \tag{30}$$

$$O_2 + 2H_2O + 4e^- \rightarrow 4OH^- \tag{31}$$

On the other hand, O^{2-} ions can be formed at the electrolyte/oxide interface from adsorbed OH^- ions by oxygen vacancy annihilation [359], simple splitting of water at the interface, or from water by interaction with adsorbed electrolyte anions in the process shown schematically in Figure 1.14 [208]. In the latter process, OH^- ions may also be produced.

Anodic polarization of aluminum in the acidic electrolyte leads to the amorphous oxide film growth according to the following reactions:

$$2Al^{3+} + 3H_2O \rightarrow Al_2O_3 + 6H^+ + 6e^- \tag{32}$$

and

$$2Al + 6OH^- \rightarrow Al_2O_3 + 3H_2O + 3e^- \tag{33}$$

$$2Al + 3O^{2-} \rightarrow Al_2O_3 + 6e^- \tag{34}$$
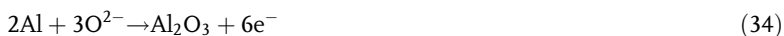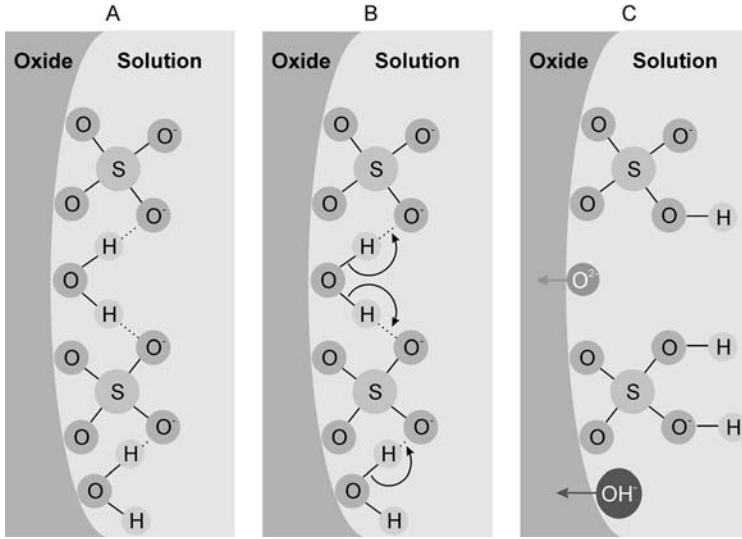
Figure 1.14 Schematic representation of O^{2-} and OH^- ions formation at the oxide/electrolyte interface from water interacting with adsorbed SO_4^{2-} anions. (After Ref. [208].)

The main contribution to the anodic current is made by the given reaction:

$$Al \rightarrow Al^{3+} + 3e^- \tag{35}$$
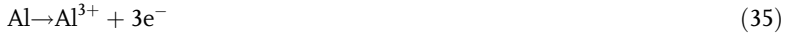
The evolution of oxygen near the metal/oxide interface was reported for anodizing of aluminum in various electrolytes [204,360–362]. This side reaction can be represented as follows:

$$2H_2O \rightarrow O_2 + 4H^+ + 4e^- \tag{36}$$

$$4OH^- \rightarrow 2H_2O + O_2 + 4e^- \tag{37}$$

or alternatively,

$$2O^{2-} \rightarrow O_2 + 4e^- \tag{38}$$

According to Chu *et al.* [363], during aluminum anodizing at high anodizing potentials the generation of oxygen is also possible through the following reaction:

$$H_2O_2 \rightarrow O_2 + 2H^+ + 2e^- \tag{39}$$

The formation of oxygen bubbles within anodic alumina, according to Eq. (38) in the vicinity of the metal/film interface, can proceed due to the presence and compositions of impurities or second-phase particles [360,361]. It was also suggested

that oxygen evolution is directly connected with growth of the porous alumina film, and the process can be used for testing transition from barrier-type to porous-type coatings [204]. The anodic process is further complicated in the presence of electrolyte anions susceptible to oxidation [342]:

$$2SO_4^{2-} \rightarrow S_2O_8^{2-} + 2e^- \qquad (40)$$

It widely recognized that pore formation is attributed to the thermally assisted, field-accelerated dissolution of oxide at the base of pores. On the other hand, the growth of oxide occurs mainly at the oxide/metal interface for typical acidic electrolytes including sulfuric, phosphoric, and oxalic acids. The growth of porous alumina involves the inward migration of oxygen-containing ions (O^{2-} or OH^-) from the electrolyte through the barrier layer, and the simultaneous outward drift of Al^{3+} ions across the oxide layer. It was found that only a part of the Al^{3+} ion flux takes part in the oxide formation at the metal/oxide and oxide/electrolyte interfaces. Depending on the anodizing conditions – and especially on the current efficiency of the oxide growth – oxide formation can also proceed at the oxide/electrolyte interface. For a current efficiency close to 100%, and for phosphates and chromate electrolytes, the majority of Al^{3+} ions reaching the oxide/electrolyte interface are involved in the formation of oxide at the oxide/electrolyte interface [256]. This means that for high-efficiency oxide growth, about 40% of the film material is formed at the oxide/electrolyte interface. This behavior is consistent with the relative transport numbers of Al^{3+} and O^{2-}/OH^- ions observed for various anodizing electrolytes and anodizing conditions. These relative transport numbers for cations and anions are about 0.4 and 0.6, respectively. In contrast, for anodizing in oxalate electrolytes and for processes occurring with a low current efficiency, there is no evidence of any oxide formation at the oxide/electrolyte interface [256]; rather, a direct ejection of Al^{3+} ions to the electrolyte was observed [256]. The remainder of the Al^{3+} ions flux reaching the oxide/electrolyte interface is lost into the electrolyte by field-assisted dissolution [208,274] or by a mechanism involving direct Al^{3+} ion ejection to the solution [359]. A schematic representation of elementary processes involved in porous alumina growth is shown in Figure 1.15.

Additionally, the electrolyte anions migrate inwards to the barrier layer and can be incorporated into the oxide material. The chemical dissolution of oxide in acidic electrolyte results in a thinning of the oxide layer.

For steady-state porous oxide growth, the locally increased field at the electrolyte/oxide interface affects the dissolution of oxide in the pore bases [203]. Increasing field-assisted dissolution of oxide increases the oxide growth rate at the metal/oxide interface due to a dynamic equilibrium between the rate of field-assisted dissolution of oxide and the rate of oxide formation. The field-assisted dissolution of oxide starts from the polarization of Al—O bonds, followed by the removal of Al^{3+} ions from the oxide structure [208]. The removal of Al^{3+} ions occurs more easily in the presence of the field.

The field-assisted oxide dissolution is most likely thermally enhanced through Joule heating effects [208]. According to Li *et al.* [236], a rise in the temperature of the aluminum anode, calculated for a first 12 s of anodizing, is about 25 °C.
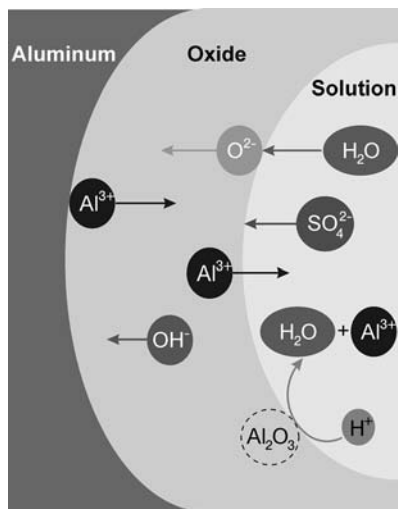
Figure 1.15 Schematic illustration of ions movement and dissolution of oxide in sulfuric acid solution.

1.3.2.4 Growth Models Proposed by Patermarakis and Colleagues

Patermarakis *et al.* [271–273,364–378] described, in several publications, a compact theoretical model of porous alumina growth in various electrolytes. Different approaches have been employed to obtain information about the kinetics and mechanism of the oxide growth mainly in sulfate solutions. The main conclusions derived from these models are outlined in the following sections.

A strict kinetic model of anodic porous alumina growth based on the field-assisted dissolution of oxide was presented by Patermarakis *et al.* [364–368]. The elongated columnar pore with increasing diameter in the direction from the pore bottom to the film's surface was assumed in the model. It was found that, for anodizing conducted in 1.53 M H_2SO_4 under the constant current density regime, oxide dissolution at pores is essentially a field-assisted process, while dissolution of cell walls is governed by first-order kinetics and is thermally activated [364]. The main structural futures of the porous oxide film formed in the unstirred [364,365] and stirred [366] sulfuric acid bath were evaluated. The density of the compact cell walls estimated from the model was about 3.42 g cm^{-3} [364]. For the stirred electrolyte, the concentration of electrolyte in the pores increases linearly on moving from the film's surface to the pore bottoms [366]. The influence of sulfuric acid concentration on applicability of the model in the range between 0.20 and 10.71 M was studied [367]. It was found that the derived kinetic model of porous alumina growth is not valid for the critical concentration of sulfuric existing between 0.51 and 1.53 M [367]. For low acid concentrations, an abnormal oxide growth (pitting and burning behaviors) is suggested. A general formulation of the kinetic model applicable to other galvanostatic anodizations was also proposed [368].

The theoretical model considering mass and charge transport inside pores during the self-organized growth of porous alumina in sulfuric acid was also described

[369]. The proposed model employed both kinetics and transport phenomena equations, and showed that the concentration of $Al_2(SO_4)_3$ at the pore bases is maximal in comparison to other parts of the pore depth; moreover, it increases monotonically with increasing oxide thickness, current density or decreasing temperature [369]. The electrolyte concentration at the pore bases depends on the current density, and various phenomena were observed. The model showed that the sulfuric acid concentration can increase, decrease or reach a local minimum when the analysis of concentration is performed along the pore depth in the direction from the top of the film to the pore bottoms [369]. The transport analysis criterion, which allows prediction of the conditions of regular and abnormal oxide growth, was also performed [370,371]. The most important parameter influencing abnormal oxide growth is electrolyte concentration at the pore base in relation to the current density [370]. The promotion of pitting occurs at low temperature and sulfuric acid concentration or high current density and sulfate additives including $Al_2(SO_4)_3$ [371,372]. For the saturated $Al_2(SO_4)_3$ solution in H_2SO_4, the incorporation of colloidal micelles of aluminum sulfate was observed in the cell walls [373,374]. The kinetics and mechanism of anodizing were also found to be strongly influenced by colloidal micelles. Recently, a comparative study was performed in order to establish the kinetics and mechanism of anodizing in oxalic acid [375]. The mechanism of porous oxide growth in oxalic acid was the same as observed for sulfuric acid, but with an easier and stronger growth of colloidal micelles being reported.

A model for charge transport across the barrier layer was also proposed by Patermarakis *et al.* [376–378]. The prolonged anodization proved that the rate-controlling step of the steady-state growth of porous alumina is charge transport across the barrier layer, with the native oxide being produced mainly in the region adjacent
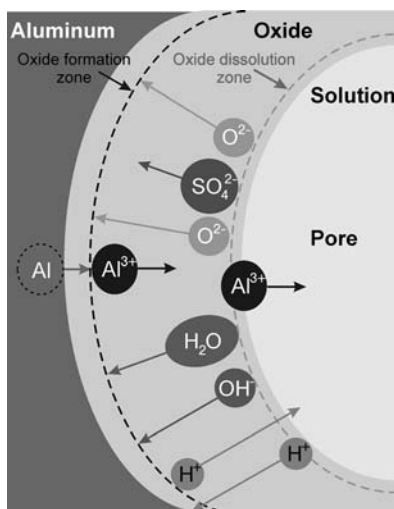

Figure 1.16 Schematic representation of the cross-sectional view of the barrier layer in anodic porous alumina. (After Ref. [376].)

to the metal/oxide interface (Figure 1.16). The zone where field-assisted dissolution of oxide occurs is located inside the oxide film, near the oxide/electrolyte interface.

According to the derived model, the ionization of aluminum as shown in Eq. (35) proceeds through successive one-electron-transfer elementary steps. Charge transport across the barrier layer is realized by the migration of O^{2-}, OH^- and SO_4^{2-} ions. The model conclusions predicted that the O^{2-} ions necessary for aluminum oxidation are derived from the oxide lattice and from OH^- ions adsorbed on the oxide surface. Al^{3+} ions are rather immobilized inside the oxide film, especially at a lower field strength. In the dissolution zone, the Al^{3+} ions are solvated and then move towards the bulk of electrolyte. In the oxide film, SO_4^{2-} ions migrate along a boundary surface of microcrystallites through the successive vacancies. Sulfate anions are much larger than O^{2-} ions, and their movement towards the metal/oxide interface is gradually blocked by greater-sized microcrystallites. The electrolyte anions are unable to reach the oxide formation zone and finally become embedded on microcrystallites in the bulk of the oxide. The model calculation is consistent with experimental data, and proved that there is no significant difference in the incorporation of various type of anion derived from the same electrolyte, such as SO_4^{2-} or HSO_4^-. Other anions, including OH^- and O^{2-}, migrate at similar rates due to the comparable ratio of ion charge to the radius. The migration process is probably realized through vacancies inside crystallites. The OH^- ions can be incorporated on/in crystallites in the oxide bulk, or they can decompose inside the oxide to O^{2-} and H^+. It is most likely that the OH^- ions reach the oxide formation zone and form the oxide film according to Eq. (33). In accordance with the model assumptions [377,378], the process of field-assisted dissolution of oxide and OH^- ions migration in the oxide lattice can be represented as shown in Figure 1.17.

Due to the positive surface charge of oxide in acidic electrolytes, decomposition of water occurs in the double layer. Consequently, the OH^- ion is adsorbed at the oxide/electrolyte interface on the Al^{3+} ion derived from the oxide lattice (Figure 1.17A). Under the high field strength, the H^+ ion is rapidly removed from the double layer to the bulk of solution. The adsorption of OH^- ion onto Al^{3+} weakens the bonds between Al^{3+} and O^{2-} ions in the oxide lattice (Figure 1.17B). The O^{2-} ion can then leave its position in the lattice and migrate further towards the metal/oxide interface. This results in anion void formation in the lattice and further possible occupation of the void by the previously adsorbed OH^- ion (Figure 1.17C and D). Simultaneously, the Al^{3+} ion can move slowly towards the bulk of electrolyte. The process of adsorption and further migration of other OH^- ions is faster than the Al^{3+} ejection to the solution, and can easily be repeated several-fold by the time the Al^{3+} ion leaves its position [377].

1.3.2.5 Other Phenomenological Models of Porous Alumina Growth

Although the field-assisted mechanism of oxide growth is commonly used to describe the self-organized growth of anodic porous alumina, some other models have been developed. The formation of colloidal layer at the electrolyte/metal interface was assumed by Heber [379,380] in his model of pore development and film growth. A chemical interaction between hydroxide, electrolyte and adsorbed water molecules
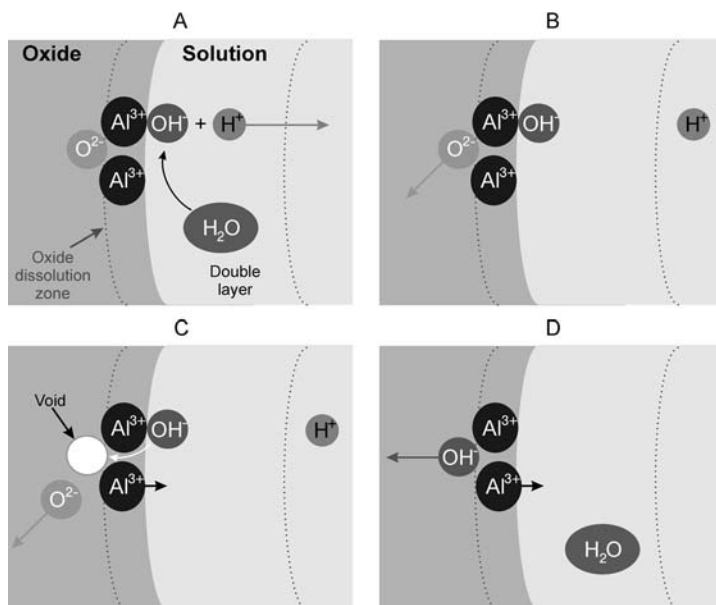
Figure 1.17 The process of field-assisted dissolution of oxide and OH⁻ ions movement in the oxide lattice according to the Patermarakis' model.

within the colloidal layer leads to the formation of droplets and pockets. Pressure inside the pocket is responsible for the pore development and further growth. On the other hand, the formation of a gel-like nascent oxide was assumed in various other studies [227,274,351,381,382]. The gel layers promote the formation of anodic alumina in antimonate, molybdate, silicate and tungstate electrolytes [382]. The gel layer, which is formed above the growing oxide film, eliminates the field-assisted ejection of Al^{3+} ions to the electrolyte. Moreover, it was found that the gel layer could shrink and easily crack on drying.

Stress generation during anodic oxidation of aluminum was studied by Nelson and Oriani [383]. Tensile stress was found to develop rapidly at the metal/oxide interface due to differences in the volume between the metal ions and the oxide. The compressive stress remains constant during the whole process of anodizing. Various possible reactions of aluminum oxidation occurring at the metal/oxide and oxide/electrolyte interfaces were suggested. One proposed model assumed that ions move only through the vacancy exchange mechanism, and that the concentration of vacancies does not change within the oxide film, except at the metal/oxide interface. Compressive stress at the oxide/metal interface, associated with volume expansion during oxide formation, was indicated by Jassensky *et al.* [384] as a main force responsible for the cellular growth of porous alumina. The generated compressive stress creates repulsive forces between neighboring pores and, as a consequence, induces a close-packed hexagonal arrangement of oxide cells. Since the oxide film formation involves oxidation occurring at the oxide/metal interface, the only

direction in which material can expand is by a vertical upwards growth of the cell walls. For the steady-state growth of porous alumina resulting in a high-order of nanopores, a uniform local compressive stress was postulated [385]. The suitable compressive stress provides the correct conditions for steady-state oxide growth, whilst a higher stress might break the oxide walls. A lower compressive stress alters the penetration direction of pores and modifies their growth. An external tensile stress which influences the ordering of pores in self-organized anodization was also studied [231]. Well-ordered structures on anodized aluminum were obtained even on the stressed surface, but a relatively high tensile stress was seen to destroy the arrangement of the pores and, instead of nanopores, huge holes and pits are formed on the highly stressed surface.

The Macdonald's point defect model [283–285] assumed that during film growth, cation vacancies are produced at the oxide/electrolyte interface and are consumed at the metal/oxide interface. In contrast, anion vacancies are formed at the metal/oxide interface but are consumed at the oxide/electrolyte interface. The film formed above metal ridges may contain a high concentration of vacancies (vacancies condensation). According to the model, vacancies at the metal/oxide interface are responsible for the breakdown of the anodic passive film and for large local cation flux through the film. This model predicts that the steady-state thickness of the barrier layer and the logarithm of the steady-state current density should vary linearly with applied anodizing potential.

According to Palibroda *et al.* [227,234,254,386,387], the steady-state growth of the porous oxide layer is a consequence of the electrical breakdown of the barrier layer by a series of non-destructive avalanches that provide easy pathways for the oxidation of aluminum. The model of oxide growth consists of three steps, the first step being rate-determining in nature [254]. The first step consists of transformation of the existing barrier layer from a compact to porous oxide film. In the second step, aluminum is ionized according to Eq. (35), followed by the reaction of new barrier layer formation [Eq. (32)] in the third step. The proposed model assumed that the barrier layer behaves as a semiconductor, and electrical breakdown of the barrier layer proceeds through non-destructive avalanches [386] which have been previously proposed to explain the electroluminiscence phenomenon of anodic alumina oxide [388]. In contrast, Shimizu *et al.* [389] found that even a few Angstroms difference in barrier layer thickness caused a remarkable variation in local electron tunneling probability. In summary, it can be stated that local differences in oxide thickness promote the electrical breakdown of the barrier layer. The Hoar–Yaholm mechanism of barrier layer protonation [333] and possible proton conductivity in the barrier layer was studied by Palibroda *et al.* [254,386,387], but no evidence was observed that this mechanism might contribute to the rate-determining step.

Li *et al.* [236] considered the model of porous alumina growth in which ionization of aluminum according to Eq. (35) proceeds at the metal/oxide interface. The formation of O^{2-} anions occurring by a water-splitting reaction at the oxide/electrolyte interface is a rate-determining step. The increasing electric field at the pore bottom increases local acid-catalyzed corrosion of oxide, and reduces the barrier layer thickness. As a result, the pores are initiated and their further growth proceeds through the

self-catalyzed oxide dissolution. An increase in local temperature at the pore bottom (ca. 21 °C), due to Joule heating and acid-catalyzed dissolution of oxide, may lead to a local dehydration of the hydroxide. Consequently, the development of voids and a lateral non-uniform compulsive stress within the middle shell of the cell is observed.

A cellular growth mechanism of self-organized anodic porous alumina was proposed by Zhang *et al.* [390]. The oxide film propagation and growth takes place at a curved metal/oxide interface, which can be counted as an unstable planar front. The dissolution of aluminum and growth of the oxide are controlled by the distribution of the electrical field (instability), which results in a re-stabilized curved metal/oxide interface. Under steady-state conditions, the curved interface then propagates.

1.3.2.6 Other Theoretical Models of Porous Alumina Growth

The model of electronic conduction of anodic oxide based on the hopping conductivity of real amorphous dielectrics of limited thickness, with or without incorporated ions, was presented by Parkhutik and Shershulsky [239]. The hopping transport was modeled as a quasi-Marcovian process. The current density–voltage relationships recorded during aluminum anodizing were fully consistent with model predictions for a dielectric with negative space charge. The slope of the current–voltage relationship was found to be related directly to the transition from the bulk-limiting hopping conduction to surface-limited conduction. Another theoretical model based on electrical field distribution was proposed by Parkhutik *et al.* [202,391]. Basic conclusions derived from the field-assisted model of oxide growth were assumed. The model also considered oxide dissolution by the electrochemical or electric field-enhanced mechanism and 3D electric field distribution in the scalloped barrier layer at pore bottoms. According to this model, the film geometry largely influences the local conduction rate, and is therefore a main parameter responsible for the formation of a porous oxide. The model predicted that steady-state porous oxide growth is a time-independent phenomenon, and that pore formation occurs in a self-consistent manner. The relationship between pore geometry and some anodizing conditions, including anodizing potential, temperature and pH, were successfully established using this model, and the theoretical predictions obtained were consistent with experimental data [239]. Parkhutik *et al.* [392] also studied the effect of combined barrier and porous oxide growth in the mixture of chromic acid with sulfuric acid. The results were attributed to an enhanced formation of insoluble aluminum chromates at high electric field. The effect of extreme dependence of pore growth rate on the electric field was suggested as a feasible explanation for this situation.

A mathematical model of oxide morphology evolution during anodizing was presented by Wu *et al.* [393]. The main assumption of this model was based on the established conduction behavior of anodic alumina oxide and interfacial reactions. Additionally, the effect of current distribution on the near-concentric hemispherical contour between existing surface ridges was taken into account. The enhanced film growth above metal ridges due to a lower local resistance to the metal/oxide interface results in a 2D potential distribution in the oxide film. Although the process of porous oxide formation was described satisfactorily, a lack of explanation for porous oxide growth in a narrow window of experimental

conditions was evident. The same modeling school also presented a simulation of the breakdown mechanism of passive oxide films and the growth of pits leading to tunnel formation in anodized alumina during the anodic etching in solutions containing chloride ions [394,395].

In addition to these previously mentioned models, many different approaches to the anodic porous alumina growth have been described in the literature. The morphology of anodic porous alumina membranes was simulated using a radial function of distribution of cells in the triangular network [396], rate equations for competitive processes of alumina formation and etching [334,397], or linear stability analysis showing instability of oxide layer with respect to perturbations with a well-defined wavelength [398]. An electrical bridge model based on the analysis of ion transport in the oxide film and electrical field distribution was also proposed in an attempt to elucidate the self-organized growth of anodic porous alumina [399].

One very promising approach to the anodic porous alumina description seems to be a fractal model of the porous layer formation [400], and the appearance of hexagonally ordered patterns as a result of Turing systems modeling [401,402].

1.3.3
Volume Expansion: The Pilling–Bedworth Ratio (PBR)

The volume expansion of an anodic porous alumina, R, known also as the Pilling–Bedworth ratio (PBR), is defined as the ratio of the volume of aluminum oxide, which is produced by anodizing process, to the consumed aluminum volume:

$$R = \frac{V_{Al_2O_3}}{V_{Al}} = \frac{M_{Al_2O_3} \cdot d_{Al}}{2 \cdot M_{Al} \cdot d_{Al_2O_3}} \tag{41}$$

where: $M_{Al_2O_3}$ is the molecular weight of aluminum oxide, M_{Al} the atomic weight of aluminum, d_{Al} and $d_{Al_2O_3}$ are densities of aluminum ($2.7\,\mathrm{g\,cm^{-3}}$) and porous alumina ($3.2\,\mathrm{g\,cm^{-3}}$), respectively. The theoretical value of the PBR for porous alumina formation with a 100% current efficiency is 1.6. Therefore, the aluminum specimen volume increases significantly during anodizing (see Figure 1.18).

Experimental values of the volume expansion differ slightly from the theoretical predictions due to the lower current efficiency of anodizing, and usually vary between 0.9 and 1.6 [224,384]. Jassensky *et al.* [384] found that increasing the anodizing potential increases the PBR for anodization conducted in sulfuric acid and the optimal conditions of anodizing; this results in the formation of high-ordered anodic porous alumina corresponding to a moderate expansion of aluminum ($R = 1.22$).
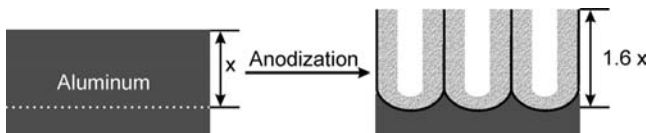

Figure 1.18 Volume expansion observed during anodization of aluminum.

Table 1.9 Anodizing potential influence on the Pilling–Bedworth ratio at 20 °C and galvanostatic regime of anodizing.

Electrolyte	Anodizing potential (V)	$R = f(U)$	Reference(s)
0.45 M $H_2C_2O_4$	$22 < U < 45$	$1.092 + 0.007 \cdot U$	[405]
	$U \leq 55$	$1.144 + 0.0057 \cdot U$	[247,404]
	$U > 55$	$1.308 + 0.003 \cdot U$	
1.1 M H_2SO_4	$13 < U < 24$	$1.1 + 0.0217 \cdot U$	[404]

According to Li *et al.* [403], the volume expansion factor for optimal anodizing conditions leading to the hexagonally arranged nanopores should be close to 1.4, independent of the electrolyte. For anodizing conducted in 0.34 M oxalic acid at 40 V, the volume expansion factor was found to be about 1.18 [236]. An anodic alumina porosity of 10% guarantees the best ordering of nanopores and volume expansion of about 1.23 [235]. By increasing the PBR above 1.3, a decrease in the size of the ordered domains was observed. The volume expansion factor for the anodization of aluminum in a 0.15 M citric acid solution at 6 and 10 mA cm^{-2} was found to be 1.4 and 1.5, respectively [217].

The influence of anodizing potential on the volume expansion factor was studied by Vrublevsky *et al.* [247,404,405], for the anodization of aluminum conducted under a constant current density. Measurements were performed using a mechanical profiler with a computer signal processing for oxalic and sulfuric acids, whereupon the PBR was found to be linearly dependent on the anodizing potential (Table 1.9).

In contrast, the concentration of oxalic acid in the range between 0.22 and 0.92 M (2% and 8%) did not affect the volume expansion factor [405]. For anodizing under constant current density, increasing the temperature causes a decrease in anodizing potential and volume expansion factor. Yet, increasing the current density increases the volume expansion factor. This effect can be attributed to the fact that the PBR depends on the electric field strength in the barrier layer. The dependence of the current density logarithm on the inverse volume expansion factor of anodic porous alumina is linear [247,404,405].

1.3.4
Rates of Oxide Formation and Oxide Dissolution

A wide variety of methods were employed to measure the thickness of the oxide layer formed by anodization of aluminum [205]. Recently, optical and microscopic techniques including TEM or SEM have mainly been used to evaluate anodic oxide layer thickness.

For the constant current density anodization, the total thickness of the oxide layer can be calculated from the pore-filling method, using the formula produced by Takashi and Nagayama [406]:

$$h = 10^{-7} \cdot B_U \cdot V_p - \frac{i \cdot t_p \cdot M_{Al}}{n \cdot F \cdot k \cdot d_{Al_2O_3}} (1 - T_{Al^{3+}}) \tag{42}$$

where, B_U is the barrier layer thickness per volt (nm V^{-1}), i is the current density (mA cm^{-2}), M_{Al} is the atomic weight of aluminum, n is the number of electrons associated with oxidation of aluminum, F is Faraday's constant, k is the weight fraction of aluminum in alumina (0.529), $d_{Al_2O_3}$ is the density of porous alumina (3.2 g cm^{-3}), $T_{Al^{3+}}$ is the transport number of Al^{3+} ions (about 0.4), and V_p and t_p are the voltage and time, respectively measured at the point where two straight parts of the voltage–time transient meet.

On the other hand, the thickness of the oxide layer can be calculated from Faraday's law. As the efficiency of anodizing is not usually 100%, the recorded current density cannot be used simply for theoretical estimation of the grown oxide layer, and the current efficiency should be considered as follows:

$$m_{Al_2O_3} = k_{Al_2O_3} \cdot j \cdot t \cdot \eta = \frac{M_{Al_2O_3}}{z \cdot F} \cdot j \cdot t \cdot \eta \tag{43}$$

where, $m_{Al_2O_3}$ is a mass of formed oxide, $k_{Al_2O_3}$ is the electrochemical equivalent for aluminum oxide, j is the passing current (A), t is the time (s), η is the current efficiency, $M_{Al_2O_3}$ is the molecular weight of aluminum oxide (g mol^{-1}), z is the number of electrons associated with oxide formation, and F is Faraday's constant (C mol^{-1}). Taking into account that the oxide mass can be expressed as the product of oxide density ($d_{Al_2O_3}$) and oxide volume ($V_{Al_2O_3}$) or as the product of density, the surface area (S) and oxide height (h):

$$m_{Al_2O_3} = d_{Al_2O_3} \cdot V_{Al_2O_3} = d_{Al_2O_3} \cdot S \cdot h \tag{44}$$

the oxide layer thickness formed at constant current anodizing is:

$$h = \frac{M_{Al_2O_3}}{z \cdot F \cdot d_{Al_2O_3}} \cdot \frac{j}{S} \cdot t \cdot \eta = \frac{M_{Al_2O_3}}{z \cdot F \cdot d_{Al_2O_3}} \cdot i \cdot t \cdot \eta \tag{45}$$

where i is the current density. Consequently, for the constant potential anodizing the thickness of the oxide layer can be expressed by:

$$h = \frac{M_{Al_2O_3}}{z \cdot F \cdot d_{Al_2O_3}} \cdot \eta \int_0^t i(t) \, dt \tag{46}$$

It is generally accepted that the constant current anodizing, the oxide thickness increases linearly with increasing current density according to the following relationship:

$$h = k \cdot i \cdot t \tag{47}$$

where k is a constant value independent of current density and temperature [364]. Therefore, the oxide layer thickness formed under constant potential anodizing can

be calculated:

$$h = k \int_0^t i(t) \, dt \tag{48}$$

The value of k was estimated at about $3.09 \times 10^{-6} \, \text{cm}^3 \, (\text{mA} \cdot \text{min})^{-1}$ for the constant current density anodizing carried out in $1.53 \, \text{M} \, H_2SO_4$ [364,367].

The thickness of the oxide layer grown under the constant potential regime in $0.3 \, \text{M}$ oxalic acid can be easily estimated from SEM cross-sectional views and rates of oxide formation (R_h in $\text{nm} \, \text{min}^{-1}$) at various temperatures according to the given equation [241]:

$$(5\,°C) \quad R_h = 392.30 - 26.92\,U + 0.63\,U^2 \tag{49}$$

$$(15\,°C) \quad R_h = 123.43 - 9.19\,U + 0.23\,U^2 \tag{50}$$

$$(30\,°C) \quad R_h = 51.33 - 3.71\,U + 0.095\,U^2 \tag{51}$$

Sulka *et al.* [240,407] determined the experimental rate of oxide formation in $2.4 \, \text{M}$ H_2SO_4 under the constant potential anodizing regime. The growth rate of the oxide layer was calculated for Al samples treated by one-, two-, and three-step anodizing conducted in the overflow cell [407] at $1\,°C$ (Figure 1.19A). No difference was found between the experimental growth rate of oxide layers obtained by the one-, two-, and three-step anodizing procedures. The experimental growth rates of oxide anodized in the simple electrochemical cell with magnetic stirring were also determined for various anodizing temperatures (Figure 1.19B). The effective growth rate of the oxide layer on anodized aluminum increases exponentially with increasing cell potential.

In general, the steady-state growth of anodic alumina is a result of equilibrium between the rate of chemical formation and rate of oxide dissolution. The total amount of dissolved oxide is a sum of electrochemical dissolution (field-assisted process) and chemical etching. Hence, dissolution of the oxide layer should be a function of the hydrogen ion concentration in the anodizing electrolyte, and is especially accelerated by H^+ ion adsorption [199,202,254]. The typical rate of field-assisted dissolution of alumina at room temperature is about $300 \, \text{nm} \, \text{min}^{-1}$, compared to a value of $0.1 \, \text{nm} \, \text{min}^{-1}$ in the absence of the field (chemical dissolution) [203]. For anodizing conducted in $1.5 \, \text{M} \, H_2SO_4$ under $17 \, \text{V}$ ($12.9 \, \text{mA} \, \text{cm}^{-2}$) at $21\,°C$, the rates of field-assisted dissolution and chemical dissolution were calculated to be about 372.5 and $0.084 \, \text{nm} \, \text{min}^{-1}$, respectively [244]. According to Nagayama and Tamura [408], the rate of field-assisted dissolution of oxide is about $1040 \, \text{nm}$ min^{-1} for anodization carried out in $1.1 \, \text{M} \, H_2SO_4$ at $11.9 \, \text{V}$ and $27\,°C$.

A strict control of the anodic nanoporous alumina formation requires the gaining of access to the correct information concerning the rate of chemical dissolution of oxide in the acidic electrolyte. The chemical dissolution of oxide, especially in acidic
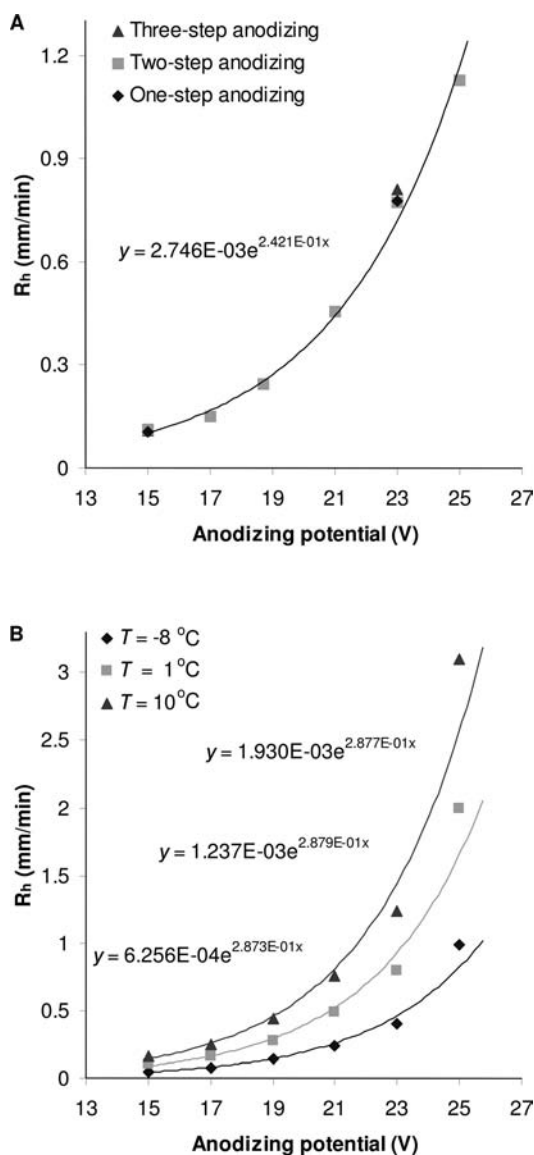
Figure 1.19 Growth rate of the oxide layer (R_h) versus anodizing time. Anodizing was conducted at a constant cell potential in a 2.4 M (20%) sulfuric acid electrolyte in the overflow cell (A) at 1 °C and simple electrochemical cell (B) at various temperatures. (Figure 1.19A reproduced with permission from Ref. [407], © 2002, The Electrochemical Society.)

Table 1.10 The rate of chemical etching of anodic alumina.

Electrolyte	Concentration (M)	Temperature (°C)	Etching rate (nm min^{-1})	Reference
H_2SO_4	1.7 (15%)	20	0.076	[244]
		25	0.114	
		30	0.172	
		50	0.873	
		70	4.434	
	0.1 (1%)	38	0.25	
	0.21 (2%)		0.27	
	1.4–3.1 (12–25%)		0.33	
	7.0 (48%)		0.25	
	15.3 (85%)		0.125	
	2.4 (20%)	20–22	0.05	[252]
	1.53 (13.7%)	20–40	0.052–0.41	[364]
	1.1 (10%)	27	0.074	[364]
	1.1 (10%)	27	0.075	[408]
	2.0 (11.1%)	60	1.6	[206]
$H_2C_2O_4$	0.63	40	0.43	[406]
H_3PO_4	0.45 (4.25%)	20–22	0.02–0.02	[252]

electrolytes, is of major significance for the development of post-treatment procedures that allow the strict control of the pore diameter of nanostructures. Moreover, the rate of chemical etching of oxide in certain media serves as valuable information in the process of selecting optimal anodizing conditions. The chemical dissolution of alumina was normally studied in a sulfuric acid solution due to a strong chemical aggression of the concentrated electrolyte used for anodizing. The concentration of phosphoric or oxalic acid used as an electrolyte for the anodization of aluminum is at least a few-fold lower than the sulfuric acid concentration. Consequently, the expected rate of chemical etching of alumina in phosphoric or oxalic acids solutions is significantly lower. Selected values of the chemical etching rate in various electrolytes are listed in Table 1.10.

The rate of oxide dissolution in 1.53 M oxalic acid is much slower than for the same concentration of sulfuric acid [375]. For example, the rate of chemical etching of oxide at 35 °C in oxalic acid is comparable with the rate of dissolution at 25 °C in sulfuric acid [375]. The incorporated phosphate anions enhanced the chemical dissolution of oxide [268]. Further details on the dissolution rate of the barrier layer are presented in Section 1.4.3.

1.4
Self-Organized and Prepatterned-Guided Growth of Highly Ordered Porous Alumina

The process of alumina template formation by anodization is relatively simple and results in a high density of parallel nanopores. Hence, anodic porous alumina (AAO)

is a key template material for the fabrication of various nanostructured materials. In general, there are two widely used methods of AAO template synthesis: (i) a self-organized, two-step anodization leading to a quasi-monodomain structure; and (ii) a prepatterned-guided anodization resulting in a perfectly ordered pore lattice.

A flow diagram of the self-organized formation of anodic alumina membranes by the anodization of aluminum with a typical two-step anodizing procedure is presented in Figure 1.20.

The formation of nanopores by self-organized anodizing of aluminum is a multistage process consisting of a pre-treatment, anodizing, and post-treatment steps. The pre-treatment procedure includes annealing of aluminum foil in a non-oxidizing atmosphere, degreasing of samples, and electropolishing. The two-step anodizing procedure is usually based on the initial anodizing at the pre-selected cell potential and subsequent chemical etching of the grown aluminum oxide layer. Following the chemical removal of oxide, a periodic concave triangular pattern formed on the aluminum surface acts as self-assembled masks for the second anodizing. The second anodization is conducted at the same cell potential as used during the first anodizing step. Finally, the synthesized hexagonally arranged nanopore structure can be removed from the base aluminum, and the pores may be opened and widened.
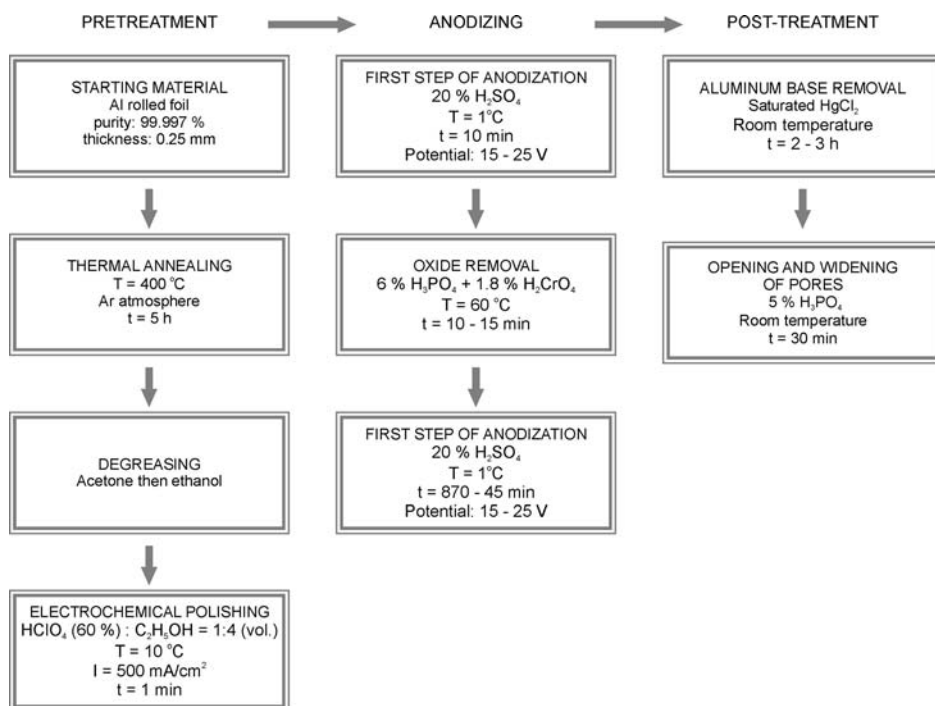

Figure 1.20 Flow diagram of AAO templates formation by two-step anodizing in sulfuric acid.

In contrast, prepatterned-guided anodizations based on the pre-texturing of electropolished aluminum prior to anodizing are used for the synthesis of ideally ordered nanopores. Among these methods, a direct indentation of the aluminum surface with a tip of the scanning probe microscope [410,411], focused-ion beam lithography [412–415], holographic lithography [416] and resist-assisted focused-ion beam lithography [417–419] were used successfully to form the pattern on the aluminum surface. In the direct patterning of aluminum, each sample can be indented individually, although this makes the techniques time-consuming and also limits their applications to the laboratory scale. Therefore, the imprinting lithography with a master stamp (mold) is the most widespread method used for prepatterning of aluminum [420–436]. Stamps with an arranged array of convexes are usually prepared lithographically, and can be used several times for the pre-texturing of aluminum. The mold used for nanoindentation of aluminum can be made from SiC [420–429], Si_3N_4 [430–432], Ni [433–435] and poly(dimethylsiloxane) (PDMS) [436]. The imprinting of aluminum using a master stamp and fabrication of anodic porous alumina from prepatterned aluminum is illustrated in Figure 1.21.

The imprinting of aluminum with a master stamp is usually carried out using an oil press. After imprinting, the generated array of concaves on the aluminum surface is a negative replication of convexes of the master stamp. The typical depth of the concave formed by the molding process is about 20 nm [420]. The different shape and arrangement of convexes in the master mold leads to various nanopore arrays in anodic porous alumina. The indentation of triangular, square, and graphite structure lattices results in hexagonal, square, and triangular cells, respectively (Figure 1.22) [424–427,430,432,434,436]. The porous alumina array with a Moiré pattern was also fabricated using indentation with the mold [431].
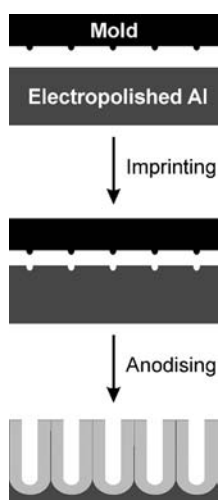
Figure 1.21 Schematic diagram of fabrication of ideally ordered porous alumina using an imprint stamp.
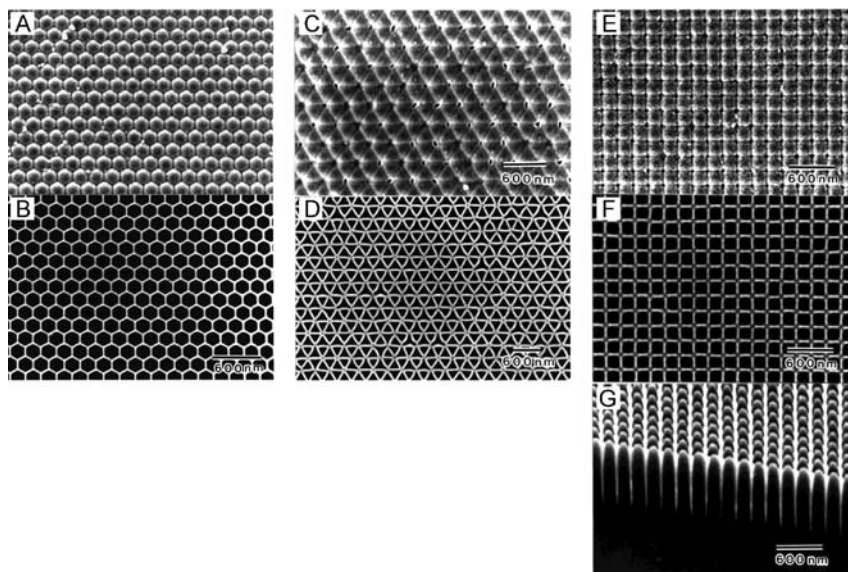
Figure 1.22 SEM images of cells (A, C, E), openings (B, D, F) at the bottom side of anodic alumina and cross-section (G) of anodic alumina formed by indentation of triangular, graphite structure and square lattices. (Reprinted with permission from Ref. [427], © 2001, Wiley-VCH Verlag GmbH.)

Recently, the prepatterned aluminum surface has been obtained using nanosphere lithography (NSL) employing a 2D hexagonal close-packed array of polystyrene [433,437] and Fe_2O_3 spheres [438] formed on the Si or glass supporting substrate. The aluminum layer was sputtered over the self-organized array of spherical monodisperse nanoparticles. After the removal of particles, shallow concaves formed on the Al surface serve as initiation points for pore formation during anodizing (Figure 1.23).

A self-assembly, close-packed 3D ordered lattice of spherical polystyrene particles formed on aluminum was used as a template for the synthesis of 2D/3D composite porous alumina structure on the Al sample [439]. The formation of ordered anodic porous alumina from the aluminum surface covered with a metallic Ta mask was also presented [440].

1.4.1
Aluminum Pre-Treatment

The quality of aluminum substrates and their surface pre-treatment have major influences on the surface nanostructuring by self-organized anodizing. The structure of a pre-existing film on the aluminum surface, which may develop in air, thermally or during chemical and electrochemical treatment, depends on the applied pre-treatment procedure. During the self-organized anodizing of aluminum, the process of pore nucleation is a combination of random nucleation and nucle-
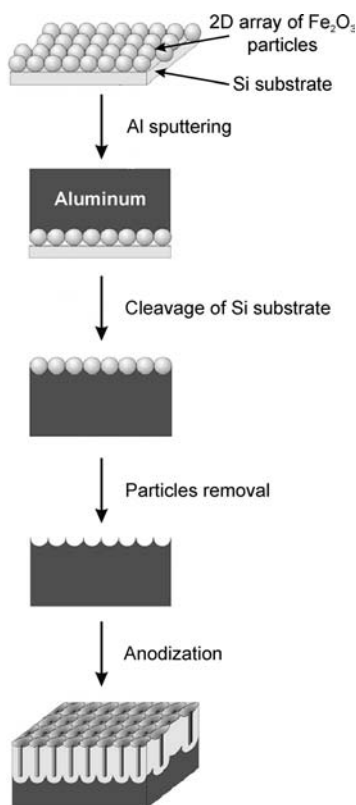
Figure 1.23 Schematic diagram of fabrication of high-ordered anodic porous alumina using a 2D array of spherical monodisperse particles as template. (Reprinted with permission from Ref. [438], © 2006, Wiley-VCH Verlag GmbH & Co. KGaA.)

ation at surface faults. Moreover, the grain boundaries and scratches on the aluminum surface are sites for preferential pore development [440]. The pre-treatment process control must be focused on the reduction of surface faults, or on their controlled and reproducible generation, in the required morphology. Therefore, the most desirable starting material for self-organized nanopore array formation by anodizing is a high-purity, annealed aluminum foil.

The effect of starting material on pore ordering was studied by Terryn *et al.* [441]. Anodic porous film development in sulfuric and phosphoric acids was studied on rolled and AC-grained aluminum, with a similar pore ordering, perpendicular to the surface, being observed. The anodization of relatively pure aluminum and various aluminum alloys was studied in a sulfuric acid solution at 0 °C [442], and the uniformity of oxide growth was seen to increase with the increasing purity of aluminum.

The annealing of foil reduces stresses in the material and increases the average size of the grain [393,443], which is usually more than 100 μm (Figure 1.24). The
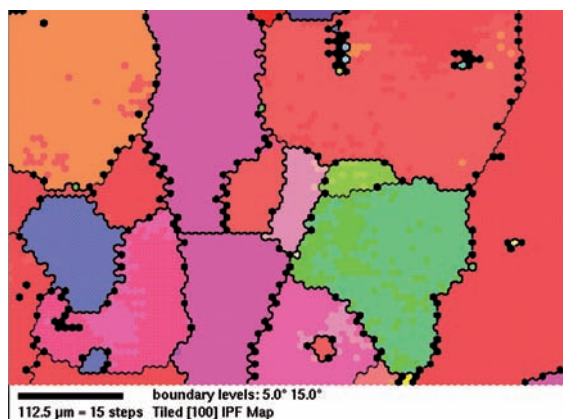
Figure 1.24 Orientation image microscopy (OIM) top-view image of the annealed and electropolished Al surface with marked grain boundaries. The annealing was conducted in an argon atmosphere at 400 °C for 5 h.

typical annealing of aluminum foil is conducted under an argon or nitrogen atmosphere at 400 or 500 °C for 3–5 h.

The degreasing and polishing of Al samples is then carried out before anodizing. Among various solvents used for degreasing, acetone and ethanol are commonly employed. Due to their moderate or high carcinogenicity, dichloromethane [387], trichloroethylene [218], benzene and methanol [444] have been used only sporadically. The immersion of samples in 5% NaOH at 60 °C for 30 s or 1 min and subsequent neutralization in a 1:1 $HNO_3 + H_2O$ solution for several seconds was also proposed for Al degreasing and cleaning [236,309,335,343]. A mixed solution of $HF + HNO_3 + HCl + H_2O$ (1:10:20:69) was also proposed for degreasing and cleaning of the aluminum surface before anodizing, leading to a highly ordered, self-organized nanopore array [403].

The most important step in the pre-treatment of aluminum before anodizing is the polishing of samples. For aluminum, this can be achieved by means of mechanical, chemical, or electrochemical polishing. Mechanical polishing of aluminum has been used rather sporadically to prepare a smooth surface before anodizing [252,390,442]. However, detailed TEM analyses of mechanically polished aluminum have shown the procedure incapable of producing a microscopically smooth and undeformed surface, even when conducted with great care [445]. Chemical polishing of aluminum to prepare surfaces before anodizing may lead to highly ordered nanostructures, and is not widely used (Table 1.11).

A combined chemical–mechanical polishing of aluminum with a slurry containing 0.05-µm Al_2O_3 particles with hydrogen peroxide, citric acid and phosphoric acid, was reported in detail [447].

It should be noted that electrochemical polishing in a 60% $HClO_4 + C_2H_5OH$ (1:4, v/v) solution at 10 °C and 500 mA cm^{-2} for 1 min is commonly used to prepare smooth Al surfaces before anodizing. Other less-frequently used electropolishing

Table 1.11 Chemical polishing of aluminum before anodizing.

Electrolyte	Temperature ($^\circ$C)	Time (min)	Remarks	Reference
70% HNO_3 + 85% H_3PO_4 (15:85)	85	2	Followed by immersing in stirred 1 M NaOH, 10 min, RT	[278]
3.5% H_3PO_4 + 45 g L^{-1} CrO_3	80	10	Followed by electrochemical polishing	[299]
70 mL H_3PO_4 + 25 mL H_2SO_4 + 5 mL HNO_3	85	1.5	After initial mechanical polishing	[446]
91% H_3PO_4 + 98% H_2SO_4 + 70% HNO_3 (75:11:11, v/v) + 0.8 g L^{-1} $FeSO_4$·$7H_2O$	95–100	45–75	Gentle stirring of solution	[333]
70% H_3PO_4 + 20% H_2SO_4 + 10% HNO_3 + 5 g L^{-1} $Cu(NO_3)_2$	–	–	–	[341]
25% NaOH + 20% $NaNO_3$	80	3	–	[220]

^{e}RT: room temperature.

mixtures, together with conditions of electrochemical polishing, are listed in Table 1.12.

An AFM study showed that the typical surface roughness of an electropolished sample is about 20–30 nm on a lateral length scale of 10 μm [443]. The examination of various procedures of pre-treatment of aluminum surfaces, including mechanical polishing or electropolishing, in a standard perchloric acid–ethanol mixture followed by chemical etching was studied in detail [450]. The influence of the electropolishing of aluminum on pore ordering occurring during anodizing was also studied [211,443,451]. Typical SEM images of the aluminum surface after electropolishing in a mixture of perchloric acid and ethanol are presented in Figure 1.25.

Similar stripes and mound patterns formed on the surface during the electrochemical polishing of aluminum were reported elsewhere [185,452–457]. The Al (1 1 0) surface was found to exhibit a regular striped array, whereas on the Al (1 1 1) and Al (1 0 0) surfaces hexagonally ordered patterns were observed. These patterns act as self-assembled masks for nanopore growth in the anodizing process. However, a cellular structure was also observed sporadically on the electropolished aluminum surface [449,450].

Apart from high-purity aluminum foil, the most frequently used starting materials for the anodizing of aluminum have included sputtered or evaporated aluminum on various substrates, including soda-lime glass covered with a tin-doped indium oxide (ITO) [213,363,458–468], Si [298,310–312,321,322,468–485], Ti [486], InP [487] and GaAs [488]. The transfer of nanopore order from anodic porous alumina to semiconductor materials (e.g., Si) is of special interest from the point of view of

Table 1.12 Non-typical conditions of electrochemical polishing of aluminum.

Electrolyte	Temperature (°C)	Current density or potential	Time (min)	Reference(s)
20% $HClO_4$ + 80% C_2H_5OH	0–5	15 V	2	[259]
20% $HClO_4$ + 80% C_2H_5OH	10	20 V	2	[256]
20% $HClO_4$ + 80% C_2H_5OH	10	100 mA cm^{-2}	5	[224,262–265]
$HClO_4$ + C_2H_5OH (1:4, v/v)	7	20 V	1.0–1.5	[241]
	30	160 mA cm^{-2}	3.5	[222]
51.7% $HClO_4$ + 98% C_2H_5OH + Glycerol (2:7:1, v/v)	5	17 V	4	[448]
$HClO_4$ + CH_3COOH (1:4, v/v)	10–15	100 mA cm^{-2}	–	[268]
$HClO_4$ + C_2H_5 OH + 2-butoxyethanol + H_2O (6.2:70:10:13.8, v/v)	10	500 mA cm^{-2}	1	[236]
$HClO_4$ + C_2H_5OH + 2-butoxyethanol + H_2O	10	40 V or 170 mA cm^{-2}	4.5	[305]
H_3PO_4 + C_2H_5OH + H_2O (40:38:25, v/v)	40	5 mA cm^{-2}	2	[393]
H_3PO_4 + $C_4H_{11}OH$ (80:20, v/v)	60–65	10–40 V 30–50 mA cm^{-2}	10–15	[449]
H_3PO_4 + H_2SO_4 + H_2O (4:4:2, v/v)	–	–	–	[384,443]
H_3PO_4 + H_2SO_4 + H_2O (7:2:1, v/v) + 35 g dm^{-3} CrO_3	40	135 mA cm^{-2}	10	[299]

integrating AAO with silicon circuit industrial processes, and the potential application of such structures as biosensors, bioreactors, and magnetic recording media. The main drawback of those methods which employ sputtered or evaporated aluminum is a limited thickness of the aluminum layer. Consequently, the anodizing

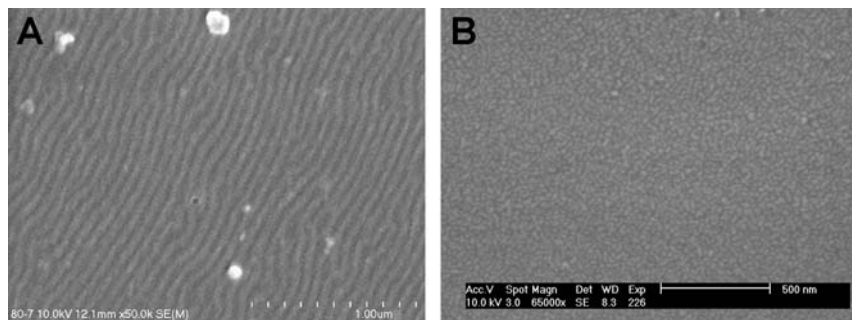

Figure 1.25 SEM top-view images of electropolished aluminum foil with typical stripes (A) and mounds (B) patterns. The electropolishing was conducted in a 60% $HClO_4$ + C_2H_5OH (1:4, v/v) solution at 10 °C and 500 mA cm^{-2} for 1 min.

time required for steady-state growth of pores, and resulting in an ordered arrangement of nanopores, might be not reached before the entire aluminum layer is completely converted into aluminum oxide.

The self-organized anodizing of aluminum was carried out sporadically on aluminum alloys [489,490] or a curved cylindrical sample [491]. In the latter case, cylindrically and pentagonally shaped 3D alumina nanotemplates with hexagonally arranged nanopores were successfully fabricated.

1.4.2
Self-Organized Anodizing of Aluminum

The self-organized growth of ordered pores on anodized aluminum occurs within a relatively narrow window of experimental conditions. Generally, a mild anodizing process leading to porous alumina formation is conducted at low temperatures and employs mainly sulfuric, oxalic, and phosphoric acids as an electrolyte. For each electrolyte, there is a certain range of potential which can be applied for anodizing without burning or breakdown of the oxide film (Table 1.13). Moreover, there is a certain value of the anodizing potential (self-ordering regime) at which, the best arrangement of nanopores is observed. When anodizing is conducted under different values of anodizing potential, the degree of pore ordering is reduced drastically. The temperature of electrolyte and alcohol addition have no influence on the self-ordering regime for the certain anodizing electrolyte. In mild, self-organized anodization, the rate of oxide growth is low due to the low current density, and the highest or most moderate rate of oxide growth is observed in sulfuric acid [448]. More recently, hard anodizing (also known as a high-field anodizing) has been successfully applied for self-organized oxide formation [213,251,499]. In this process the range of anodizing potential and self-ordering values of potentials differ widely (Table 1.13).

The passing current density used during hard anodization is much higher than in mild anodization, and the rate of oxide growth increases about 2500- to 3500-fold [499]. For mild anodizing conducted in phosphoric acid, the rate of oxide growth is about 0.05 to 0.2 μm min^{-1} over a range of anodizing potential from 80 to 195 V, whereas for hard anodizing at 195 V the rate varies between 4 and 10 μm min^{-1}, depending on the applied electric field [339,448]. Thus, in order to avoid any breakdown of the oxide film during hard anodization, aluminum is usually pre-anodized at a constant current density or constant potential for a few minutes. It should be noted that the high-field applied during hard anodizing promotes much evolution of heat, and any excessive heat should be effectively removed from the sample in order to prevent burning.

Following the discovery by Masuda and Satoh [500] of a two-step anodization, the one-step, self-organized anodizing procedure (which resulted in a worse-ordered arrangement of nanopores) is no longer used. Today, a two-step anodizing procedure is commonly used for the formation of high-ordered arrangements of nanopores by anodizing aluminum in sulfuric, oxalic, or phosphoric acid. Following an initial anodization at the pre-selected cell potential, chemical etching of the grown aluminum oxide layer is carried out in a mixed solution containing

Table 1.13 Mild and hard anodization conditions of self-organized anodizing of aluminum and self-ordering regimes.

Mild anodization

Electrolyte concentration (M)	Temperature (°C)	Range of potential (V)	Self-ordering regime (V)	Reference(s)
0.3 H_2SO_4	10	10–25	25	[403,492,493]
2.4 H_2SO_4	1			[216,226,240]
6.0 H_2SO_4	20		18	[494]
0.3 $H_2C_2O_4$	1–5	30–100	40	[403,493,495]
	15–20			[216,241,496]
0.2–0.3 H_3PO_4	0–5	160–195	195	[216,443,497]
H_3PO_4-CH_3OH-H_2O (1:10:89, v/v)	−4			[498]

Hard anodization

Electrolyte concentration (M)	Temperature (°C)	Range of potential (V)	Self-ordering regime (V)	Reference(s)
1.8 H_2SO_4	0	40–70	70	[213,251]
0.03–0.06 $H_2C_2O_4$	3	100–160	160	[213]
0.3 $H_2C_2O_4$	1	110–150	120–150	[499]
0.1 H_3PO_4	0	195–235	235	[213]
H_3PO_4-C_2H_5OH-H_2O (v/v 1:20:79)	−10 to 0	195	195	[339]

H_3PO_4 (6 wt.%) and H_2CrO_4 (1.8 wt.%) at a temperature of 60–80 °C (e.g., Refs. [226,231,240,248,318,407,409,493,498]). A slightly modified composition of solution consisting of 0.4 or 0.5 M H_3PO_4 and 0.2 M H_2CrO_4 was also proposed for the oxide removal [235,496,501]. The time required for the chemical etching of oxide depends heavily on the thickness of the oxide film grown during the first anodization, and can vary from a few minutes to several hours. It should be noted that the rate of oxide growth during anodization depends significantly on the anodizing electrolyte, with the highest rate being observed for sulfuric acid anodizing. A completely different method for the removal of oxide formed during the first-step of anodization was proposed by Schneider *et al.* [502]. This method employs a voltage detachment procedure, whereby a reverse voltage is applied to the anodized sample (the value of the reverse voltage is the same as was used for the anodization). Such a voltage detachment procedure allows the production of a fully flexible anodic porous alumina membrane, as opposed to oxide removal by chemical etching. The enhanced mechanical flexibility of the membrane is an undeniable advantage of the voltage detachment procedure over the chemical etching. One application of the electrochemical voltage pulse technique for the effective detachment of oxide layer at various electrolytes was investigated systematically [503]. The procedure results in a freestanding detached AAO membrane with open pores. The proposed mechanism of the pulse detachment involved oxide removal independently of the applied procedure, and resulted in the formation of a periodic concave pattern on the aluminum surface, which acted as a mask for the second anodizing. Following oxide removal, a second anodization is carried out at the same anodizing potential as used for the first anodization. Selected procedures of two-step anodization of aluminum resulting in a high-order arrangement of nanopores are detailed in Table 1.14.

A three-step anodizing procedure, consisting of two full cycles of pre-anodization and subsequent oxide removal, was verified as a method of self-organized nanopore arrangement in oxalic [236,390] and sulfuric acid [407]. The duration of each anodizing step is usually different. For example, times for the first, second, and third anodizations in three-step anodizing in oxalic acid were fixed at 10 min, 690 min and 3 min, respectively [236]. It was fount that, for the three-step anodization, the order of self-assembled nanopores is comparable with the arrangement of pores obtained by the two-step anodizing process [390,407]. Brändli *et al.* [512] investigated the effect of multi-step anodization in oxalic acid on a long-range uniformity in pore diameter, with the anodization and oxide dissolution cycles being repeated even three or four times; however, a rather disordered nanopore structure was obtained. It was also found that increasing number of anodization–etching cycles led to an increase in the uniformity of pore size and pore diameter.

1.4.2.1 Structural Features of Self-Organized AAO

The structural features of anodic porous alumina formed by anodization under a potentiostatic regime depend on the electrolyte and the applied anodizing potential. The interpore distance of the AAO lattice formed by the self-organized anodization depends heavily on the anodizing potential. Figure 1.26 includes SEM images of the pore arrangements with the same magnification, taken from the bottom of pores

Table 1.14 Selected procedures of two-step anodizing of aluminum conducted in sulfuric, oxalic, and phosphoric acids.

Electrolyte	Temperature (°C)	Potential (V)	Time of first anodization (min)	Mixture type*	Temperature (°C)	Time (min)	Time (min)	Oxide thickness (μm)	References(s)
					Oxide removal		Second anodization		
0.3 M H_2SO_4	10	25	1320	A	60	–	5940	~200	[493]
1.1 M H_2SO_4	1	19	1440	A	60	600	5700	200	[504]
2.4 M H_2SO_4	1	15–25	10	A	60	10–15	870–45	90	[240,248]
							1240–125	140	[407]
6–8 M H_2SO_4	0–20	18	60	A	–	–	5	0.6	[494]
0.2 M $H_2C_2O_4$	18	40	1800	A	60	–	50	–	[505]
0.3 M $H_2C_2O_4$	0	40	20	B	60	5	120	10	[506]
	0–25		600	C	65	720	60	–	[496]
	1		1440	A	60	600	5700	200	[504]
	10		120	A	60	240	2–10	0.2–1.3	[507]
	15		900	A	65	–	10–600	–	[390]
	17		600	A	60	840	5	0.7	[500]
	20		40	A	65	10–20	120	–	[508]
	24		300	A	60	600	5	1.0	[509]
0.5 M $H_2C_2O_4$	5–30	20–60	120–740	A	65	60–240	740	–	[241]
0.15–0.5 M $H_2C_2O_4$	5	40	1320	A	60	–	5940	~170	[493]
0.15 M H_3PO_4	5	10–60	1200	D	–	–	30	1.2–1.5	[495]
0.5 M H_3PO_4	2	195	1440	A	60	600	1200	110	[510]
	0	140	120	A	60	240	5–10	–	[511]
H_3PO_4-CH_3OH-H_2O (1:10:89, V/v)	–4	195	1200	A	80	–	1200	~100	[498]

*Mixture types: A: phosphoric acid (6 wt %) and chromic acid (1.8 wt %); B: 0.4 M phosphoric acid and 0.2 M chromic acid; C: 0.5 M phosphoric acid and 0.2 M chromic acid; D: phosphoric acid.
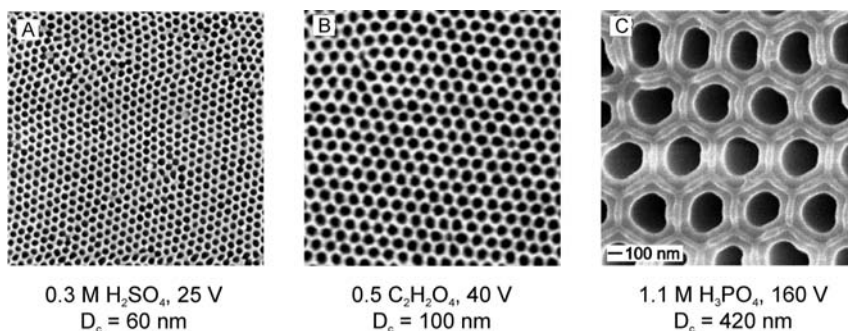
0.3 M H$_2$SO$_4$, 25 V
D$_c$ = 60 nm

0.5 C$_2$H$_2$O$_4$, 40 V
D$_c$ = 100 nm

1.1 M H$_3$PO$_4$, 160 V
D$_c$ = 420 nm

Figure 1.26 SEM bottom-views of porous anodic alumina with hexagonally arranged nanopore structures after opening pore bottoms. Nanostructures were formed by self-organized anodization in different electrolytes at 10 °C (A), 5 °C (B) and 3 °C (C). (Reprinted with permission from Ref. [493], 1999, AVS The Science & Technology Society.)

after their opening, and the interpore distance values of nanostructures. The high-ordered anodic porous alumina films were obtained by the two-step anodizing in sulfuric, oxalic, and phosphoric acid solutions under potentials of 25, 40, and 160 V, respectively. Pores formed in sulfuric, oxalic and phosphoric acid were opened by immersing in 5 wt.% phosphoric acid at 30 °C for 30 min, 35 °C for 30 min, and 45 °C for 30 min, respectively.

SEM bottom-views of the AAO layers synthesized in the same electrolyte, but at various anodizing potentials, are presented in Figure 1.27. The increasing anodizing potential is seen to increase the interpore distance.

The typical range of potentials used for anodizing or hard anodizing (dotted arrows) and corresponding interpore distances for various electrolytes are presented in Figure 1.28. The diagonal of the graph denotes the theoretical dependence of interpore distance on anodizing potential according to Eq. (5).

Irrespective of the type of electrolyte used, the linear relationship between the anodizing potential and interpore distance of the formed nanostructures is clearly visible. Each electrolyte is related with a specific range of anodizing potential and corresponding interpore distance of the anodic porous alumina film. The interpore distance of the formed nanostructure can be controlled over the whole range of nanometric scale by choosing an appropriate anodizing electrolyte and corresponding anodizing potential. It should be pointed out that the type of electrolyte used for anodizing is directly related with the operating conditions, including the anodizing potential, the concentration of electrolyte, and the temperature. On the other hand, the structural features of anodic porous alumina are dependent upon conditions used for anodizing. Selected operating conditions commonly used for anodizing of aluminum are presented in Tables 1.15, 1.16 and 1.17 for sulfuric, oxalic, and phosphoric acid anodizing, respectively.

In addition, the characteristic features of fabricated nanostructures including pore diameter, interpore distance, porosity and pore density of the nanostructure, are also collected in Tables 1.15–1.17. The operating conditions of anodization and
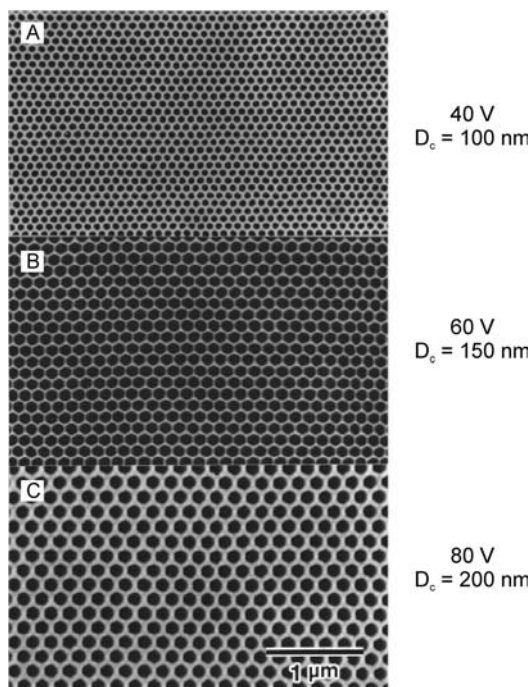
Figure 1.27 SEM images of perfectly ordered porous anodic alumina formed from pre-textured Al at different anodizing potential in 0.3 M oxalic acid at 17 °C (A and B) and 3 °C (C). (Reprinted with permission from Ref. [420], © 1997, American Institute of Physics.)

Figure 1.28 Anodizing potential influence on the interpore distance for anodic porous alumina formed in various electrolytes. Dotted arrows for phosphoric, oxalic and sulfuric acids corresponds to hard anodizing conditions. (Data for glycolic, malonic, tartaric, malic and citric acids were taken from Refs. [211,213].)

Table 1.15 Structural features of nanostructures obtained by anodizing in H_2SO_4 at various anodizing conditions.

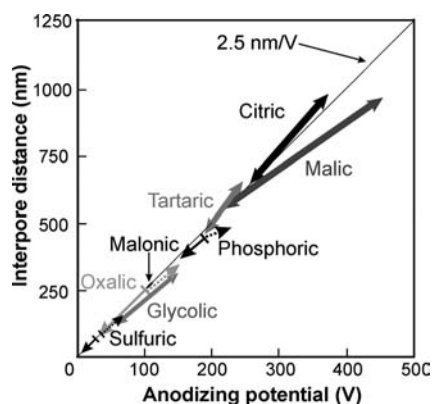| Concentration (M)	Temperature (°C)	Potential (V)	D_p (nm)	D_c (nm)	α (%)	n (1 cm^{-2})	Remarks	Reference(s)
0.18	10	25	24	66.3	12.0	2.63×10^{10}	2-step	[235,493]
0.3	10	25	n.a.	60	n.a.	3.2×10^{10}	1-step, volume expansion factor: 1.40	[403]
0.5–4.0	10–40	3–18	12–18	18.1–47.9	41.0–13.0	$3.2\text{–}0.5 \times 10^{11}$	1-step	[238]
1.1	5	25	36	64	28.7	2.8×10^{10}	2-step	[502]
1.0–1.5	20	2–20	9.4–16.0	17.8–50.3	29.3–10.5	n.a.	1-step	[249,513]
1.53	18	15	13.5	40.5	10.1	8.1×10^{10}	1-step, rate of oxide growth: ~330 nm/min	[448]
1.7	n.a.	10–15	10–20	n.a.	n.a.	n.a.	1-step, poor periodicity	[514]
1.8	0.1–5	15–25	10–20	44.8–65.0	4.5–8.6	$5.8\text{–}2.7 \times 10^{10}$	1 step	[251]
1.8	0.1	40–70	30–50	90–130	10.0–13.5	$1.4\text{–}0.7 \times 10^{10}$	1-step, hard anodizing,	[213,251]
2.4	−8 to 10	15–25	13.4–27.0	39.7–68.7	10.3–20.5	$7.3\text{–}2.4 \times 10^{10}$	2-step	[240,248,407,409]
6.0–8.0	0 or 20	18	30	45	40.3	5.7×10^{10}	2-step	[494]

D_P: pore diameter;
D_c: interpore distance;
α: porosity;
n: pore density;
n.a.: data not available.

Table 1.16 Structural features of nanostructures formed by anodizing in $H_2C_2O_4$ at various anodizing conditions.

Concentration (M)	Temperature (°C)	Potential (V)	D_P (nm)	D_c (nm)	α (%)	n (1 cm^{-2})	Remarks	Reference(s)
0.03–0.06	3	100–160	50–100	220–440	4.7	0.24–0.06×10^{10}	1-step, hard anodising	[213]
0.15	−1	70	90.4	n.a.	26.9	0.42×10^{10}	1-step	[253,515]
	16		87.4		21.9	0.36×10^{10}		
0.15	5	10–60	11–39	40.6–141	6.6–6.9	7.0–0.6×10^{10}	2-step	[495]
0.5		40	27	95	8.1	1.3×10^{10}		
0.2	18	40	40	103	13.7	1.2×10^{10}	1-step, rate of oxide growth: ~71 nm min^{-1}	[448]
0.2	18	40	43.8	104.2	16.0	1.1×10^{10}	2-step	[505]
0.3	1	110–150	49–59	220–300	3.3–3.4	1.3–1.9×10^{10}	Hard anodization	[499]
0.3	1	40	31	105	8.0	1.05×10^{10}	2-step, rate of oxide growth: 28.6 nm min^{-1} ordered domains: 1–5 μm^2	[235,493]
0.3	15	20–60	n.a.	49.8–159.8	n.a.	4.6–0.45×10^{10}	2-step, rate of oxide growth for 40 V: $-147.75 + 125.53t$ [nm min^{-1}]	[241]
		40	24	109	4.4	0.97×10^{10}		
0.3	15	40	63	100	36.0	1.15×10^{10}	3-step, ordered domains: 0.5–2 μm^2	[390]
0.3	20	40	50	92	26.8	1.36×10^{10}	2-step	[509]
0.3	30	2–40	11.5–34.2	20.3–97.3	31.4–12.5	n.a.	1-step	[249,513]
0.34	15	40	60	104	31.6	1.12×10^{10}	3-step, ordered domains: ~4 μm^2	[236]
0.45	5	40–50	36–57	105–114	10.7–22.7	1.05–0.89×10^{10}	2-step	[502]
0.45–0.9	10–40	3–20	14.5–21.1	20.5–54.5	45.7–13.7	3.1–0.4×10^{11}	1-step	[237]
		20–40	21.1–37.7	54.5–110.7	13.7–10.6	0.4–0.1×10^{11}		
0.63	20–40	4–36	7.3–18.5	n.a.	32.0–10.4	19.1–0.97×10^{20}	1-step	[406]

D_P: pore diameter;
D_c: interpore distance;
α: porosity;
n: pore density;
n.a.: data not available.

Table 1.17 Structural features of nanostructures formed by anodizing in H_3PO_4 at various anodizing conditions.

Concentration (M)	Temperature (°C)	Potential (V)	D_p (nm)	D_c (nm)	α (%)	n (1 cm^{-2})	Remarks	Reference(s)
0.04–0.4	−1 to 16	160	170–200	n.a.	14.0–26.0	5.0×10^{12}	1-step	[515]
0.1–0.25	0	195–235	130–n.a.	420–480	8.7–n.a.	6.5–n.a. $\times 10^{8}$	1-step, hard anodizing	[213]
0.1	3	195	158.4	501	9.0	4.6×10^{8}	1-step	[235,493]
0.3–1.1	0	195	n.a.	500	n.a.	4.6×10^{8}	1-step	[497]
0.4	25	80	80	208	13.4	3.1×10^{9}	1-step, rate of oxide growth: $\sim$55.6 nm min^{-1}	[448]
0.4	25	5–40	20.8–74.7	23.5–105.4	80.0–50.5	n.a.	1-step	[249]
0.42	23.9	20–120	33	73–274		18.9–0.9×10^{9}	1-step, pore diameter constant	[197]
0.42	25	87–117.5	64–79	236–333	n.a.	n.a.	1-step	[232]
0.53	n.a.	40–120	60–200	n.a.	n.a.	n.a.	1-step, rate of oxide growth: 1–2 nm min^{-1}, poor periodicity	[514]
1.1	3	160	n.a.	420	n.a.	6.5×10^{8}	1-step, volume expansion factor: 1.45	[403]
H_3PO_4-CH_3OH-H_2O (v/v 1:10:89)	−4	195	200	460	17.1	5.5×10^{8}	2-step, ordered domains: 1–5 μm^2	[498]
H_3PO_4-C_2H_5OH-H_2O (v/v 1:20:79)	−10 or −5	195 (at current density 150–400 mA cm^{-2})	80–140	380–320	4.0–17.4	8.0–11.3×10^{8}	2-step, hard anodizing, rate of oxide growth: 4–10 μm min^{-1}, anodizing ratio: 0.62 nm V^{-1}	[339]
0.42 M H_3PO_4 + 0.5–1% Hydracrylic triprotic carboxylic acid + 0.05–0.1% Cerium salt	15–20	120–130	100–200	n.a.	9.0–43.3	1.1–1.4×10^{13}	1-step	[219,516]

D_p: pore diameter;
D_c: interpore distance;
α: porosity;
n: pore density;
n.a.: data not available.

corresponding structural features of anodic porous alumina films for infrequently used electrolytes, such as chromic, glycolic, malic, tartaric, citric and malonic acids or mixed sulfuric and oxalic acids, are listed in Table 1.18.

An analysis of the data contained with Tables 1.15–1.18 shows that the highest density of nanopores can be obtained by anodizing in sulfuric acid. Anodization carried out in other electrolytes results in a lower pore density of the anodic porous alumina film. It should be noted that the pore diameter is less strictly related to the anodizing potential than the interpore distance, and is seen to differ slightly even for the same anodizing conditions. Consequently, there is no consistency among the porosity of nanostructures obtained under the same anodizing conditions. This can be attributed to various concentrations of the electrolyte, or to various hydrodynamic conditions of anodizing. It is generally accepted that stirring of the electrolyte during anodization is an unquestionable necessity for in order to form ordered hexagonal nanostructures [221,236,366,443]. Indeed, without stirring the electrolyte the temperature at pore bottoms increases significantly [236]. Subsequently, in the event of weak heat abstraction, breakdown of the oxide film or its anodic dissolution can easily occur, especially during anodization at high potential or high electric field (hard anodization). Furthermore, the electrolyte composition at pore bottoms differs from the bulk electrolyte [366,443]. In general, with an increasing speed of electrolyte stirring and decreasing concentration of the acidic solution used for anodizing, a shift of the self-ordering regime occurs and higher values of anodizing potentials can be applied (compare mild and hard anodizations in Table 1.13) [494]. On the other hand, an increasing concentration of acid, especially in combination with a high anodizing temperature or a long process duration, greatly enhances the chemical etching of oxide; the result of this is that a significant widening of pores occurs.

The effect of electrolyte temperature on interpore distance, pore diameter, wall thickness and barrier layer thickness of anodic porous alumina formed by two-step anodizing in 2.4 M H_2SO_4 is illustrated graphically in Figure 1.29. These data were collected in the range of anodizing potential from 15 to 25 V for two different geometries of the electrochemical cell. A simple double-wall cell with magnetic stirring [240,248] and overflow cell with a pump system [407,409] were used for anodizing aluminum over a range of temperatures from -8 to $10\,^\circ$C. For the overflow cell, anodizations were conducted only at a temperature of $1\,^\circ$C. With increasing temperature of the electrolyte, however, the range of anodizing potential narrows such that, at $10\,^\circ$C, the self-ordering of nanopores is observed only between 17 and 25 V.

An analysis of the data presented in Figure 1.29 shows that the interpore distance and barrier layer thickness do not vary significantly with the temperature of anodization. Moreover, the different geometry of the set-up, resulting in the different hydrodynamics conditions, does not have any considerable influence on the interpore distance and barrier layer thickness. These experimental data are in a close agreement with the theoretical predictions calculated from Eqs. (5) and (15). For the pore diameter and wall thickness, such good consistency between the experimental values is not observed, and the data differ depending on the anodizing temperature. In general, increasing the temperature of the electrolyte leads to an increase in pore

Table 1.18 Structural features of nanostructures formed by anodizing in a non-commonly used electrolytes at various anodizing conditions.

Electrolyte	Temperature (°C)	Potential (V)	D_P (nm)	D_c (nm)	α (%)	n (1 cm^{-2})	Remarks	Reference(s)
0.3 M H$_2$SO$_4$ + 0.3 M H$_2$C$_2$O$_4$	3	20–48	n.a	50–98	n.a.	4.6–1.2 × 10^{10}	1-step, best ordering at 36 V	[222]
0.026–0.044 M H$_3$PO$_4$ + 0.023–0.11 M H$_2$C$_2$O$_4$ + 0.023–0.14 M H$_3$PO$_2$ + 3.4 × 10^{-3} M Na$_2$WO$_4$	35	120	250–500	350–650	n.a.	3.0–7.0 × 10^8	1-step, various compositions of electrolytes were studied, rate of oxide growth: 2.33 μm min^{-1}, barrier layer thickness 400–500 nm	[220]
0.3 M Chromic acid	40	5–40	17.1–44.8	25.6–109.4	44.6–17.0	n.a.	1-step	[249]
0.3 M Chromic acid	60	45	23–50	74–17	n.a.	2.3–2.8 × 10^{10}	1-step, stepwise increase in potential, random pores	[218]
0.44 M Chromic acid	n.a.	40	70–100	n.a.	n.a.	n.a.	1-step	[514]
1.3 M (10%) Glycolic acid	10	50–150	35–n.a.	150–320	10.1–n.a.	5.1 × 10^9	1-step or 2-step	[213]
0.13 M (2%) Tartaric acid	1–5	235–240	n.a.	630–650	n.a.	2.9–2.7 × 10^8	1-step	[213]
3 M Tartaric acid	5	195	n.a.	500	n.a.	4.6 × 10^8	1-step	[211]
0.15–0.3 M (2–4%) Malic acid	10	220–450	n.a.	550–950	n.a.	3.8–1.3 × 10^8	1-step	[213]
0.1–0.2 M (2–4%) Citric acid	20	270–370	n.a.	650–980	n.a.	2.7–1.2 × 10^8	1-step	[213]
0.125–0.15 M Citric acid	21	260–450	130–250	650–1100	n.a.		1-step, Al on Si, anodizing ratio: 1.1 nm V^{-1}	[217]
2 M Citric acid	20	240	180	600	10.0	3.2 × 10^8	1-step, rate of oxide growth: 0.12 μm min^{-1}	[216]
0.1 M Malonic acid	20	150	n.a.	n.a.	10.0	n.a.	1-step	[230]
5.0 M Malonic acid	5	120	n.a.	300	n.a.	1.3 × 10^9	1-step	[211]
γ-butyrolactone + ethylene glycol (9:1) + 0.9% H$_2$O	RT^a	250–500	n.a	275–550	n.a.	n.a.	1-step, anodizing ratio: 0.8 nm V^{-1}, random order	[295,517]
0.3 M Na$_2$B$_4$O$_7$	60	60	up to 235	n.a.	32.0	2.5 × 10^{14}	1-step, pH = 9.2, random pores, rate of oxide growth: 60 nm min^{-1}	[201]

D_P: pore diameter;
D_c: interpore distance;
α: porosity;
n: pore density;
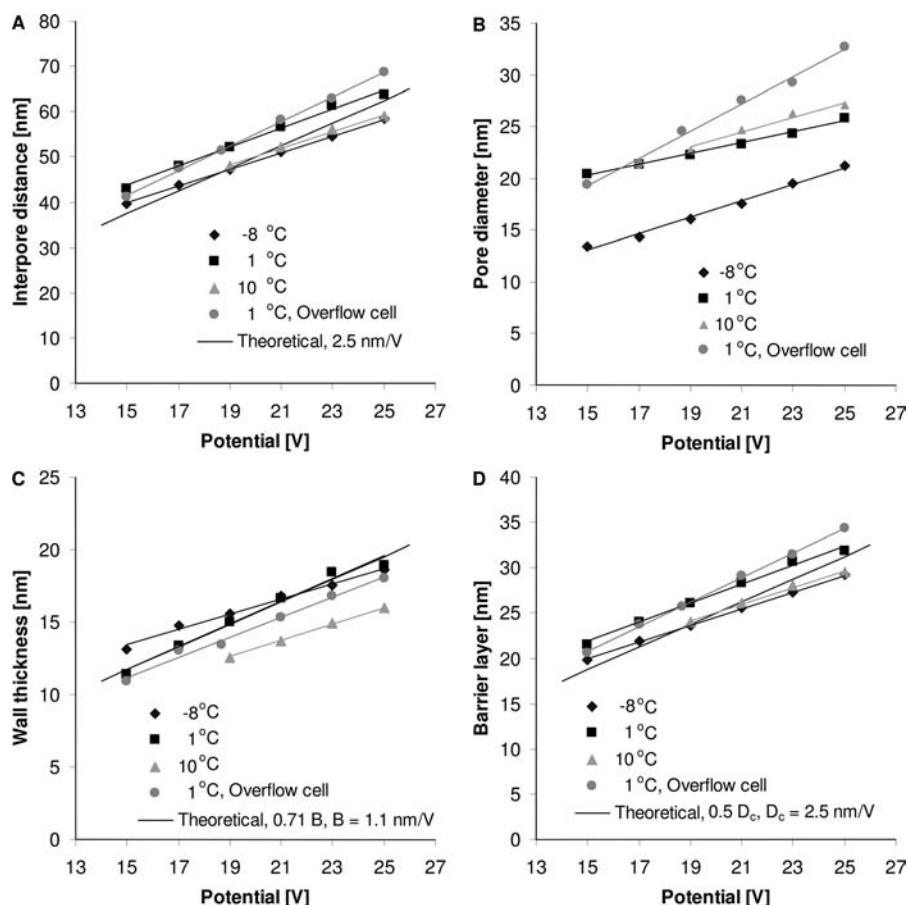n.a.: data not available;
RT: room temperature.

Figure 1.29 Average interpore distance (A) pore diameter (B), wall thickness (C) and barrier layer thickness (D) versus anodizing potential at various temperatures. The anodization in the overflow cell and double-wall cell with magnetic stirrer was carried out in 2.4 M H$_2$SO$_4$.

diameter and a decrease in wall thickness. Due to the slow chemical dissolution of oxide occurring at $-8\,°C$, the smallest pore sizes were obtained. Consequently, the thinnest cell walls are observed at the highest studied temperature. Since porosity depends on the pore diameter according to Eq. (19), the observed changes in pore diameter at different anodizing temperatures should also be indicated in the calculated porosity of the nanostructure.

The influence of temperature on the porosity and pore density of self-organized anodic porous alumina formed in various electrochemical cells and temperatures are presented in Figure 1.30.

Indeed, the data in Figure 1.30 indicate that the porosity of anodic alumina varies between 10 and 20% in the whole range of the anodizing potential, and for all
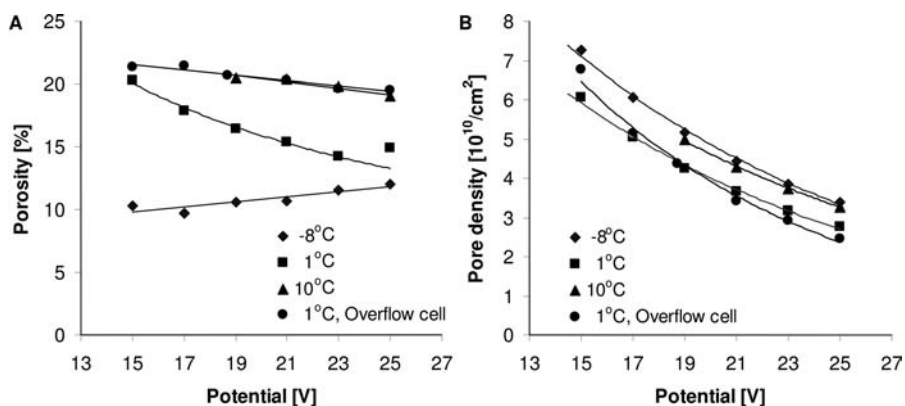
Figure 1.30 Porosity (A) and pore density of the nanostructure (B) versus anodizing potential at various temperatures. The anodization in the overflow cell and double-wall cell with magnetic stirrer was carried out in 2.4 M H$_2$SO$_4$.

studied temperatures. With increasing anodizing potential, both behaviors – an increase and decrease in porosity – were observed. As might be expected from Eq. (25), the pore density decreases with increasing anodizing potential for all temperatures.

The current density recorded during steady-state growth of anodic porous alumina in 2.4 M sulfuric acid under a constant potential regime shows an exponential dependency on the anodizing potential (Figure 1.31A).
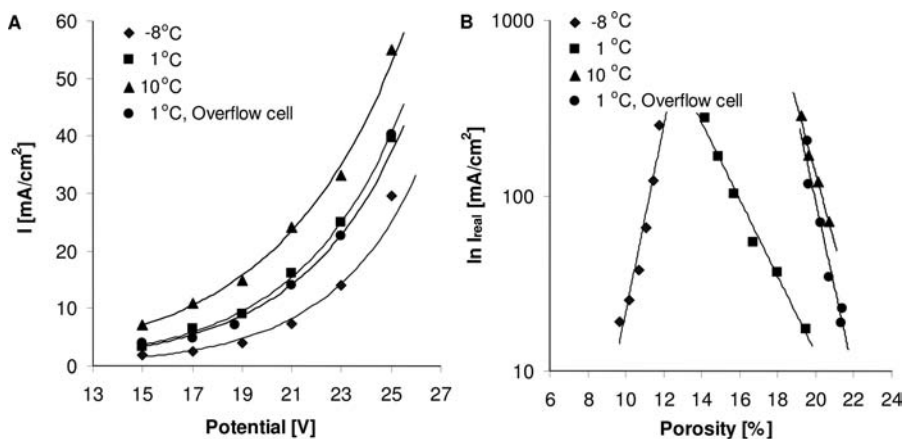

Figure 1.31 Dependence of steady-state current density on anodizing potential (A) and ln I_{real} on porosity of nanostructure (B) at various temperatures. The anodization in the overflow cell and double-wall cell with magnetic stirrer was carried out in 2.4 M H$_2$SO$_4$.

Although the increasing temperature increases the current density of the porous oxide growth, a different hydrodynamics flux in electrochemical cells does not have any significant influence on the steady-state current density. It is widely recognized that the current density accompanied by steady-state growth of the porous oxide film is related exponentially with the electric field strength, defined as a ratio of forming potential to barrier layer thickness. Therefore, the recorded steady-state current density at 1 °C is similar for different electrochemical cells. Due to the porosity of the anodic film, the real current density at the bottom of the pores is much higher than recorded. The real current density, I_{real}, as the ratio of average current density for the certain anodizing potential to the porosity of nanostructure, shows a linear dependency on the porosity of nanostructure (Figure 1.31B).

The structural features of anodic porous alumina formed in 2.4 M H_2SO_4 (especially pore diameter) depend on the electrolyte temperature as, with increasing temperature, an enhanced oxide dissolution is observed (Figure 1.32).

As a result, a considerable widening of pores occurs at the higher anodizing potential. The 3D SEM top-view image of anodic porous alumina formed at 25 V shows that, at this particular magnification, nanostructures do not exhibit defects in the nanopores arrangement. The distances between neighboring pores and pore diameter are fully uniform over the analyzed surface area for the temperature of
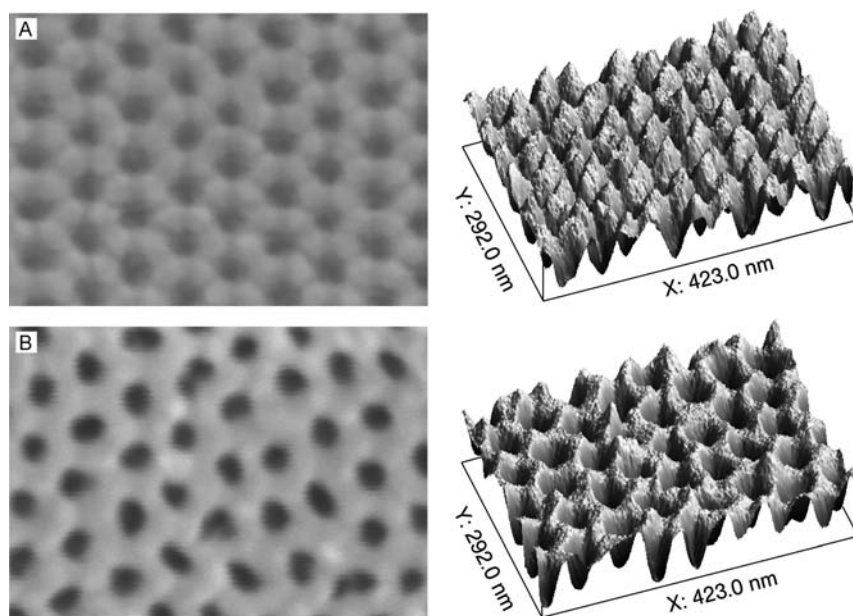
Figure 1.32 SEM top-view and 3D images for the anodic porous alumina surface formed at −8 °C (A) and 10 °C (B). The two-step anodization in the double-wall cell with magnetic stirrer was carried out in 2.4 M H_2SO_4 under 25 V. (Reprinted with permission from Ref. [240], © 2007, Elsevier Ltd.).

$-8\,°C$. At a temperature of $10\,°C$, however, a variation is indicated in pore diameter over the surface area (Figure 1.32B). Moreover, the pores are reasonably wider than those observed at $-8\,°C$, a finding which is especially apparent in the 3D SEM image, where the surface of the sample anodized at $10\,°C$ is smoother due to the enhanced chemical etching of oxide. Uniformity of the pore diameter and interpore distance were also analyzed with, for all studied temperatures, 1000 independent measurements of pore diameter and interpore distance being carried out from SEM top-views images of anodic porous alumina formed under various cell potentials. The collected values of the pore diameter and interpore distance, for each of the anodizing potentials, were classified into seven groups and distribution diagrams were constructed for all studied temperatures. The typical pore size and interpore distance distribution diagrams obtained for an anodizing potential of 19 V at various temperatures are shown in Figure 1.33.

In order to obtain a better understanding of the influence of temperature on uniformity of pore diameter and interpore distance, the breadths of the distribution diagram (being a maximum difference between extreme values), were calculated from the diagrams and are collected in Table 1.19. Most importantly, it should be noted that for anodizations carried out at $10\,°C$ under 15 and 17 V, the pore growth was not exhibited on the surface. Rather, a fiber-like oxide or porous random oxide structure was formed on the top of anodized aluminum surface.

In general, the breadth of distribution diagrams at -8 and $1\,°C$ decreases with increasing anodizing potential, over the range of potentials between 15 and 23 V. A further increase in anodizing potential to 25 V causes a slight increase in the breadth of the distribution diagrams. At an anodizing temperature of $10\,°C$, there is no a direct relationship between anodizing potential and the breadth of the diagram. This can be explained in terms of the enhanced chemical dissolution of oxide at $10\,°C$ and, consequently, a significant change in pore diameter. Thus, the uniformity of pore diameter is heavily affected by the chemical attack of acid.

It is generally accepted that whilst the duration of anodizing influences the pore diameter, the cell size stays unchanged [223]. With increasing anodizing time an increase in pore sizes was observed elsewhere (e.g., Refs. [201,223,233,255,408]). The pore diameter increases with anodizing time due not only to the chemical dissolution of oxide but also to the coalescence and formation of stable pore walls [223]. The anodizing duration also alternates the regularity of the self-organized anodic porous alumina structure. An improvement in nanopore arrangement and an increase in the average size of the domains exhibiting an ideally arranged pore structure, were observed with increasing anodizing time for sulfuric [216,407,492], oxalic [216,518], phosphoric [216,497], and malonic acid [211] solutions. Thus, an extended anodizing time improves the regularity of nanopore arrangement and produces the ideally arranged triangular lattice. Moreover, the extended anodizing not only rearranges the cells but also reduces the number of defects and dislocations in the nanostructure. In contrast, Nielsch *et al.* [235] found that on extending the anodizing time from 24 to 48 h, the size of ordered domain decreased for the anodization conducted in 0.1 M H_3PO_4.
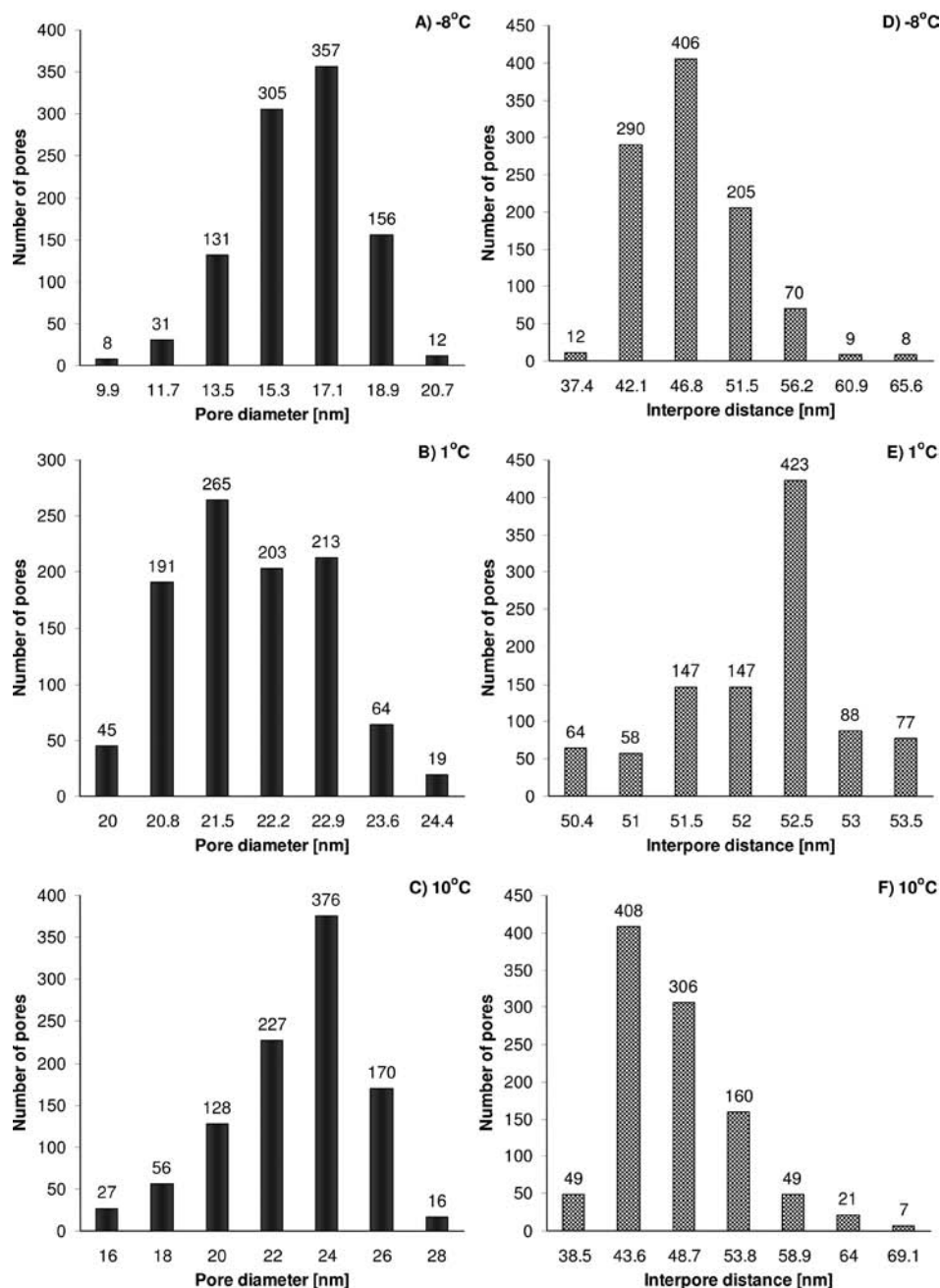
Figure 1.33 Pore size and interpore distance distribution diagrams of anodic porous alumina formed under 19 V at various temperatures: $-8\,°C$ (A and D), $1\,°C$ (B and E) and $10\,°C$ (C and F). The two-step anodization in the double-wall cell with magnetic stirrer was carried out in $2.4\,M\ H_2SO_4$.

Table 1.19 Distribution diagrams breadth at various temperatures and anodizing potentials.

| | Breadth of the distribution diagram (nm) | | | | | |
| | Pore diameter | | | Interpore distance | | |
Potential (V)	−8 °C	1 °C	10 °C	−8 °C	1 °C	10 °C
15	14.0	5.7	–	35.0	3.7	–
17	14.0	6.3	–	34.6	2.4	–
19	12.6	5.1	13.0	32.9	3.6	35.7
21	10.4	4.9	18.2	32.9	3.1	31.4
23	6.3	4.2	19.6	30.1	2.8	33.6
25	11.5	4.9	15.3	37.0	2.7	34.6

The two-step anodization in double-wall cell with magnetic stirrer was carried out in 2.4 M H_2SO_4. (Reprinted with permission from Ref. [240]; © 2007 Elsevier Ltd.).

1.4.2.2 Order Degree and Defects in Nanopore Arrangement

The broad range of various applications of the high-ordered, self-organized anodic porous alumina requires close control of the nanopore arrangement over a large surface area. From the nanoengineer's perspective, one of the most desired material is a close-packed nanostructure with a perfect arrangement of uniform pores. Therefore, the avoidance of defects formation in self-organized anodic porous alumina and a subsequent strict analysis of ordering degree in the nanostructure is extremely important. The two-step anodization of aluminum, conducted under precisely selected operating conditions including the specific self-ordering regime of anodizing potential, can lead to perfectly arranged nanostructures. In the case when operating conditions are fixed differently from the self-ordering regime, the hexagonal arrangement of nanopores is disturbed and some defects appears. An analysis of the order degree of nanopore arrangement can be performed from images of the anodized aluminum surface, or from images showing the pore bottoms. It should be noted that the order degree determined from the surface of anodized aluminum is usually slightly worse than the order at the pore bottoms. This difference is attributed to the rearrangement of pores occurring at the metal/oxide interface during the anodic porous alumina growth.

SEM images taken from the anodized surface and pore bottoms, together with 2D fast Fourier transforms (FFTs) and average profiles along the intensity of the 2D FFT image, are shown in Figure 1.34. The two-step, self-organized anodizing of aluminum was performed in 2.4 M H_2SO_4 under 21 V at 1 °C.

The regular triangular nanopore array with a limited number of defects in the pore arrangement is clearly visible in SEM images, and proven by 2D FFT images. The Fourier transform of the lattice provides useful information about the periodicity of the structure in the inverse scale. For a perfectly triangular lattice, a FFT pattern should consist of six distinct spots on the edges of a hexagon. When the order of the lattice is worse, ring-shaped or even disc-shaped forms can appear in the FFT image. The non-perfect regularity of the nanostructure shown in Figure 1.34 is
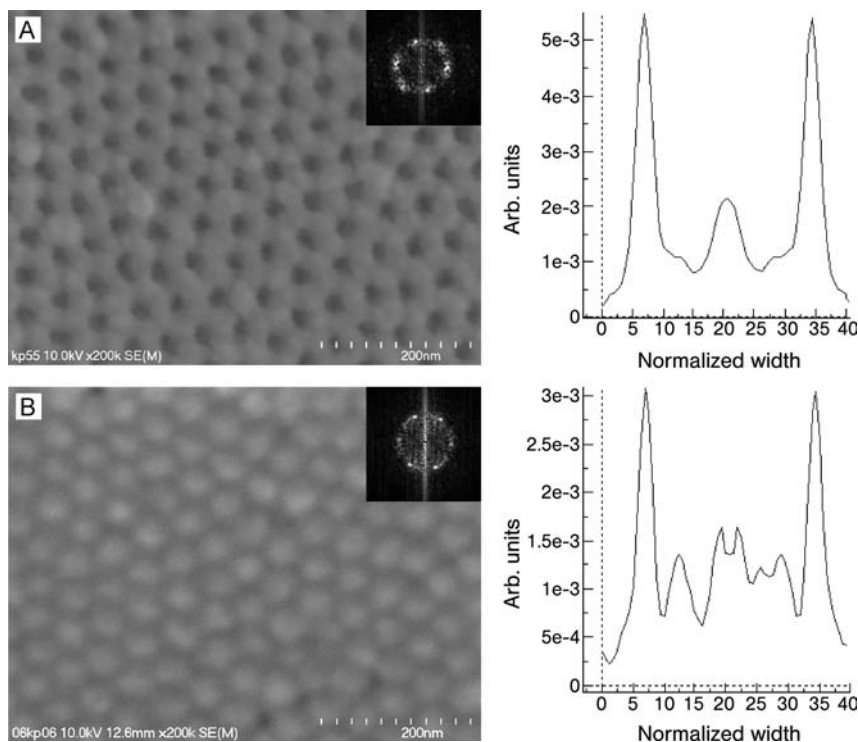
Figure 1.34 SEM top (A) and pore bottom (B) views of anodic porous alumina layer with 2D FFT images and profile analyses of the FFT intensity. The two-step anodization in the double-wall cell with magnetic stirrer was carried out in 2.4 M H_2SO_4 under 21 V at 1°C.

indicated in the ring-shaped pattern of the 2D FFT. The higher order degree at the pore bottoms appears as distinctly marked spots in the 2D FFT image (Figure 1.34B), and narrower main peaks in the average profile along the intensity of the FFT image.

The cross-section of anodic porous alumina layer formed by two-step, self-organized anodizing in 2.4 M H_2SO_4 at 21 V shows a net of parallel straight channels (Figure 1.35A). In order to observe a channel structure of holes grown in the anodized layer, a He^+ ion beam was transmitted vertically through the anodic layer with open pores, and dissipation of the beam after membrane transmission was analyzed. In the dissipation diagram (Figure 1.35B), a relatively narrow peak proves that channels formed during anodizing are both straight and parallel.

A two-step, self-organizing anodization of aluminum in sulfuric acid can result in the perfect triangular arrangement of nanopores. Figure 1.36A shows the SEM-top view of anodic porous alumina formed in sulfuric acid at 25 V and −8°C.

The perfectly arranged triangular lattice of nanopores is indicated in the SEM image as a net of black circles. The dimensions of pores and distances between neighboring pores are fully uniform. The 3D SEM image of the anodized surface
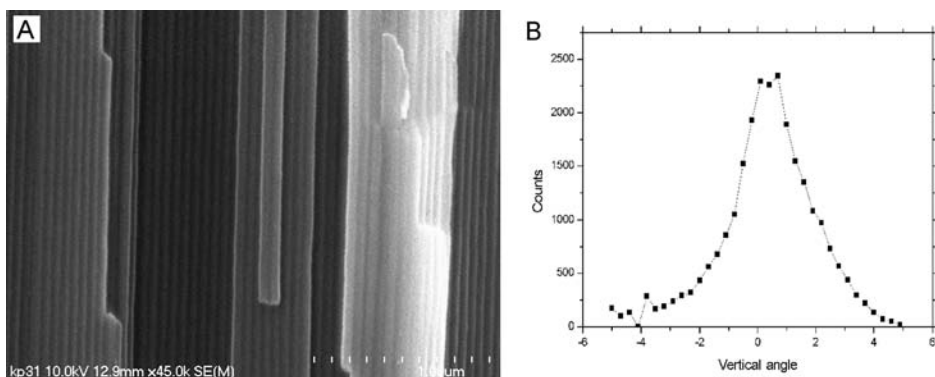
Figure 1.35 Cross-sectional view of anodic porous alumina formed at 21 V (A) and dissipation diagram recorded after transmission of the He$^+$ ion beam through the channels of AAO (B). The two-step anodization in the double-wall cell with magnetic stirrer was carried out in 2.4 M H$_2$SO$_4$ at 1 °C.

(Figure 1.36B) does not exhibit any defects in the arrangement of pores, while the high-degree of pore order is proved by the 2D FFT pattern (Figure 1.36C) consisting of six distinct spots.

It is widely recognized that the ideally ordered array of nanopores grown by self-organization processes can be observed only within perfectly ordered domains, over a surface area of about 0.5 to 5 μm^2 [236,403,493,498]. Defects in the hexagonal arrangement of nanopores appear at boundaries between ordered domains. Figure 1.37A shows the SEM top-view image of anodized aluminum taken from the surface area of 1 μm^2. The anodic porous alumina film was formed by two-step anodizing in 2.4 M H$_2$SO$_4$ under the constant potential of 25 V at −8 °C. A close-packed hexagonal arrangement of nanopores is still visible, but some defected pores have appeared that are not six-fold coordinated by neighboring pores. The 3D SEM image (Figure 1.37B) reveals clearly existing centers of defects as the protruding hills much higher than others. The order degree in the nanostructure was reduced slightly, and six distinct spots in the FFT image (Figure 1.37C) were broadened out.

The effect of anodizing temperature on the pore order degree of anodic porous alumina formed in sulfuric acid was studied at cell potentials between 15 and 25 V. A typical SEM top- view and 2D FFT images are shown in Figure 1.38A for a sample anodized at 23 V and 1 °C.

In order to better characterize the order degree of self-organized nanostructures, quantitative analyses of the FFT intensity profile were performed for various temperatures and anodizing potentials. Figure 1.38B presents the intensity profile taken from the FFT image along the direction marked with a solid line. From other two directions, marked in the FFT image, the intensity profiles were also taken and the regularity ratio, $H/W_{1/2}$ (defined as a ratio of the maximum intensity of the peak to the wide of the peak at half-maximum; Figure 1.38B), was calculated for various
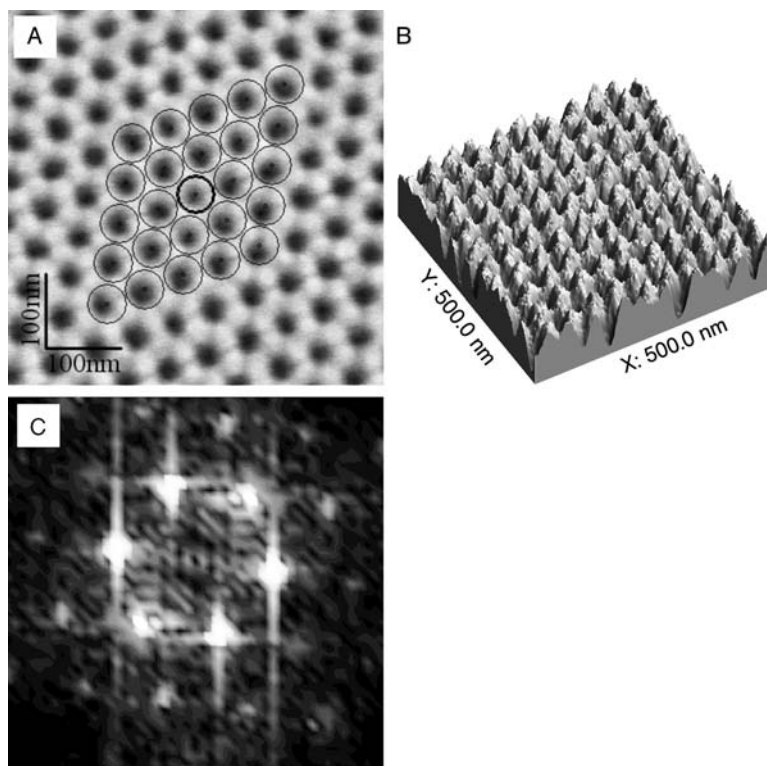
Figure 1.36 SEM top-view (A), 3D topography representation (B), and 2D FFT (C) image of a perfect triangular nanohole array. The porous alumina layer was formed at 25 V by two-step anodizing in 2.4 M H_2SO_4 at $-8\,°C$. The analyzed surface area was 0.25 μm^2. (Reprinted from Ref. [226].)

anodizing potentials and temperatures. The average regularity ratio versus anodizing potential is shown in Figure 1.39.

The results show that the hexagonal arrangement of nanopores obtained by two-step, self-organized anodization of aluminum in sulfuric acid can be considerably improved by increasing the anodizing potential. The average regularity ratio increases with anodizing potential such that a maximum is reached at 25 V, independently of the anodizing temperature. These results show that the formation of nanostructure with the best nanopore order occurs at the anodizing potential of 25 V.

The second method of quantitative analysis of pore arrangement in anodic porous alumina formed by self-organized anodization is based on a defect maps known as Delaunay's triangulations. Defects maps constructed from SEM top-view images for the arrangement of over 1000 pores formed in 2.4 M sulfuric acid at various potentials and temperatures are shown in Figure 1.40. Each pore that is not six-fold
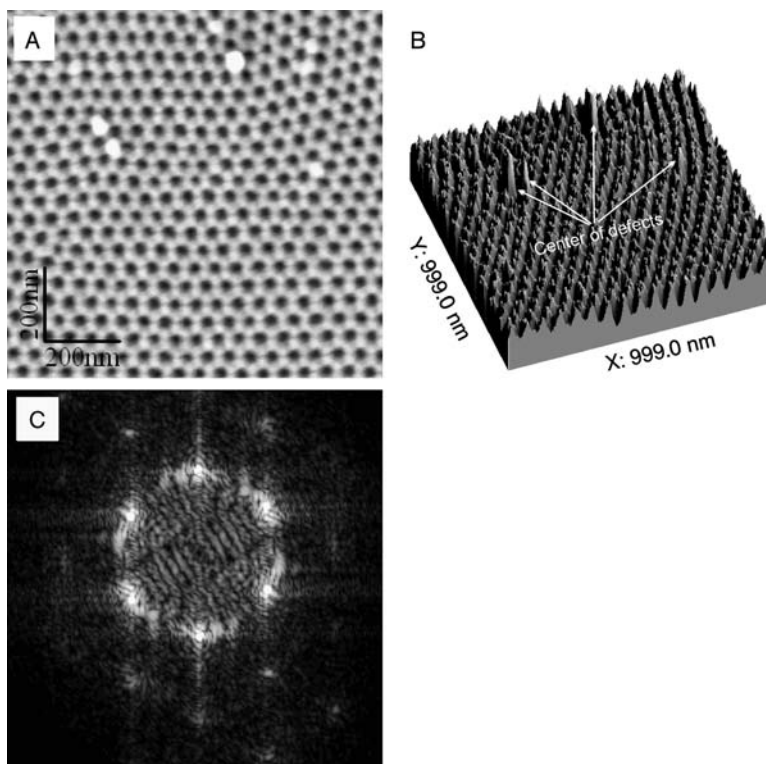
Figure 1.37 SEM top-view (A), 3D topography representation (B), and 2D FFT (C) image of anodic porous alumina with a regular nanohole array. The porous alumina layer was formed at 25 V by two-step anodizing in 2.4 M H_2SO_4 at $-8\,°C$. The analyzed surface area was $1\,\mu m^2$. (Reprinted from Ref. [226].)
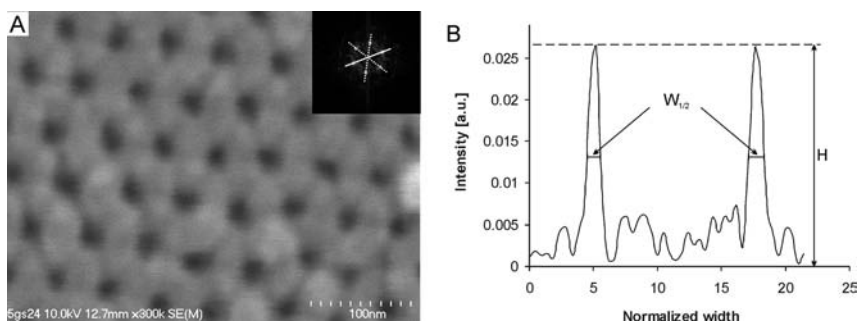
Figure 1.38 SEM top-view and FFT images of anodic porous alumina (A) and profile analysis of the FFT intensity along the marked solid line (B). The porous alumina layer was formed at 23 V by two-step anodizing in 2.4 M H_2SO_4 at $1\,°C$. (Reprinted with permission from Ref. [240], © 2007 Elsevier Ltd.).

Figure 1.39 Anodizing potential influence on the average regularity ratio ($H/W_{1/2}$) at various temperatures. (Reprinted with permission from Ref. [240], © 2007, Elsevier Ltd.).

Figure 1.40 Defect maps of the arrangement of over 1000 pores constructed from SEM images taken from a surface anodized at various cell potentials: 17 V (A), 21 V (B) and 25 V (C). The porous alumina layer was formed at 23 V by two-step anodizing in 2.4 M H_2SO_4 at 1 °C. (Reprinted with permission from Ref. [248], © 2006, Elsevier B.V.).
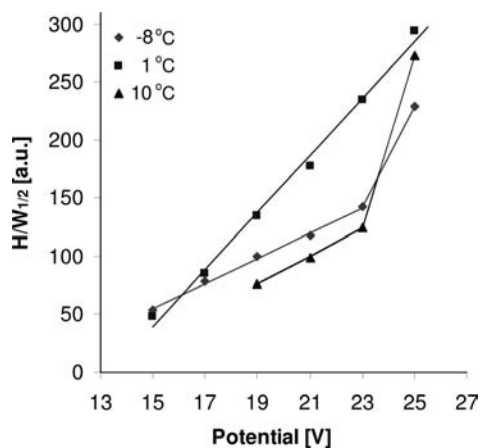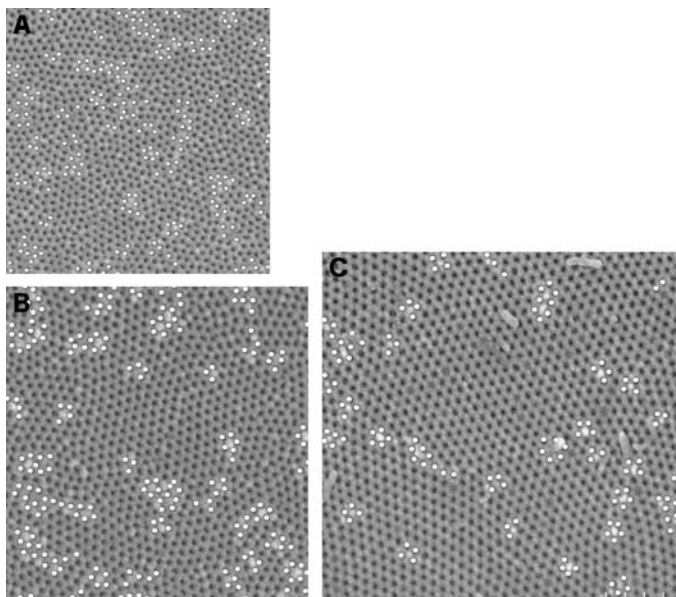
Table 1.20 Percentage of defects in the arrangement of nanopores at various temperatures.

Anodizing potential (V)	Surface area (μm)	−8 °C		1 °C		10 °C	
		Number of pores	Percentage of defects (%)	Number of pores	Percentage of defects (%)	Number of pores	Percentage of defects (%)
15	1.24×1.24	1230	30.81	1054	20.87	–	–
17	1.32×1.32	1046	29.70	1072	20.43	–	–
19	1.48×1.48	1077	30.18	1040	21.15	1100	30.73
21	1.57×1.57	1111	30.06	1004	20.92	1038	29.67
23	1.76×1.76	1193	30.60	1134	20.99	1249	30.50
25	1.76×1.88 or 1.82×1.82	1268	9.54	1137	11.70	1191	10.75

Reprinted from Ref. [226].

coordinated by neighboring pores is marked with a white dot. The percentage of defected pores was calculated and collected in Table 1.20.

For anodizing potentials from 15 to 23 V, the percentage of defected pores is constant, independent of the anodizing temperature. At a temperature of 1 °C, a 20% defect level is observed, while at −8 or 10 °C the percentage of defects increases to about 30%. A perfectly ordered anodic porous alumina with a number of defects equals to about 10% can be obtained by a self-organized anodizing of aluminum carried out at 25 V.

The analysis of nanostructure regularity and generated defects showed that the best nanostructure resulting in a highly ordered and uniform nanopore arrangement with a limited number of defects can be formed by a self-organized anodizing of aluminum conducted in sulfuric acid at 25 V and at 1 °C.

The effect of electrolyte concentration and anodizing time on the regularity of nanostructures formed by self-organized anodization of aluminum were also investigated for oxalic acid [241,385,495,496]. The regularity ratio analysis performed at various temperatures showed that the best nanopore arrangement with a largest size of ordered domains can be observed for the nanostructure formed under 40 V in 0.5 M oxalic acid and 5 °C [495], or in 0.3 M oxalic acid at 15–17 °C [241,496]. In contrast, Ba *et al.* [385] suggested that the best ordered anodic porous alumina could be formed by anodizing under 40 V in 0.6 M oxalic acid at 0 °C. The influence of anodizing time on the size of the ordered domains grown during the anodization of aluminum in 0.3 M oxalic acid at 40 V and 0 °C was studied [236,519]. It was found that the ordered domain size, equal to about 2.8 μm^2, could be obtained after 10 h of anodization, and the ordered domain area was doubled after 7 h of anodizing [519]. The linear relationship between the size of domain, D (μm^2), and time of anodization, t (h), was found to be at 0 °C:

$$[519] \quad D = 0.550 \cdot t \tag{52}$$

$$[236] \quad D = 0.195 \cdot t \tag{53}$$

and at 15 °C [236]:

$$D = 0.404 \cdot t \qquad (54)$$

The influence of temperature of aluminum annealing before anodization on the ordering degree of nanopores formed by two-step anodizing in 0.3 M oxalic acid was also investigated [520]. It was found that, with an increasing annealing temperature, the size of ordered domains increases gradually.

The structural uniformity of nanopore arrangement was studied from SEM images using adaptive thresholding with an analysis of wave propagation [521]. The percentage of hexagonality was calculated on the basis of Veronoi diagrams. The average hexagonality percentage for a commercially available membrane with a pore size of 20 nm (Anapore, Whatman) was found to range between 37.5 and 41.3%. However, for the laboratory-prepared membrane, synthesized by the self-organized one- or two-step anodizing in oxalic acid, the determined hexagonality ranged from 47.2 to 54.5%. The arrangement of nanopores formed by anodizing of aluminum was studied by Sui and Sangier using AFM [522]. The hexagonal array percentage over a surface area of $0.25 \, \mu m^2$ was found to be about 66% and 100% for anodizing in sulfuric and oxalic acids, respectively.

1.4.3
Post-Treatment of Anodic Porous Alumina

Recently, anodic porous alumina films with a regular arrangement of nanopores have been widely used as templates for the fabrication of other nanomaterials. Therefore, AAO films fabricated by self-organized anodization are usually subjected to an optional further post-treatment procedure which included removal of the aluminum base, removal or thinning of the barrier layer, and re-anodizing.

1.4.3.1 Removal of the Aluminum Base
In order to detach the aluminum oxide from the remaining aluminum base, an electrochemical detachment method employing a reversal and pulse voltage techniques can be used [502,503]. The separation of aluminum oxide from the remaining aluminum substrate might also be performed by using electrochemical etching in 20% HCl, with an operating potential between 1 and 5 V [302]. However, the most widespread method is based on a wet chemical removal of aluminum. For this procedure, the unoxidized aluminum substrate is usually dissolved by immersing an anodized sample for a few hours in a saturated $HgCl_2$ solution (e.g., Refs. [220,407,409]). Other solutions that are infrequently used for aluminum base removal are listed, together with operating conditions, in Table 1.21.

The effect of different $CuSO_4/HCl$ contents and solution temperature on the rate of chemical etching of aluminum substrate was investigated with great care [507]. Subsequently, it was found that the time necessary for effective dissolution of a

Table 1.21 Non-typical solutions used for the chemical removal of aluminum base after anodizing.

Solution	Temperature (°C)	Time (min)	Reference(s)
$Br_2 + CH_3OH$	40	10	[252,295]
$CuCl_2$ (saturated)	–	–	[523]
$CuCl_2$ (saturated) + 8% HCl	RT	–	[305,324]
0.08 M $CuCl_2$ + 8% HCl	20	60	[524]
0.1 M $CuCl_2$ + 20% HCl	5–RT	10	[253,299,491,501,515]
$CuSO_4$ (saturated)	–	–	[303]
$CuSO_4$ (saturated) + 38% HCl	0–20	2–5	[318,507]

RT: room temperature.

0.2 mm-thick aluminum base is less than 2 min within a range of HCl concentrations from 25% to 65%. The temperature of solution has a negligible influence on the time of removal. Indeed, following removal of the aluminum substrate, the spherical pore bottoms can be observed (see Figure 1.34B).

1.4.3.2 Removal of the Barrier Layer

The AAO template preparation consists of pore opening after separation of the oxide from the Al substrate, or pore widening before the subsequent deposition of metals and semiconductors into pores. Removal of the barrier layer in a separated AAO membrane, formed by self-organized anodization, is usually carried out by chemical etching of the oxide. The nanopore bottoms are opened by immersing in a H_3PO_4 solution, with the opening time depending directly on the barrier layer thickness, and consequently on anodizing conditions. Some selected procedures of barrier layer removal are listed in Table 1.22.

If the opening time is prolonged, the widening of pores can occur simultaneously [498]. The diameter of the opened pores can be adjusted by changing the time of the chemical etching treatment in a phosphoric acid solution. Pore opening and widening were studied in detail by Xu *et al.* [318]. Samples before widening treatment were anodized in 0.3 M $H_2C_2O_4$ at 40 V and 12 °C. The dissolution rate of the barrier layer in 0.5 M H_3PO_4 was found to be approximately 1.3 nm min^{-1}, and to decrease inside the columnar pore channel with increasing pore depth. The horizontal and vertical dissolution rates were also distinguished. The horizontal rate of oxide dissolution is mainly responsible for barrier layer removal, whereas the vertical rate plays a key role in the widening of pores and nanopore thickness reduction. A different etching technique using a reactive ion-beam (mainly Ar$^+$) was also proposed for removal of the barrier layer in anodic porous alumina [385,524,528]. Most importantly, it should be noted that dry etching by ion-beams requires the use of a sophisticated apparatus.

In order to obtained an array of ordered nanopores with a desired pore diameter, it is important first to carry out a widening treatment (Table 1.23).

Table 1.22 Selected procedures of pore opening after two-step anodizing of aluminum in sulfuric, oxalic and phosphoric acids.

	Anodization conditions			Opening conditions				
Electrolyte	Temperature (°C)	Potential (V)	Electrolyte	Temperature (°C)	Time (min)	D_P (nm)	Reference(s)
0.3 M H_2SO_4	10	25	0.5 M H_3PO_4	30	30	–	[403,493]
1.1 M H_2SO_4	5	25		30	23	33	[502]
0.2 M $H_2C_2O_4$	0	40		25	45	43	[506]
0.3 M $H_2C_2O_4$	0	60		RT	120	80	[501]
	1	40		35	30	–	[403,493]
	17	40		30	60	50	[500]
0.45 M $H_2C_2O_4$	5	40–50		30	75–85	40–72	[502]
1.1 M H_3PO_4	3	160		45	30	–	[403,493]
H_3PO_4-CH_3OH-H_2O (1:10:89, v/v)	−4	195	1.1 M H_3PO_4	20	300	350	[498,525,526]
H_3PO_4-C_2H_5OH-H_2O (1:20:79, v/v)	−10 to 0	195^a	0.5 M H_3PO_4	45	30	–	[339]

RT: room temperature.
^{a}Hard anodizing.

Table 1.23 Selected procedures of pore widening after a two-step anodizing of aluminum in sulfuric, oxalic and phosphoric acid solutions.

	Anodization conditions				Widening conditions			
Electrolyte	Temperature (°C)	Potential (V)	D_p (nm)	Electrolyte	Temperature (°C)	Time (min)	D_p (nm)	Reference(s)
1.1 M H_2SO_4	10	20	–	0.1 M H_3PO_4	35	20	–	[522]
6.0 M H_2SO_4	20	18	–	0.5 H_3PO_4	30	12	30	[494]
0.04 M $H_2C_2O_4$	5	85	90	0.5 H_3PO_4	20	30	120	[498,525,526]
0.2 M $H_2C_2O_4$	18	40	–	0.1 H_3PO_4	–	40	44	[505]
0.3 M $H_2C_2O_4$	–	40	31	0.1 H_3PO_4	30	30	46	[527]
						50	60	
	15	40	24	0.1 H_3PO_4	30	50	74	[241]
	15	40	–	0.1 H_3PO_4	35	50	52–60	[522]
	20	40	25	0.63 M H_3PO_4	20	85	75	[305]
	24	40	40	0.5 M H_3PO_4	25	60	80	[509]
0.63 M $H_2C_2O_4$	20	30	14.5	0.63 M $H_2C_2O_4$	40	30	20	[406]
						60	26	
						90	32	
						120	38	
0.3 M H_3PO_4	0	195	–	1.1 M H_3PO_4	–	240	320	[497]
0.45 M H_3PO_4	20–22	140	100	2.4 M H_2SO_4	20	60	103	[252]
						80	109	
						300	115	

A relationship between pore diameter (D_p, in nm) and widening time (t_w, in min) for samples anodized in 0.3 M oxalic acid under 40 V at 15 °C was reported by Hwang *et al.* [241]:

$$D_p = 24.703 - 0.116 \cdot t_w + 0.0221 \cdot t_w^2 \tag{55}$$

The widening of pores was conducted in 0.1 M H_3PO_4 at a temperature of 30 °C. In contrast, Choi *et al.* [529] suggested that the rate of pore widening in 1 M H_3PO_4 at 30 °C was equal to 1.83 nm min^{-1}. The diameter of the widened pores can easily be determined from SEM or AFM images [527]. Recently, capacitance–voltage measurements on thin alumina films have been proposed for characterization of the pore-widening process [530]. Pore widening in 1.2 M NaOH, leading to a simultaneous separation of AAO nanowires and nanotubes from the grown nanostructure, was also reported [523]. When ultrasonic waves were also used to assist the pore-widening process [531], the widening time was found to be shortened to a significant degree.

1.4.3.3 Structure and Thinning of the Barrier Layer

The structure of the barrier layer in anodic porous alumina, as well as its dielectric characterization modified by oxide dissolution or ion implantation, was studied using *in-situ* spectroscopic ellipsometry [532,533], Brillouin spectroscopy [534], electrochemical impedance spectroscopy (EIS) [448,533,535,536], and re-anodizing techniques [245–247,267,535,537,538].

It is generally accepted that the barrier layer in anodic porous alumina consists of two or three sublayers, each with a different susceptibility to chemical dissolution in acidic solution. Furthermore, the number and thicknesses of the sublayers, as well as the percentage share of the barrier layer thickness, depends on the anodizing potential. An anodic porous alumina was first formed under various anodizing potentials in 0.4 M H_3PO_4 and 0.45 M $H_2C_2O_4$ at 20 °C, and then subjected to dissolution by immersion in sulfuric acid [246,247,532,537,538]. The dissolution rate of the barrier layer in 2 M H_2SO_4 or H_3PO_4 at 50 °C was investigated using the re-anodizing technique (Figs. 1.41 and 1.42).
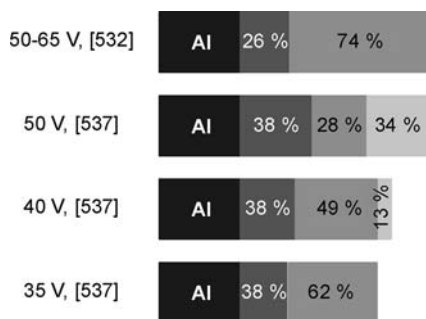

Figure 1.41 Sublayers of the barrier layer with different dissolution rates for anodic porous alumina formed by anodizing of aluminum in 0.4 M H_3PO_4 at 20 °C. (After Refs. [532,537].)
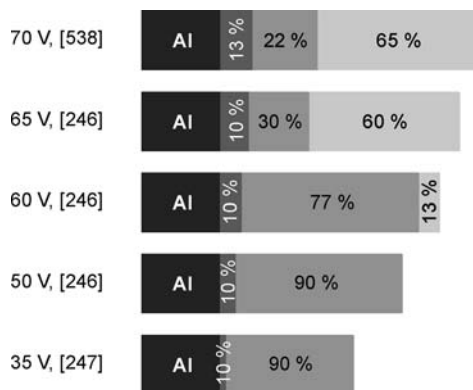
Figure 1.42 Sublayers of the barrier layer with different dissolution rates for anodic porous alumina formed by anodizing of aluminum in 0.44 M oxalic acid at 20 °C. (After Refs. [246,247,538].)

Dissolution of the barrier layer formed in a 0.1 M ammonium adipate solution at the anodizing potential between 5 and 80 V and 20 °C was studied using the re-anodizing technique [267]. The rate of dissolution was investigated in 2 M sulfuric acid at 60 °C, whereupon the results obtained suggested the dissolution rate to be similar for anodic films formed at the anodizing potential between 20 and 80 V. Although the barrier layer was seen to be composed of one layer, for lower anodizing potentials two sublayers were apparent, each with different dissolution rates.

A close control of the nucleation sequence of electrodeposits within all pores of the anodic porous alumina is required in order to create a significant thinning of the barrier layer. Such effective thinning provides the necessary conditions for electrons to tunnel through the barrier layer, with subsequent uniform pore filling by electrodeposition. Thinning of the barrier layer in anodized aluminum always occurs together with pore widening. According to Stein *et al.* [532], the barrier layer in anodic porous alumina formed in 0.4 M H_3PO_4 under the constant current density of 2 mA cm^{-2} at 20 °C consists of two sublayers each with a different dissolution rate (see Figure 1.41). The interface barrier layer, which is close to the metal/oxide interface, does not dissolved in 2 M H_3PO_4, whereas the layer at the pore bottoms is in contact with the electrolyte and dissolves easily. The rate of barrier layer dissolution in a mixture of 0.4 M phosphoric and 0.2 M chromic acids at various temperatures was investigated in detail [533]. The barrier layer in the anodic porous alumina film was formed by anodization in 0.34 M oxalic acid under 30 V at 0 °C. Subsequently, the dissolution rate of the 36 nm-thick barrier layer was estimated as approximately 0.3 and 1.0 nm min^{-1} at temperatures of 38 and 60 °C, respectively. Under the same anodizing conditions, the dissolution rate of porous oxide formed by anodization was estimated at 6 nm min^{-1} for 38 °C.

O'Sullivan and Wood [208,232] suggested that decreasing the anodizing potential would result in a substantial barrier layer thinning, due to a field-assisted dissolution

of the oxide. On the basis of this assumption, an extraordinary electrochemical method of homogeneous thinning of the barrier layer was derived [539]. A progressive reduction of the anodizing potential led to a thinning of the barrier layer, and finally to its perforation. The step-wise reduction of the anodizing potential from 160 to 0.1 V, with decrements of 0.3 V or 5% of the existing potential, was applied to thin the barrier layer formed by the anodization g of aluminum in 0.4 M H$_3$PO$_4$ at 25 °C [539]. A similar, exponentially decaying, potential was applied for thinning of the barrier layer in anodic porous alumina formed in 0.1 M phosphoric acid at 195 V [529]. The process of thinning involves two different electrolytes used for the different ranges of decaying potential. For the thinning process from 195 to 80 V, 0.1 M phosphoric acid was used, and each potential decrement of 2 V was applied for 180 s. In the range of decaying potential from 80 to 1 V, a 0.3 M oxalic acid solution was used for barrier layer thinning. The exponential step-wise reduction began from a step of 2 V and finished at the last step with the potential difference of 0.01 V. Each step of the potential reduction was applied for 30 s. This thinning method was successfully applied during fabrication of the ordered Ni nanowire array by electrodeposition of metal into nanopores of the AAO template. The thinning of the barrier layer in AAO formed in 0.3 M oxalic acid at 40 V and 2 °C was performed by means of two subsequent additional anodizations conducted for 15 min under constant current densities of 290 and 135 mA cm^{-2}, respectively [540]. Prior to the electrochemical barrier layer thinning, a chemical widening of the pores in 0.3 M oxalic acid was carried out for 2 h at 30 °C.

1.4.3.4 Re-Anodization of Anodic Porous Alumina

The re-anodizing technique, which is known also as a pore-filling method, is widely used to characterize porous oxide films formed by anodization. The re-anodization of anodic alumina is usually carried out under the constant current density in a neutral electrolyte, for example a mixture of 0.5 M H$_3$BO$_3$ + 0.05 M Na$_2$B$_4$O$_7$ [245–247,406,537,538]. The dissolution rate of the barrier layer in acidic solutions, as well as the anodizing potential influence on the thickness of the barrier layer formed during anodization in ammonium adipate [267], oxalic [246,247,406,538] and phosphoric acid [245,537] solutions, were investigated using the re-anodization technique. The re-anodizing method allows one to calculate the anodic oxide thickness from Eq. (42). Girginov *et al.* [533] showed EIS to be a suitable technique for the estimation of barrier layer thickness modified by re-anodization. Moreover, the electrical conductivity of the complex anodic oxide films formed during re-anodizing of anodic porous alumina was investigated in detail [541]. The modification of barrier layer properties by the re-anodization of anodic porous alumina in oxalic acid with fluoride additives was also studied [536], with a significant reduction in electrical resistance being observed during the re-anodizing.

The re-anodizing methods can be used for determination of anodic alumina porosity, α, from the following equation:

$$\alpha = \frac{T_{Al^{3+}}\cdot(m_2/m_1)}{1-(1-T_{Al^{3+}})(m_2/m_1)} = \frac{T_{Al^{3+}}\cdot(m_2/m_1)}{1-T_{O^{2-}}\cdot(m_2/m_1)} \tag{56}$$

where: $T_{Al^{3+}}$ and $T_{O^{2-}}$ are transport numbers of Al^{3+} and O^{2-}, m_1 is the slope of the voltage–time curve recorded during re-anodizing, and m_2 is the slope of the voltage–time curve recorded during the anodizing of aluminum. Since the transport numbers of Al^{3+} and O^{2-} were estimated at 0.4 and 0.6 for various electrolytes used for anodizing, the porosity of anodic porous alumina can easily be calculated. The re-anodization was also successfully employed for determination of the porosity of anodic porous alumina films formed in sulfuric [216,249], oxalic [216,249,406,541], phosphoric [216,249,336], and chromic acids [249].

The kinetics of growth of the complex anodic alumina films during re-anodization was studied by Girginov *et al.* [542–545]. These authors found that, during re-anodization, the current flowed mainly through the bottom of pores, with distributions of the current density at the pore bottoms corresponding directly to the hemispherical curvature of the pore bottom.

1.5
AAO Template-Assisted Fabrication of Nanostructures

The self-organized anodization of aluminum, which results in a hexagonal pattern of nanopores with an extended long-range perfect order, appears to be a very promising powerful and inexpensive method used for the synthesis of nanostructured materials. AAO templates are widely used for the transfer of nanopore arrangements to other materials. In general, the use of anodic porous alumina for nanomaterials fabrication can be carried out in two ways: (i) the anodic film with a remaining aluminum substrate can be used directly for the electrodeposition of metals; or (ii) it can be separated from the aluminum base and further processed into a freestanding membrane with open pores at the top and bottom of the membrane. The second approach to employing a freestanding AAO template represents a key method for fabricating highly ordered nanostructures. Liang *et al.* [546] have reported details of the most widespread methods of nanoarrays fabrication employing anodic porous alumina (Figure 1.43).

An enormous variety of nanoscale materials including metal and semiconductors nanopores, rings, particles, nanorods and nanowires, metal oxides, metallic, Si and diamond nanopore arrays, carbon and polymer nanotubes have been successfully fabricated on a basis of ordered anodic porous alumina. However, unfortunately only selected nanostructured materials fabricated on the basis of the AAO template can be discussed here.

Most nanomaterials synthesized with the assistance of anodic porous alumina may be classified into the following groups:

- Metal nanodots, nanowires, nanorods and nanotubes
- Metal oxide nanodots, nanowires and nanotubes
- Semiconductor nanodots, nanowires, nanopillars and nanopore arrays
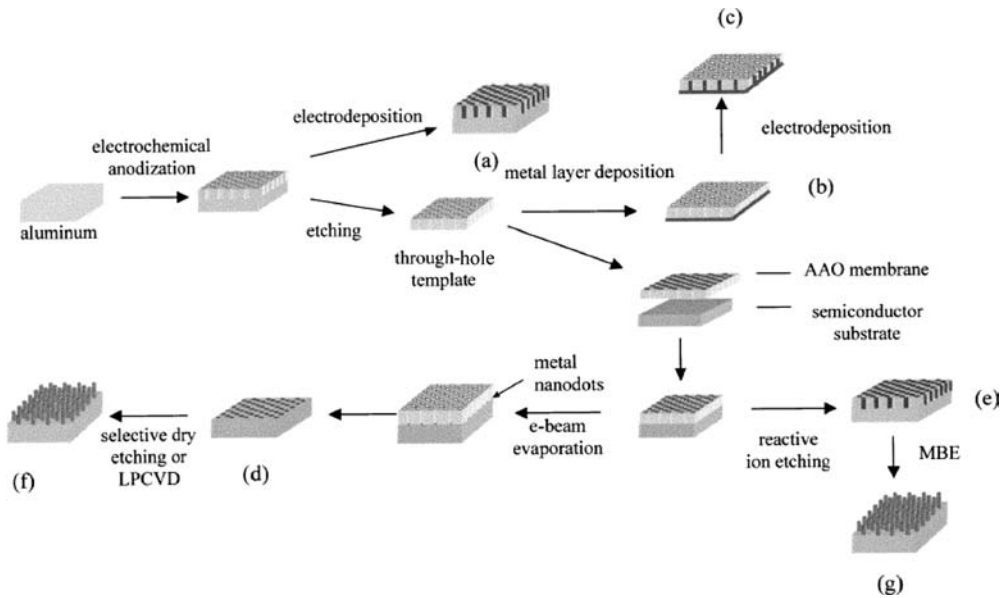- Polymer, organic and inorganic nanowires and nanotubes
- Carbon nanotubes

Figure 1.43 Schematic diagram of the fabrication of nanostructured materials with utilization of anodic porous alumina. Step a: metallic nanowire array electrodeposited in AAO; step b: AAO template with metal deposited on its surface; step c: metal nanowire array electrodeposited within the AAO template; step d: metallic nanodot array deposited on semiconductor substrate; step e: semiconductor substrate with nanopore array; step f: semiconductor freestanding nanopillar array; step g: heterostructure quantum dot array by molecular beam epitaxy (MBE). (Reprinted with permission from Ref. [546], © 2002, Institute of Electrical and Electronics Engineers, Inc.).

- Photonic crystals
- Other nanomaterials (metallic and diamond membranes, biomaterial, etc.).

1.5.1
Metal Nanodots, Nanowires, Nanorods, and Nanotubes

Metallic nanodot arrays are often fabricated by the evaporation of metals into the AAO template (step d in Figure 1.43). The advantage of the evaporation method over electrochemical deposition is an easier control of nanodot growth. Various nanodot arrays were obtained including Ni [4], Cu [547] Au and Au–Ag [548] nanodots on a Si substrate. Recently, Park *et al.* [549] reported Au, Al, Ag, Pb, Cu, Sn and Zn nanodot arrays on the silicon substrate obtained by metal evaporation through the AAO template. A second approach to nanodot or nanoparticle synthesis is a metal deposition via a chemical route. For example, Ag [550] and Pd [551] nanodots were fabricated successfully using the chemical method.

Arrays of metallic nanowires and nanorods are mainly synthesized by the electrodeposition of materials into the nanochannels of anodic porous alumina (step a in
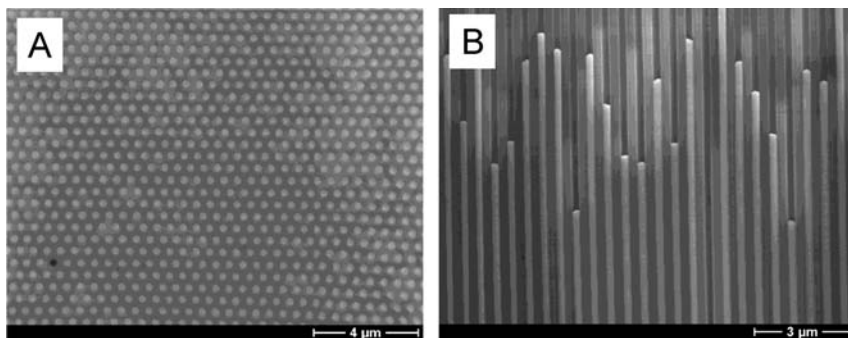
Figure 1.44 SEM images of silver wires embedded in a mono-domain anodic porous alumina template. Top view (A) and cross-sectional view (B). (Reprinted in part with permission from Ref. [529], © 2004, American Chemical Society.)

Figure 1.43) or in the AAO template with open pores (steps b and c in Figure 1.43). Arrays of Ag [529,552,553], Au [554–556], Co [557–559], Cu [560], Ni [540,556,561–566], Pb [567], and Pd [568] nanowires and nanorods were obtained successfully by electrodeposition. A highly ordered array of silver nanowires electrodeposited in the AAO template is presented in Figure 1.44.

A single Ni nanowire and complex nanowire pattern were also obtained by electrodeposition with a supported AAO template [569]. Recently, the electrochemical deposition of multilayered Co/Cu [570] and alloyed Co–Cr [571], Co–Pt [572,573], Fe–Pt [573] and Fe–Pd [574] nanowires into anodic porous alumina was also reported, while the evaporation technique was used to fabricate arrays of Au nanowires [575]. Ag [576] and Ni doped with P [577] nanowires were obtained by the electroless deposition of metals into the AAO template.

Metallic nanotubes with outer diameters ranging from 50 to 100 nm were successfully prepared by the electrodeposition of Fe, Co and Ni inside nanopores of the through-hole AAO template (steps b and c in Figure 1.43) [578]. The immobilization of Ag nanoparticles, followed by the electrochemical deposition of Au and Ni, was applied for the synthesis of Au and multi-segmented Au–Ni nanotubes [579]. Thin-walled Co [510,580] or Pd [581–583] nanotubes coated with a polymer layer on their inner walls were formed in anodic porous alumina. These composite magnetic nanotubes were obtained within the AAO template by thermal decomposition of the appropriate precursor; the same process was also used to synthesize Au nanotubes inside the AAO template [584]. The spontaneous coalescence of Au nanoparticles on the pore walls of a silane-treated AAO template was used for the fabrication of Au nanotubes [585]. The electroless deposition as a method of Co, Ni and Cu nanotube synthesis was reported by Wang *et al.* [586]. Aluminum nanotubes were formed by physical vapor deposition on the AAO template, followed by atmospheric pressure injection of the evaporated layer into pores of the template [587].

Metal Oxide Nanodots, Nanowires, and Nanotubes

By using the AAO template, metal oxide nanodots and nanowires are usually formed in nanopores of the template by electrochemical or electroless deposition of metals (steps a–c in Figure 1.43), followed by their oxidation. This method was employed successfully for the fabrication of ZnO nanowires [588]. The electrodeposition technique was used for a direct deposition of Cu_2O nanowires into the channels of porous alumina template [589]. Metal evaporation through the AAO template with open pores (step d in Figure 1.43) was used for the preparation of TiO_2 nanodots [546]. Recently, the complex structure of In_2O_3 rods in dots was synthesized by the deposition of individual nanorods within the AAO template on a Si substrate using a radiofrequency magnetron sputtering system [590]. A highly ordered array of tantalum oxide nanodots with a narrow size distribution was fabricated by the anodization of Al on TaN [591] and Ta(Nb) [592] substrates. During anodizing, the aluminum layer is converted into porous alumina oxide, and the growth of tantalum oxide beneath the anodic porous alumina occurs simultaneously. Alternatively, ZnO nanowires can be formed by a catalyzed epitaxial crystal growth [593], and the AAO template was used to form ordered Au dots on GaN. The regular array of straight ZnO nanowires was grown on Au nucleation sites. TiO_2 [594] and WO_3 [595] porous films were fabricated using a two-step replication process. The first step of the method was based on the fabrication of negative-type AAO with poly(methacrylate) (PMMA). In the second step, the replicated PMMA-negative with the evaporated thin Au layer was used either for the subsequent electrodeposition of WO_3 [595] or for a sol–gel synthesis of TiO_2 [594]. Sander *et al.* [596] used atomic layer deposition (ALD) to create an array of ordered TiO_2 nanotubes inside the channels of anodic porous alumina template (Figure 1.45). Recently, ferroelectric $PbZrTiO_3$ nanotube arrays were also fabricated by using a sol–gel method of the AAO template infiltration [597].

Semiconductor Nanodots, Nanowires, Nanopillars, and Nanopore Arrays

Recently, research interest has focused on the synthesis of semiconductor nanostructures, due mainly to their fascinating potential technological applications. The hexagonal pattern of the AAO template can be replicated directly in semiconductors by using dry etching methods, such as plasma etching, ion milling, and reactive ion etching. This positive transfer of the nanopore arrangement (step e in Figure 1.43) results in antidot (pore) arrays in the semiconductor material. Alternatively, the negative transfer of AAO nanopores, employing molecular beam epitaxy (MBE) and metal–organic chemical vapor deposition (MOCVD) (steps e and g in Figure 1.43) or vapor–liquid–solid (VLS) growth and low-pressure chemical vapor deposition (LPCVD) (steps d and f in Figure 1.43), produces quantum dots or nanopillars. Quantum dot arrays can also be fabricated by the extended anodization of aluminum on a semiconductor substrate [598]. The process is continued until the moment when a whole aluminum layer is consumed, after which a barrier layer of anodic
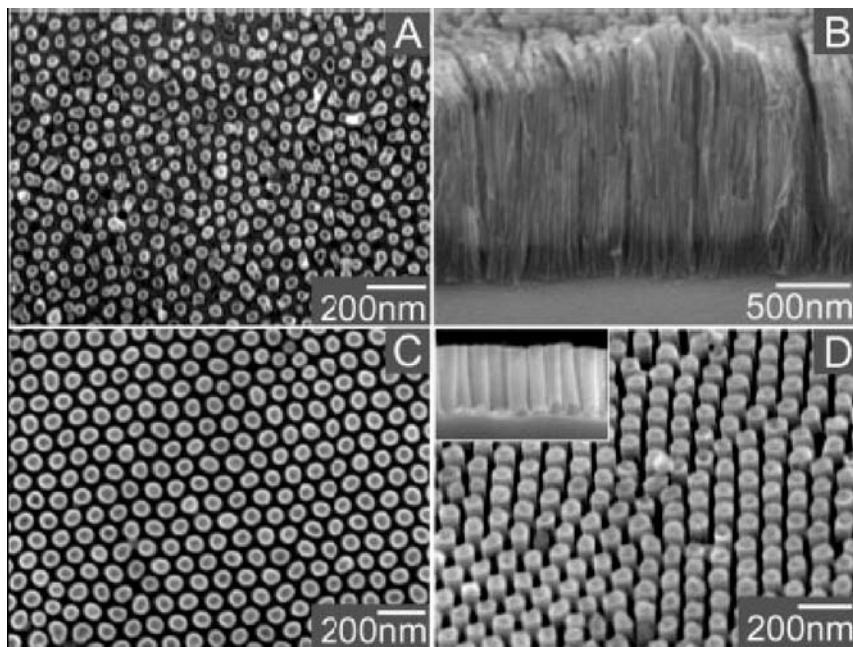
Figure 1.45 SEM images of TiO$_2$ nanotube arrays on silicon substrate. Top view (A) and side view (B) of nanotubes with outer diameters of 40 nm and average intertube spacing of 60 nm. Top (C) and oblique (D) of hexagonally ordered array of nanotubes with outer dia-meters of 80 nm and average intertube spacing of 100 nm. The inset in (D) shows a side view of the nanotubes on the substrate. (Reprinted with permission from Ref. [596], © 2004, Wiley-VCH Verlag GmbH & Co. KGaA.)

porous alumina is dissolved and oxidation of the semiconductor substrate occurs. The great variety of quantum dot arrays, including InAs [598], GaN [599], CdTe [600,601], InGaN [602], SiO$_2$ [603] and nc-Si:H [604] dots on various semiconductor substrates (Si, GaAs or GaN), were fabricated with AAO template assistance. Wang *et al.* [602] reported that a strict control of the growth time can result in nanorings and nanoarrows of regular patterns formed by MOCVD (Figure 1.46).

Anodic porous alumina is widely used as a template for the synthesis of semi-conductor nanowires and nanopillars. Si, InP, GaAs and GaN nanopillars were fabricated using the reactive ion or reactive beam etching process (step e in Figure 1.43) [546,605,606]. Uniformity of the pore diameter in GaAs and InP nano-hole arrays was fairy acceptable for 2D photonic bandgap crystals. The hexagonally arranged nanowire array of GaN grown in the VLS process (step f in Figure 1.43) was also reported [4]. The AAO template-assisted electrochemical deposition was used for the preparation of PbS [607], CdS [608–610] and Se [611] nanowires. Semicon-ductor InN nanowires were fabricated by the electrodeposition of indium into pores of anodic porous alumina, followed by a direct reaction of indium with ammonia at 550–700 °C [612]. The hydrothermal method with the AAO membrane was used for the synthesis of In$_2$S$_3$ nanofibers [613].
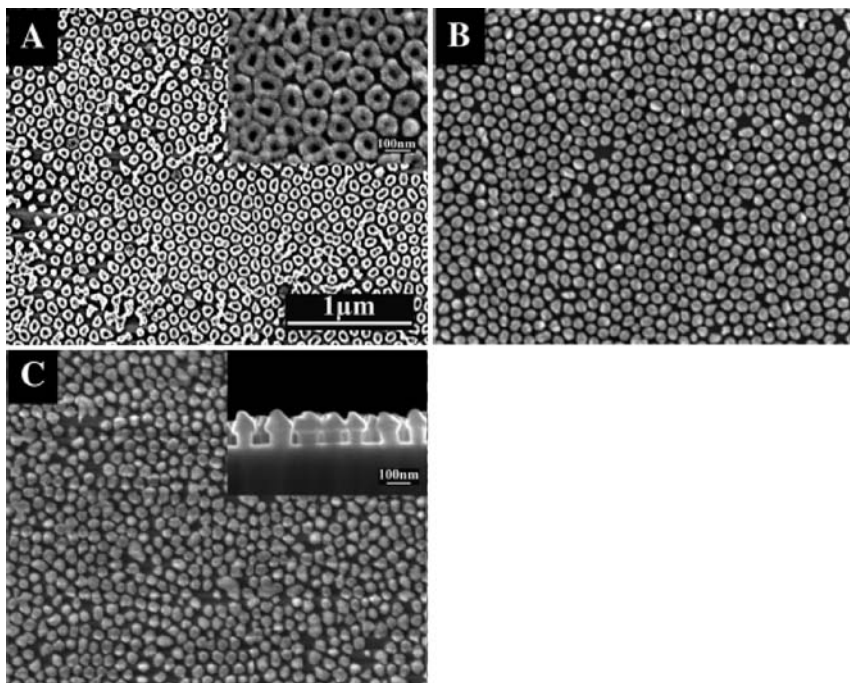
Figure 1.46 SEM images of InGaN nanostructures. Nanorings (A) (inset shows the larger magnitude); nanodots (B); and nanoarrows (C) (inset shows the cross-sectional view). (Reprinted with permission from Ref. [602], © 2006, American Chemical Society.)

1.5.4
Polymer, Organic and Inorganic Nanowires and Nanotubes

Ordered porous alumina membranes are considered to be one of the most suitable host materials for the fabrication of polymer nanowires and nanotubes. High-conductivity polypyrrole (PPy) nanowires with a pore diameter of 220 nm and length of 20 μm were prepared by using anodic porous alumina as the template (Figure 1.47). The high-density array of uniform nanowires was electrosynthesized in a medium of 75% isopropyl alcohol + 20% boron trifluoride diethyl etherate + 5% poly(ethylene glycol) [614].

A melt-assisted template method employing anodic porous alumina was used for the synthesis of semi-conducting polythiophene mesowires [615]. The AAO template was also used for the fabrication of organic–inorganic hybrid polymer nanowires consisting of poly(N-vinylcarvazole), rhodamine 6G and TiO_2 nanoparticles [616]. A wide variety of polymer nanotubes, such as perylene [617], polyaniline [618], polystyrene [582,619], polytetrafluoroethylene (PTFE) [619,583], polyvinylidene fluoride (PVDF) [582,583], and epoxy resin [620] were successfully prepared by a simple wetting of the AAO templates. Poly(p-xylene) (PPX) nanowires were synthesized by CVD polymerization [621] and poly(2-hydroxyethyl methacrylate) (PHEMA) by atom
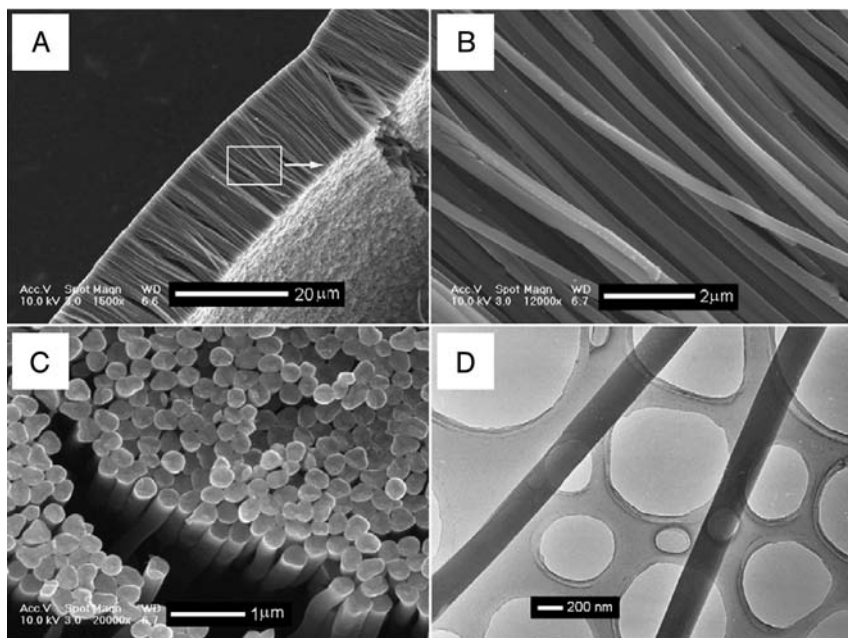
Figure 1.47 SEM images (A)–(C) and TEM image (D) of the PPy nanowires. (Reprinted with permission from Ref. [614], © 2006, IOP Publishing Ltd.).

transfer radical polymerization [622], with the assistance of AAO templates. The highly ordered array of PMMA nanopores, fabricated on the basis of the AAO template [594,595,623,624] is frequently used for the fabrication of various nanoporous membranes by the two-step replication process.

Recently, the preparation of crystalline organic nanorods of 2,7-di-*t*-butylpyrene (DTBP) [625] and organometallic nanotubes synthesized from a di-Rh N-heterocyclic carbene complex [626] were also reported.

By using highly ordered anodic porous alumina as templates, inorganic nanowires such as AgI [627], CuS, Ag_2S, CuSe and Ag_2Se [628] were prepared successfully by the electrochemical or electroless deposition processes. A high aspect ratio Prussian blue nanotube [629] with an outer diameter of 60 nm, and nickel sulfide [630] nanotubes with a diameter of approximately 200 nm, were each grown inside the pores of the AAO template.

1.5.5
Carbon Nanotubes

In recent years, carbon nanotubes have attracted much attention due to their remarkable electronic, optical, and mechanical properties. AAO templates have often been utilized for carbon nanotube growth [621,631–638], while cylindrical carbon nanotubes with various diameters [631–637] and triangular [638] cross-sections have been

synthesized using the CVD approach. An array of parallel and multiwalled carbon nanotubes with uniform diameter and periodic arrangement was achieved by using the AAO template [4,634,635]. The production of carbon nanotubes with deposited Pt nanoparticles on the interior walls of the AAO template has also been reported [637].

1.5.6
Photonic Crystals

Two-dimensional photonic crystals are periodic dielectric materials with an ability to control the propagation of light. The ideally ordered array of nanopores in anodic porous alumina can be directly used as a 2D photonic crystal in the near-infrared (IR) and visible wavelength regions. Numerous publications have been dedicated to 2D photonic band-gap crystals made from ideally ordered anodic porous alumina [639–646]. A monodomain porous alumina with a perfect nanopore order and high aspect ratio, for photonic crystals applications, is normally fabricated by anodizing of the pre-patterned aluminum foil.

1.5.7
Other Nanomaterials (Metallic and Diamond Membranes, Biomaterials)

The growing interest in nanoimprinting and the development of regular patterns has resulted in a considerable increase in the number of attempts to transfer the perfect order of nanopores from the AAO template to other materials with a greater mechanical stability. A variety of nanomaterials with a highly ordered arrangement of nanopores has been fabricated with aid from the AAO template, including a negative array of highly ordered Ni nanorods [647], and negative membranes from Ni [648], Au [593,649,650], Pt [651] and diamond [652,653]. A freestanding gold nanotube membrane replicated by Fan *et al.* [593] from a monodomain AAO template is illustrated in Figure 1.48.
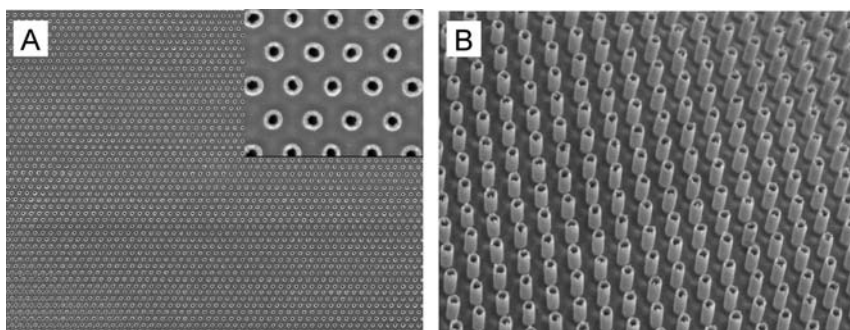

Figure 1.48 (A) SEM image of a gold nanotube membrane viewed from the front side (inset: enlarged top view). The inner diameter of the nanotube is about 130 nm. (B) Inclined view of the gold nanotube membrane showing the perfect alignment of the nanotubes. (Reprinted with permission from Ref. [593], © 2005, IOP Publishing Ltd.).

Recently, a number of nanostructured biomaterials have been synthesized on the base of the AAO template [622,654–657]. Protein binding to an AAO membrane covered with a polymer layer and functionalized by a nitrotriacetate–Cu^{2+} complex was studied [622]. Such modified membranes reveal an unusually high capacity for rapid protein binding, and can be applied to the purification of His-tag proteins. A flow-through-type DNA array, prepared by affixing a single-stranded probe DNA to the sidewall of holes in the perfectly ordered anodic porous alumina film with the evaporated Pt layer, was recently described [654]. The formation of a highly ordered DNA array on the Au array formed in anodic porous alumina was also studied [655,656]. Controlled DNA nanopatterning was carried out via the fabrication of Au disk arrays on the AAO template, with a interpore distance of 63 nm and a pore diameter of 40 nm. DNA molecules were fixed to the ordered Au disc array by the formation of Au−S bonds between the Au surface and thiolated groups introduced at the end of the DNA sequences. The DNA nanopatterns (Figure 1.49) were formed upon immersion of the Au disk array into DNA solution [656].

The potential applications of such materials lie in the field of highly functional biodevices for analysis in hereditary diseases, in DNA computers, molecular motors, heterogeneous sensors, transducers, and reactors. An electrochemical biosensor for the determination of blood glucose was constructed by the condensation polymerization of dimethyldichlorosilane at the surface of a porous alumina membrane [658]. Anodic porous alumina films can also be used as implants with enhanced bone-bonding performance, by filling the nanopores with a bioactive material that supports normal osteoblastic activity [659].
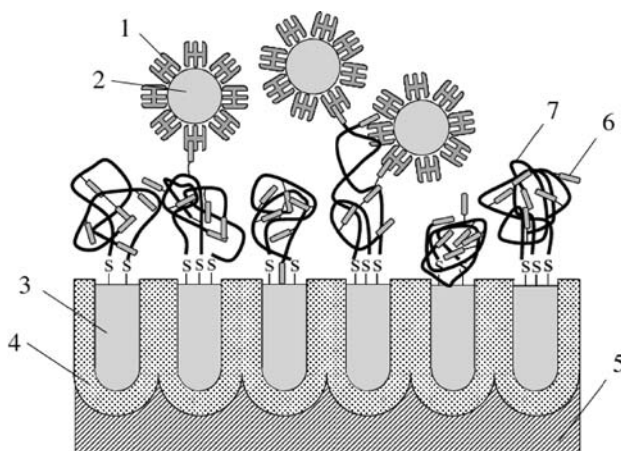

Figure 1.49 Schematic of Au-particle-DNA array prepared using Au disk array formed from highly ordered anodic porous alumina. (1) Streptavidin; (2) Au particles; (3) deposited Au; (4) anodic porous alumina; (5) aluminum; (6) biotin; (7) DNA. (Reprinted with permission from Ref. [656], © 2005, The Japan Society of Applied Physics.)

Acknowledgments

References

1 Parades, J.I., Martínez-Alonso, A. and Tascón, J.M.D. (2003) *Micropor. Mesopor. Mater.*, **65**, 93–126.

2 Rosei, F. (2004) *J. Phys. Condens. Matter*, **16**, S1373–S1436.

3 DiNardo, N.J. (1994) in *Materials Science and Technology*, (eds R.W. Cahn, P. Haasen and E.J. Kramer), Vol. 2B, *Characterization of Materials, Part II*, E. Lifshin (Vol. Ed.), VCH Verlagsgesellschaft mbH, Weinheim, Germany, pp. 2–158.

4 Chik, H. and Xu, J.M. (2004) *Mater. Sci. Eng. R*, **43**, 103–138.

5 Noda, S. (2001) *MRS Bull.*, August, 618–620.

6 Polman, A., Wiltzius, P. and Editors, G. (2001) *MRS Bull.*, August, 608–610.

7 Kamp, M., Happ, T., Mahnkopf, S., Duan, G., Anand, S. and Forchel, A. (2004) *Physica E*, **21**, 802–808.

8 Matthias, S., Müller, F., Jamois, C., Wehrspohn, R.B. and Gösele, U. (2004) *Adv. Mater.*, **16**, 2166–2170.

9 Létant, S.E., van Buuren, T.W. and Terminello, L.J. (2004) *Nano Lett.*, **4**, 1705–1707.

10 Cui, Y., Wei, Q., Park, H. and Lieber, C.M. (2001) *Science*, **293**, 1289–1292.

11 Vaseashta, A. and Dimova-Malinovska, D. (2005) *Sci. Technol. Adv. Mater.*, **6**, 312–318.

12 Alexson, D., Chen, H., Cho, M., Dutta, M., Li, Y., Shi, P., Raichura, A., Ramadurai, D., Parikh, S., Stroscio, M.A. and Vasudev, M. (2005) *J. Phys.: Condens. Matter*, **17**, R637–R656.

13 Petroff, P.M., Lorke, A. and Imamoglu, A. (2001) *Physics Today*, May, 46–52.

14 Hazani, M., Hennrich, F., Kappes, M., Naaman, R., Peled, D., Sidorov, V. and Shvarts, D. (2004) *Chem. Phys. Lett.*, **391**, 389–392.

15 Pedano, M.L. and Rivas, G.A. (2004) *Electrochem. Commun.*, **6**, 10–16.

16 Gooding, J.J. (2005) *Electrochim. Acta*, **50**, 3049–3060.

17 Ben-Ali, S., Cook, D.A., Evans, S.A.G., Thienpont, A., Bartlett, P.N. and Kuhn, A. (2003) *Electrochem. Commun.*, **5**, 747–751.

18 Ben-Ali, S., Cook, D.A., Bartlett, P.N. and Kuhn, A. (2005) *J. Electroanal. Chem.*, **579**, 181–187.

19 Mai, L.H., Hoa, P.T.M., Binh, N.T., Ha, N.T.T. and An, D.K. (2000) *Sensors Actuators B*, **66**, 63–65.

20 Islam, T., Mistry, K.K., Sengupta, K. and Saha, H. (2004) *Sensors Mater.*, **16**, 345–356.

21 Fert, A. and Piraux, L. (1999) *J. Magn. Magn. Mater.*, **200**, 338–358.

22 Oepen, H.P. and Kirschner, J. (1999) *Curr. Opin. Solid State Mater. Sci.*, **4**, 217–221.

23 Ross, C.A. (2001) *Annu. Rev. Mater. Res.*, **31**, 203–235.

24 Aranda, P. and García, J.M. (2002) *J. Magn. Magn. Mater.*, **249**, 214–219.

25 Hasegawa, R. (2002) *J. Magn. Magn. Mater.*, **249**, 346–350.

26 Juang, J-Y. and Bogy, D.B. (2005) *Microsyst. Technol.*, **11**, 950–957.

27 Chou, S.Y. (1997) *Proceed. IEEE*, **85**, 652–671.

28 Guo, L., Leobandung, E. and Chou, S.Y. (1997) *Science*, **275**, 649–651.

29 Oh, S-W., Rhee, H.W., Lee, Ch., Kim, Y. Ch., Kim, J.K. and Yu, J-W. (2005) *Curr. Appl. Phys.*, **5**, 55–58.

30 Walter, E.C., Favier, F. and Penner, R.M. (2002) *Anal. Chem.*, **74**, 1546–1553.

31 Yun, M., Myung, N.V., Vasquez, R.P., Lee, Ch., Menke, E. and Penner, R.M. (2004) *Nano Lett.*, **4**, 419–422.

32 Routkevitch, D., Tager, A.A., Haruyama, J., Almawlawi, D., Moskovits, M. and Xu, J.M. (1996) *IEEE Trans. Electron Devices*, **43**, 1646–1658.

33 Samuelson, L. (2003) *Materials Today*, October, 22–31.

34 Forshaw, M., Stadler, R., Crawley, D. and Nikolić, K. (2004) *Nanotechnology*, **15**, S220–S223.

35 Dreselhaus, M.S., Lin, Y.M., Rabin, O., Jorio, A., Souza Filho, A.G., Pimenta, M. A., Saito, R., Samsonidze, Ge.G. and Dresselhaus, G. (2003) *Mater. Sci. Eng. C*, **23**, 129–140.

36 Dresselhaus, M.S., Lin, Y.M., Rabin, O., Black, M.R. and Dresselhaus, G. (2004) in *Springer Handbook of Nanotechnology*, (ed. B. Bhushan), Springer-Verlag, Heidelberg, Germany, pp. 99–145.

37 Martín, J.I., Nogués, J., Liu, K., Vicent, J. L. and Schuller, I.K. (2003) *J. Magn. Magn. Mater.*, **256**, 449–501.

38 Schwarzacher, W., Kasyutich, O.I., Evans, P.R., Darbyshire, M.G., Yi, G., Fedosyuk, V.M., Rousseaux, F., Cambril, E. and Decanini, D. (1999) *J. Magn. Magn. Mater.*, **198–199**, 185–190.

39 Maria, J., Jeon, S. and Rogers, J.A. (2004) *J. Photochem. Photobiol. A*, **166**, 149–154.

40 Lin, B.J. (2006) *Microelectron. Eng.*, **83**, 604–613.

41 Chou, S.Y., Krauss, P.R. and Kong, L. (1996) *J. Appl. Phys.*, **79**, 6101–6106.

42 Duvail, J.L., Dubois, S., Piraux, L., Vaurès, A., Fert, A., Adam, D., Champagne, M., Rousseaux, F. and Decanini, D. (1998) *J. Appl. Phys.*, **84**, 6359–6365.

43 Dumpich, G., Krome, T.P. and Hausmanns, B. (2002) *J. Magn. Magn. Mater.*, **248**, 241–247.

44 Papaioannou, E., Simeonidis, K., Valassiades, O., Vouroutis, N., Angelakeris, M., Ppolopoulos, P., Kostic, I. and Flevaris, N.K. (2004) *J. Magn. Magn. Mater.*, **272–276**, e1323–e1325.

45 Chen, A., Chua, S.J., Chen, P., Chen, X.Y. and Jian, L.K. (2006) *Nanotechnology*, **17**, 3903–3908.

46 Lodder, J.C. (2004) *J. Magn. Magn. Mater.*, **272–276**, 1692–1697.

47 Ji, Q., Chen, Y., Ji, L., Jiang, X. and Leung, K-N. (2006) *Microelectron. Eng.*, **83**, 796–799.

48 Miramond, C., Fermon, C., Rousseaux, F., Decanini, D. and Carcenac, F. (1997) *J. Magn. Magn. Mater.*, **165**, 500–503.

49 Turberfield, A.J. (2001) *MRS Bulletin*, August, 632–636.

50 Ross, C.A., Hwang, M., Shima, M., Smith, H.I., Farhoud, M., Savas, T.A., Schwarzacher, W., Parrochon, J., Escoffier, W., Neal Bertram, H., Humphrey, F.B. and Redjdal, M. (2002) *J. Magn. Magn. Mater.*, **249**, 200–207.

51 Rosa, W.O., de Araújo, A.E.P., Gobbi, A. L., Knobel, M. and Cescato, L. (2005) *J. Magn. Magn. Mater.*, **294**, e63–e67.

52 Chou, S.Y., Krauss, P.R. and Renstrom, P. R. (1996) *J. Vac. Sci. Technol. B*, **14**, 4129–4133.

53 Chou, S. (2003) *Technol Rev.*, February, 42–44.

54 Harnagea, C., Alexe, M., Schilling, J., Choi, J., Wehrspohn, R.B., Hesse, D. and Gösele, U. (2003) *Appl. Phys. Lett.*, **83**, 1827–1829.

55 Grujicic, D. and Pesic, B. (2005) *J. Magn. Magn. Mater.*, **288**, 196–204.

56 Li, W., Hsiao, G.S., Harris, D., Nyffenegger, R.M., Virtanen, J.A. and Penner, R.M. (1996) *J. Phys. Chem.*, **100**, 20103–20113.

57 Nyffenegger, R.M. and Penner, R.M. (1997) *Chem. Rev.*, **97**, 1195–1230.

58 Lee, S., Kim, J., Shin, S., Lee, H-J., Koo, S. and Lee, H. (2004) *Mater. Sci. Eng. C*, **24**, 3–9.

59 Kolb, D.M. and Simeone, F.C. (2005) *Electrochim. Acta*, **50**, 2989–2996.

60 Raimundo, D.S., Stelet, A.B., Fernandez, F.J.R. and Salcedo, W.J. (2005) *Microelectron. J.*, **36**, 207–211.

61 Jones, B.A., Searle, J.A. and O'Grady, K. (2005) *J. Magn. Magn. Mater.*, **290–291**, 131–133.

62 Komiyama, H., Yamaguchi, Y. and Noda, S. (2004) *Chem. Eng. Sci.*, **59**, 5085–5090.

63 Zhukov, A.A., Ghanem, M.A., Goncharov, A.V., Bartlett, P.N. and de Groot, P.A.J. (2004) *J. Magn. Magn. Mater.*, **272–276**, e1369–e1371.

64 Li, Y., Cai, W., Duan, G., Sun, F., Cao, B. and Lu, F. (2005) *Mater. Lett.*, **59**, 276–279.

65 Ma, W., Hesse, D. and Gösele, U. (2006) *Nanotechnology*, **17**, 2536–2541.

66 Teichert, C., Bean, J.C. and Lagally, M.G. (1998) *Appl. Phys. A*, **67**, 675–685.

67 Oster, J., Huth, M., Wiehl, L. and Adrian, H. (2004) *J. Magn. Magn. Mater.*, **272–276**, 1588–1589.

68 Schmidt, O.G., Rastelli, A., Kar, G.S., Songmuang, R., Kiravittaya, S., Stoffel, M., Denker, U., Stufler, S., Zrenner, A., Grützmacher, D., Nguyen, B-Y. and Wennekers, P. (2004) *Physica E*, **25**, 280–287.

69 Adair, J.H., Li, T., Kido, T., Havey, K., Moon, J., Mecholsky, J., Morrone, A., Talham, D.R., Ludwig, M.H. and Wang, L. (1998) *Mater. Sci. Eng. R*, **23**, 139–242.

70 Tartaj, P., Morales, M.P., González-Carreño, T., Veintemillas-Verdaguer, S. and Serna, C.J. (2005) *J. Magn. Magn. Mater.*, **290–291**, 28–34.

71 Vázquez, M., Luna, C., Morales, M.P., Sanz, R., Serna, C.J. and Mijangos, C. (2004) *Physica B*, **354**, 71–79.

72 Yakutik, I.M. and Shevchenko, G.P. (2004) *Surf. Sci.*, **566–568**, 414–418.

73 Kim, K.D., Han, D.N. and Kim, H.T. (2004) *Chem. Eng. J.*, **104**, 55–61.

74 Lee, G-J., Shin, S-I., Kim, Y-Ch. and Oh, S-G. (2004) *Mater. Chem. Phys.*, **84**, 197–204.

75 Chen, S., Feng, J., Guo, X., Hong, J. and Ding, W. (2005) *Mater. Lett.*, **59**, 985–988.

76 Zhou, H. and Li, Z. (2005) *Mater. Chem. Phys.*, **89**, 326–331.

77 Liu, Y-Ch. and Lin, L-H. (2004) *Electrochem. Commun.*, **6**, 1163–1168.

78 Zhang, J., Han, B., Liu, M., Liu, D., Dong, Z., Liu, J., Li, D., Wang, J., Dong, B., Zhao, H. and Rong, L. (2003) *J. Phys. Chem. B*, **107**, 3679–3683.

79 Murray, B.J., Li, Q., Newberg, J.T., Menke, E.J., Hemminger, J.C. and Penner, R.M. (2005) *Nano Lett.*, **5**, 2319–2324.

80 Völkel, B., Kaltenpoth, G., handrea, M., Sahre, M., Nottbohm, Ch.T., Küller, A., Paul, A., Kautek, W., Eck, W. and Gölzhäuser, A. (2005) *Surf. Sci.*, **597**, 32–41.

81 Wang, C., Chen, M., Zhu, G. and Lin, Z. (2001) *J. Colloid Interfac. Sci.*, **243**, 362–364.

82 Groves, J.T., Ulman, N. and Boxer, S.G. (1997) *Science*, **275**, 651–653.

83 Castellana, E.T. and Cremer, P.S. (2006) *Surf. Sci. Rep.*, **61**, 429–444.

84 Whang, D., Jin, S. and Lieber, C.M. (2003) *Nano Lett.*, **3**, 951–954.

85 Rao, C.N.R., Govindaraj, A., Gundiah, G. and Vivekchand, S.R.C. (2004) *Chem. Eng. Sci.*, **59**, 4665–4671.

86 Kim, Y., Kim, Ch. and Yi, J. (2004) *Mater. Res. Bull.*, **39**, 2103–2112.

87 Thiruchitrambalam, M., Palkar, V.R. and Gopinathan, V. (2004) *Mater. Lett.*, **58**, 3063–3066.

88 Pavasupree, S., Suzuki, Y., Pivsa-Art, S. and Yoshikawa, S. (2005) *Sci. Technol. Adv. Mater.*, **6**, 224–229.

89 Choi, H., Sofranko, A.C. and Dionysiou, D.D. (2006) *Adv. Funct. Mater.*, **16**, 1067–1074.

90 Yang, P., Deng, T., Zhao, D., Feng, P., Pine, D., Chmelka, B.F., Whitesides, G.M. and Stucky, G.D. (1998) *Science*, **282**, 2244–2246.

91 Karakassides, M.A., Gournis, D., Bourlinos, A.B., Trikalitis, P.N. and Bakas, T. (2003) *J. Mater. Chem.*, **13**, 871–876.

92 Zach, M.P. and Penner, R.M. (2000) *Adv. Mater.*, **12**, 878–883.

93 Liu, H., Favier, F., Ng, K., Zach, M.P. and Penner, R.M. (2001) *Electrochim. Acta*, **47**, 671–677.

94 Penner, R.M. (2002) *J. Phys. Chem. B*, **106**, 3339–3353.

95 Zach, M.P., Ng, K.H. and Penner, R.M. (2000) *Science*, **290**, 2120–2123.

96 Zach, M.P., Inazu, K., Ng, K.H., Hemminger, J.C. and Penner, R.M. (2002) *Chem. Mater.*, **14**, 3206–3216.

97 Walter, E.C., Zach, M.P., Favier, F., Murray, B., Inazu, K., Hemminger, J.C. and Penner, R.M. (2002) in *Physical Chemistry of Interface Nanomaterials*, (eds J.Z. Zhang and Z.L. Wang), Proceedings of the SPIE, Vol. 4807, pp. 83–92.

98 Walter, E.C., Ng, K., Zach, M.P., Penner, R.M. and Favier, F. (2002) *Microelectron. Eng.*, **61–62**, 555–561.

99 Walter, E.C., Murray, B.J., Favier, F., Kaltenpoth, G., Grunze, M. and Penner, R.M. (2002) *J. Phys. Chem.*, **106**, 11407–11411.

100 Walter, E.C., Zach, M.P., Favier, F., Murray, B.J., Inazu, K., Hemminger, J.C. and Penner, R.M. (2003) *ChemPhysChem.*, **4**, 131–138.

101 Walter, E.C., Murray, B.J., Favier, F. and Penner, R.M. (2003) *Adv. Mater.*, **15**, 396–399.

102 Atashbar, M.Z., Banerji, D., Singamaneni, S. and Bliznyuk, V. (2004) *Nanotechnology*, **15**, 374–378.

103 Li, Q., Olson, J.B. and Penner, R.M. (2004) *Chem. Mater.*, **16**, 3402–3405.

104 Li, Q., Walter, E.C., van der Veer, W.E., Murray, B.J., Newberg, J.T., Bohannan, E.W., Switzer, J.A., Hemminger, J.C. and Penner, R.M. (2005) *J. Phys. Chem. B*, **109**, 3169–3182.

105 Menke, E.J., Li, Q. and Penner, R.M. (2004) *Nano Lett.*, **4**, 2009–2014.

106 Petit, C., Legrand, J., Russier, V. and Pileni, M.P. (2002) *J. Appl. Phys.*, **91**, 1502–1508.

107 Mazur, M. (2004) *Electrochem. Commun.*, **6**, 400–403.

108 Shi, S., Sun, J., Zhang, J. and Cao, Y. (2005) *Physica B*, **362**, 231–235.

109 Liu, F-M. and Green, M. (2004) *J. Mater. Chem.*, **14**, 1526–1532.

110 Dryfe, R.A.W., Walter, E.C. and Penner, R.M. (2004) *ChemPhysChem.*, **5**, 1879–1884.

111 Yanagimoto, H., Deki, S., Akamatsu, K. and Gotoh, K. (2005) *Thin Solid Films*, **491**, 18–22.

112 Sun, L., Searson, P.C. and Chien, C.L. (1999) *Appl. Phys. Lett.*, **74**, 2803–2805.

113 Chien, C.L., Sun, L., Tanase, M., Bauer, L.A., Hultgren, A., Silevitch, D.M., Meyer, G.J., Searson, P.C. and Reich, D.H. (2002) *J. Magn. Magn. Mater.*, **249**, 146–155.

114 Ziegler, K.J., Polyakov, B., Kulkarni, J.S., Crowley, T.A., Ryan, K.M., Morris, M.A., Erts, D. and Holmes, J.D. (2004) *J. Mater. Chem.*, **14**, 585–589.

115 Kazakova, O., Erst, D., Crowley, T.A., Kulkarni, J.S. and Holmes, J.D. (2005) *J. Magn. Magn. Mater.*, **286**, 171–176.

116 Aylett, B.J., Earwaker, L.G., Forcey, K., Giaddui, T. and Harding, I.S. (1996) *J. Organometal. Chem.*, **521**, 33–37.

117 Rastei, M.V., Meckenstock, R., Devaux, E., Ebbesen, Th. and Bucher, J.P. (2005) *J. Magn. Magn. Mater.*, **286**, 10–13.

118 Matthias, S., Schilling, J., Nielsch, K., Müller, F., Wehrspohn, R.B. and Gösele, U. (2002) *Adv. Mater.*, **14**, 1618–1621.

119 Zhao, L., Yosef, M., Steinhart, M., Göring, P., Hofmeister, H., Gösele, U. and Schlecht, S. (2006) *Angew. Chem. Int. Ed.*, **45**, 311–315.

120 Martin, C.R. (1994) *Science*, **266**, 1961–1966.

121 Szklarczyk, M., Strawski, M., Donten, M.L. and Donten, M. (2004) *Electrochem. Commun.*, **6**, 880–886.

122 Ounadjela, K., Ferré, R., Louail, L., George, J.M., Maurice, J.L., Piraux, L. and Dubois, S. (1997) *J. Appl. Phys.*, **81**, 5455–5457.

123 Piraux, L., Dubois, S., Ferain, E., Legras, R., Ounadjela, K., George, J.M., Mayrice, J.L. and Fert, A. (1997) *J. Magn. Magn. Mater.*, **165**, 352–355.

124 Scarani, V., Doudin, B. and Ansermet, J-P. (1999) *J. Magn. Magn. Mater.*, **205**, 241–248.

125 Kazadi Mukenga Bantu, A., Rivas, J., Zaragoza, G., López-Uintela, M.A. and

Blanco, B.C. (2001) *J. Non-Crystall. Solids*, **287**, 5–9.

126 Kazadi Mukenga Bantu, A., Rivas, J., Zaragoza, G., López-Uintela, M.A. and Blanco, B.C. (2001) *J. Appl. Phys.*, **89**, 3393–3397.

127 Valizadeh, S., George, J.M., Leisner, P. and Hultman, L. (2001) *Electrochim. Acta*, **47**, 865–874.

128 Ge, S., Li, Ch., Ma, X., Li, W., Xi, L. and Li, C.X. (2001) *J. Appl. Phys.*, **90**, 509–511.

129 Ge, S., Ma, X., Li, Ch. and Li, W. (2001) *J. Magn. Magn. Mater.*, **226–230**, 1867–1869.

130 Encinas, A., Demand, M., George, J-M. and Piraux, L. (2002) *IEEE Trans. Magn.*, **38**, 2574–2576.

131 Vila, L., George, J.M., Faini, G., Popa, A., Ebels, U., Ounadjela, K. and Piraux, L. (2002) *IEEE Trans. Magn.*, **38**, 2577–2579.

132 Rivas, J., Kazadi Mukenga Bantu, A., Zaragoza, G., Blanco, M.C. and López-Quintela, M.A. (2002) *J. Magn. Magn. Mater.*, **249**, 220–227.

133 Demand, M., Encinas-Oropesa, A., Kenane, S., Ebels, U., Huynen, I. and Piraux, L. (2002) *J. Magn. Magn. Mater.*, **249**, 228–233.

134 Motoyama, M., Fukunaka, Y., Sakka, T., Ogata, Y.H. and Kikuchi, S. (2005) *J. Electroanal. Chem.*, **584**, 84–91.

135 Konishi, Y., motoyama, M., Matsushima, H., Fukunaka, Y., Ishii, R. and Ito, Y. (2003) *J. Electroanal. Chem.*, **559**, 149–153.

136 Dubois, S., Michel, A., Eymery, J.P., Duvail, J.L. and Piraux, L. (1999) *J. Mater. Res.*, **14**, 665–671.

137 Han, G.C., Zong, B.Y. and Wu, Y.H. (2002) *IEEE Trans. Magn.*, **38**, 2562–2564.

138 Blondel, A., Meier, J.P., Doudin, B. and Ansermet, J-Ph. (1994) *Appl. Phys. Lett.*, **65**, 3019–3021.

139 Piraux, L., George, J.M., Despres, J.F., Leroy, C., Ferain, E., Legras, R., Ounadjela, K. and Fert, A. (1994) *Appl. Phys. Lett.*, **65**, 2484–2486.

140 Dubois, S., Beuken, J.M., Piraux, L., Duvail, J.L., Fert, A., George, J.M. and Maurice, J.L. (1997) *J. Magn. Magn. Mater.*, **165**, 30–33.

141 Piraux, L., Dubois, S., Duvail, J.D., Ounadjela, K. and Fert, A. (1997) *J. Magn. Magn. Mater.*, **175**, 127–136.

142 Maurice, J-L., Imhoff, D., Etienne, P., Dubois, O., Piraux, L., George, J-M., Galtier, P. and Fret, A. (1998) *J. Magn. Magn. Mater.*, **184**, 1–18.

143 Dubois, S., Marchal, C., Beuken, J.M., Piraux, L., Fert, A., George, J.M. and Maurice, J.L. (1997) *Appl. Phys. Lett.*, **70**, 396–398.

144 Valizadeh, S., George, J.M., Leisner, P. and Hultman, L. (2002) *Thin Solid Films*, **402**, 262–271.

145 Xue, S.H. and Wang, Z.D. (2006) *Mater. Sci. Eng. B*, **135**, 74–77.

146 Piraux, L., Dubois, S., Duvail, J.L., Radulescu, A., Demoustier-Champagne, S., Ferain, E. and Legras, R. (1999) *J. Mater. Res.*, **14**, 3042–3050.

147 Curiale, J., Sánchez, R.D., Troiani, H.E., Pastoriza, H., levy, P. and Leyva, A.G. (2004) *Physics B*, **354**, 98–103.

148 Park, I-W., Yoon, M., Kim, Y.M., Kim, Y., Kim, J.H., Kim, S. and Volkov, V. (2004) *J. Magn. Magn. Mater.*, **272–276**, 1413–1414.

149 Huang, E., Rockford, L., Russell, T.P. and Hawker, C.J. (1998) *Nature*, **395**, 757–758.

150 Otsuka, H., Nagasaki, Y. and Kataoka, K. (2001) *Mater. Today*, **4** (May/June), 30–36.

151 Hamley, I.W. (2003) *Nanotechnology*, **14**, R39–R54.

152 Yalçın, O., Yıldız, F., Özdemir, M., Aktaş, B., Köseoğlu, Y., Bal, M. and Tuominen, M.T. (2004) *J. Magn. Magn. Mater.*, **272–274**, 1684–1685.

153 Jeoung, E., Galow, T.H., Schotter, J., Bal, M., Ursache, A., Tuominen, M.T., Stafford, C.M., Russell, T.P. and Rotello, V.M. (2001) *Langmuir*, **17**, 6396–6398.

154 Wu, X.C. and Tao, Y.R. (2004) *J. Cryst. Growth*, **242**, 309–312.

155 Wang, L., Zhang, X., Zhao, S., Zhou, G., Zhou, Y. and Qi, J. (2005) *Mater. Res. Soc. Symp. Proc.*, **879E**, Z3.21.1–Z3.21.6.

156 Huang, M.H., Mao, S., Feick, H., Yan, H., Wu, Y., Kind, H., Weber, E., Russo, R. and Yang, P. (2001) *Science*, **292**, 1897–1899.

157 Xu, C.X., Sun, X.W., Dong, Z.L. and Yu, M.B. (2004) *J. Cryst. Growth*, **270**, 498–504.

158 Stelzner, T., Andrä, G., Wendler, E., Weschl, W., Scholz, R., Gösele, U. and Christiansen, S.H. (2006) *Nanotechnology*, **17**, 2895–2898.

159 Chou, S.Y. and Zhuang, L. (1999) *J. Vac. Sci. Technol. B*, **17**, 3197–3202.

160 Chou, S.Y., Keimel, C. and Gu, J. (2002) *Nature*, **417**, 835–837.

161 Szafraniak, I., Hesse, D. and Alexe, M. (2005) *Solid State Phenomena*, **106**, 117–122.

162 Yasuda, H., Ohnaka, I., Fujimoto, S., Sugiyama, A., Hayashi, Y., Yamamoto, M., Tsuchiyama, A., Nakano, T., Uesugi, K. and Kishio, K. (2004) *Mater. Lett.*, **58**, 911–915.

163 Hassel, A.W., Bello-Rodriguez, B., Milenkovic, S. and Schneider, A. (2005) *Electrochim. Acta*, **50**, 3033–3039.

164 Yasuda, H., Ohnaka, I., Fujimoto, S., Takezawa, N., Tsuchiyama, A., Nakano, T. and Uesugi, K. (2006) *Scripta Mater.*, **54**, 527–532.

165 Grüning, U., Lehmann, V., Ottow, S. and Busch, K. (1996) *Appl. Phys. Lett.*, **68**, 747–749.

166 Jessensky, O., Müller, F. and Gösele, U. (1997) *Thin Solid Films*, **297**, 224–228.

167 Birner, A., Grüning, U., Ottow, S., Schneider, A., Müller, F., Lehmann, V., Föll, H. and Gösele, U. (1998) *Phys. Stat. Sol. A*, **165**, 111–117.

168 Motohashi, A. (2000) *Jpn. J. Appl. Phys.*, **39**, 363–367.

169 Bisi, O., Ossicini, S. and Pavesi, L. (2000) *Surf. Sci. Rep.*, **38**, 1–126.

170 Hamm, D., Sasano, J., Sakka, T. and Ogata, Y.H. (2002) *J. Electrochem. Soc.*, **149**, C331–C337.

171 Chazalviel, J-N., Ozanam, F., Gabouze, N., Fellah, S. and Wehrspohn, R.B. (2002) *J. Electrochem. Soc.*, **149**, C511–C520.

172 Föll, H., Christophersen, M., Carstensen, J. and Hasse, G. (2002) *Mater. Sci. Eng. R*, **39**, 94–141.

173 Seo, M. and Yamaya, T. (2005) *Electrochim. Acta*, **51**, 787–794.

174 Hasegawa, H. and Sato, T. (2005) *Electrochim. Acta*, **50**, 3015–3027.

175 Choi, J., Wehrspohn, R.B., Lee, J. and Gösele, U. (2004) *Electrochim. Acta*, **49**, 2645–2652.

176 Bourdet, P., Vacandio, F., Argème, L., Rossi, S. and Massiani, Y. (2005) *Thin Solid Films*, **483**, 205–210.

177 Macak, J.M., Sirotna, K. and Schmuki, P. (2005) *Electrochim. Acta*, **50**, 3679–3684.

178 Prida, V.M., Hernández-Vélez, M., Cervera, M., Pirota, K., Sanz, R., Navas, D., Asenjo, A., Aranda, P., Ruiz-Hitzky, E., Batallán, F., Vázquez, M., Hernando, B., Menéndez, A., Bordel, N. and Pereiro, R. (2005) *J. Magn. Magn. Mater.*, **294**, e69–e72.

179 Raja, K.S., Misra, M. and Paramguru, K. (2005) *Electrochim. Acta*, **51**, 154–165.

180 Raja, K.S., Misra, M. and Paramguru, K. (2005) *Mater. Lett.*, **59**, 2137–2141.

181 Tsuchiya, H., Macak, J.M., Ghicov, A., Taveira, L. and Schmuki, P. (2005) *Corros. Sci.*, **47**, 3324–3335.

182 Zhao, J., Wang, X., Chen, R. and Li, L. (2005) *Solid State Commun.*, **134**, 705–710.

183 Bayoumi, F.M. and Ateya, B.G. (2006) *Electrochem. Commun.*, **8**, 38–44.

184 Ricker, R.E., Miller, A.E., Yue, D-F., Banerjee, G. and Bandyopadhyay, S. (1996) *J. Electron. Mater.*, **25**, 1585–1592.

185 Yuzhakov, V.V., Chang, H-Ch. and Miller, A.E. (1997) *Phys. Rev. B*, **56**, 12608–12624.

186 Tsuchiya, H. and Schmuki, P. (2004) *Electrochem. Commun.*, **6**, 1131–1134.

187 Sieber, I., Hildebrand, H., Friedrich, A. and Schmuki, P. (2005) *Electrochem. Commun.*, **7**, 97–100.

188 Karlinsey, R.L. (2005) *Electrochem. Commun.*, **7**, 1190–1194.

189 Heidelberg, A., Rozenkranz, C., Schultze, J.W., Schäpers, Th. and Staikov, G. (2005) *Surf. Sci.*, **597**, 173–180.

190 Habazaki, H., Ogasawara, T., Konno, H., Shimizu, K., Asami, K., Saito, K., Nagata, S., Skeldon, P. and Thompson, G.E. (2005) *Electrochim. Acta*, **50**, 5334–5339.

191 Tsuchiya, H. and Schmuki, P. (2005) *Electrochem. Commun.*, **7**, 49–52.

192 Shin, H.-C., Dong, J. and Liu, M. (2004) *Adv. Mater.*, **16**, 237–240.

193 Cochran, W.C. and Keller, F. (1963) in *The Finishing of Aluminum* (ed. G.H. Kissin), New York Reinhold Publishing Corporation, pp. 104–126.

194 Lowenheim, F.A. (1978) in *Electroplating*, McGraw-Hill Book Company New York, pp. 452–478.

195 Wernick, S., Pinner, R. and Sheasby, P.G. (1987) in *The Surface Treatment and Finishing of Aluminium and its Alloys*, ASM International, Finishing Publication Ltd., 5th edition, pp. 289–368.

196 Jelinek, T.W. (1997) in *Oberflächenbehandlung von Aluminium*, Eugen G. Leuze Verlag –D –88348 Saulgau/Württ, pp. 187–219 (in German).

197 Keller, F., Hunter, M.S. and Robinson, D.L. (1953) *J. Electrochem. Soc.*, **100**, 411–419.

198 Young, L. (1961) in *Anodic Oxide Films*, Academic Press, London and New York, pp. 193–221.

199 Despić, A.R. (1985) in *J. Electroanal. Chem.*, **191**, 417–423.

200 Thompson, G.E. and Wood, G.C. (1983) in *Treatise on Materials Science and Technology*, (ed. J.C. Scully), Academic Press New York, Vol. 23, pp. 205–329.

201 Pakes A., Thompson, G.E., Skeldon, P., Morgan, P.C. and Shimizu, K. (1999) *Trans. IMF*, **77**, 171–177.

202 Despić, A. and Parkhutik, V.P. (1989) in *Modern Aspects of Electrochemistry*, (eds J.O'M. Bockris, R.E. White and B.E. Conway), Plenum Press, New York and London, Vol. 20, pp. 401–503.

203 Thompson G.E. (1997) *Thin Solid Films*, **297**, 192–201.

204 Zhu, X.F., Li, D.D., Song, Y. and Xiao, Y.H. (2005) *Mater. Lett.*, **59**, 3160–3163.

205 Diggle, J.W., Downie, T.C. and Goulding, C.W. (1969) *Chem. Rev.*, **69**, 365–405.

206 Takahashi, H., Fujimoto, K. and Nagayama, M. (1988) *J. Electrochem. Soc.*, **135**, 1349–1353.

207 Morks, M.F., Hamdy, A.S., Fahim, N.F. and Shoeib, M.A. (2006) *Surf. Coat. Technol.*, **200**, 5071–5076.

208 O'Sullivan, J.P. and Wood, G.C. (1970) *Proc. Roy. Soc. Lond. A*, **317**, 511–543.

209 Surganov, V., Morgen, P., Nielsen, J.C., Gorokh, G. and Mozalev, A. (1987) *Electrochim. Acta*, **32**, 1125–1127.

210 Surganov, V., Gorokh, G., Poznyak, A. and Mozalev, A. (1988) *Zhur. Prikl. Khimii (Russ. J. Appl. Chem.)*, **61**, 2011–2014 (in Russian).

211 Ono, S., Saito, M. and Asoh, H. (2005) *Electrochim. Acta*, **51**, 827–833.

212 Surganov, V. and Gorokh, G. (1993) *Mater. Lett.*, **17**, 121–124.

213 Chu, S.Z., Wada, K., Inoue, S., Isogai, M., Katsuta, Y. and Yasumori, A. (2006) *J. Electrochem. Soc.*, **153**, B384–B391.

214 Mozalev, A., Surganov, A. and Magaino, S. (1999) *Electrochim. Acta*, **44**, 3891–3898.

215 Surganov, V. and Gorokh, G. (1993) *Zhur. Prikl. Khimii (Russ. J. Appl. Chem.)*, **66**, 683–685 (in Russian).

216 Ono, S., Saito, M., Ishiguro, M. and Asoh, H. (2004) *J. Electrochem. Soc.*, **151**, B473–B478.

217 Mozalev, A., Mozaleva, I., Sakairi, M. and Takahashi, H. (2005) *Electrochim. Acta*, **50**, 5065–5075.

218 Zhou, X., Thompson, G.E. and Potts, G. (2000) *Trans. IMF*, **78**, 210–214.

219 Wang, H. and Wang, H.W. (2006) *Mater. Chem. Phys.*, **97**, 213–218.

220 Jia, Y., Zhou, H., Luo, P., Luo, S., Chen, J. and Kuang, Y. (2006) *Surf. Coat. Technol.*, **201**, 513–518.

221 Mozalev, A., Poznyak, A., Mozaleva, I. and Hassel, A.W. (2001) *Electrochem. Commun.*, **3**, 299–305.

222 Shingubara, S., Morimoto, K., Sakaue, H. and Takahagi, T. (2004) *Electrochem. Solid-State Lett.*, **7**, E15–E17.

223 Choo, Y.H. and Devereux, O.F. (1975) *J. Electrochem. Soc.*, **122**, 1645–1653.

224 Shimizu, K., Kobayashi, K., Thompson, G.E. and Wood, G.C. (1992) *Phil. Mag. A*, **66**, 643–652.

225 Arrowsmith, D.J. and Moth, D.A. (1986) *Trans. IMF*, **64**, 91–93.

226 Sulka, G.D. and Jaskuła, M. (2006) *J. Nanosci. Nanotechnol.*, **6**, 3803–3811.

227 Palibroda, E., Farcas, T. and Lupsan, A. (1995) *Mater. Sci. Eng. B*, **32**, 1–5.

228 Martin, T. and Hebert, K.R. (2001) *J. Electrochem. Soc.*, **148**, B101–B109.

229 Abdel-Gaber, A.M., Abd-El-Nabey, B.A., Sidahmed, I.M., El-Zayady, A.M. and Saadawy, M. (2006) *Mater. Chem. Phys.*, **98**, 291–297.

230 Ono, S., Saito, M. and Asoh, H. (2004) *Electrochem. Solid-State Lett.*, **7**, B21–B24.

231 Sulka, G.D., Stroobants, S., Moshchalkov, V., Borghs, G. and Celis, J-P. (2004) *J. Electrochem. Soc.*, **151**, B260–B264.

232 Wood, G.C., O'Sullivan, J.P. and Vaszko, B. (1968) *J. Electrochem. Soc.*, **115**, 618–620.

233 Paolini, G., Masaero, M., Sacchi, F. and Paganelli, M. (1965) *J. Electrochem. Soc.*, **112**, 32–38.

234 Palibroda, E. (1984) *Surf. Technol.*, **23**, 341–351 (in French).

235 Nielsch, K., Choi, J., Schwirn, K., Wehrspohn, R.B. and Gösele, U. (2002) *Nano Lett.*, **2**, 677–680.

236 Li, F., Zhang, L. and Metzger, R.M. (1998) *Chem. Mater.*, **10**, 2470–2480.

237 Ebihara, K., Takahashi, H. and Nagayama, M. (1983) *J. Met. Finish. Soc. Japan (Kinzoku Hyomen Gijutsu)*, **34**, 548–553 (in Japanese).

238 Ebihara, K., Takahashi, H. and Nagayama, M. (1982) *J. Met. Finish. Soc. Japan (Kinzoku Hyomen Gijutsu)*, **33**, 156–164 (in Japanese).

239 Parkhutik, V.P. and Shershulsky, V.I. (1992) *J. Phys. D: Appl. Phys.*, **25**, 1258–1263.

240 Sulka, G.D. and Parkoła, K.G. (2007) *Electrochim. Acta*, **52**, 1880–1888.

241 Hwang, S-K., Jeong, S-H., Hwang, H-Y., Lee, O-J. and Lee, K-H. (2002) *Korean J. Chem. Eng.*, **19**, 467–473.

242 Marchal, D. and Demé, B. (2003) *J. Appl. Cryst.*, **36**, 713–717.

243 Hunter, M.S. and Fowle, P.E. (1954) *J. Electrochem. Soc.*, **101**, 481–485.

244 Hunter, M.S. and Fowle, P.E. (1954) *J. Electrochem. Soc.*, **101**, 514–519.

245 Vrublevsky, I., Parkoun, V. and Schreckenbach, J. (2005) *Appl. Surf. Sci.*, **242**, 333–338.

246 Vrublevsky, I., Parkoun, V., Sokol, V. and Schreckenbach, J. (2005) *Appl. Surf. Sci.*, **252**, 227–233.

247 Vrublevsky, I., Parkoun, V., Schreckenbach, J. and Marx, G. (2004) *Appl. Surf. Sci.*, **227**, 282–292.

248 Sulka, G.D. and Parkoła, K. (2006) *Thin Solid Films*, **515**, 338–345.

249 Ono, S. and Masuko, N. (2003) *Surf. Coat. Technol.*, **169–170**, 139–142.

250 Ono, S., Asoh, H., Saito, M. and Ishiguro, M. (2003) *Electrochemistry*, **71**, 105–107 (in Japanese).

251 Chu, S-Z., Wada, K., Inoue, S., Isogai, M. and Yasumori, A. (2005) *Adv. Mater.*, **17**, 115–2119.

252 Nakamura, S., Saito, M., Huang, Li-F., Miyagi, M. and Wada, K. (1992) *Jpn. J. Appl. Phys.*, **31**, 3589–3593.

253 Bocchetta, P., Sunseri, C., Bottino, A., Capannelli, G., Chiavarotti, G., Piazza, S. and Di Quarto, F. (2002) *J. Appl. Electrochem.*, **32**, 977–985.

254 Palibroda, E. (1995) *Electrochim. Acta*, **40**, 1051–1055.

255 Wood, G.C. and O'Sullivan, J.P. (1970) *Electrochim. Acta*, **15**, 1865–1876.

256 Xu, Y., Thompson, G.E., Wood, G.C. and Bethune, B. (1987) *Corros. Sci.*, **27**, 83–102.

257 Wood, G.C., Skeldon, P., Thompson, G.E. and Shimizu, K. (1996) *J. Electrochem. Soc.*, **143**, 74–83.

258 Habazaki, H., Shimizu, K., Skeldon, P., Thompson, G.E., Wood, G.C. and Zhou, X. (1997) *Corros. Sci.*, **39**, 731–737.

259 Thompson, G.E., Skeldon, P., Shimizu, K. and Wood, G.C. (1995) *Phil. Trans. R. Soc. Lond. A*, **350**, 143–168.

260 Shimizu, K., Brown, G.M., Kobayashi, K., Skeldon, P., Thompson, G.E. and Wood, G.C. (1999) *Corros. Sci.*, **41**, 1835–1847.

261 Shimizu, K., Habazaki, H., Skeldon, P., Thompson, G.E. and Wood, G.C. (1999) *Surf. Interface Anal.*, **27**, 1046–1049.

262 Shimizu, K., Brown, G.M., Habazaki, H., Kobayashi, K., Skeldon, P., Thompson, G. E. and Wood, G.C. (1999) *Surf. Interface Anal.*, **27**, 24–28.

263 Shimizu, K., Brown, G.M., Habazaki, H., Kobayashi, K., Skeldon, P., Thompson, G. E. and Wood, G.C. (1999) *Surf. Interface Anal.*, **27**, 153–156.

264 Shimizu, K., Habazaki, H., Skeldon, P., Thompson, G.E. and Wood, G.C. (1999) *Surf. Interface Anal.*, **27**, 998–1002.

265 Shimizu, K., Brown, G.M., Habazaki, H., Kobayashi, K., Skeldon, P., Thompson, G. E. and Wood, G.C. (1999) *Electrochim. Acta*, **44**, 2297–2306.

266 Shimizu, K., Habazaki, H., Skeldon, P., Thompson, G.E. and Wood, G.C. (2000) *Electrochim. Acta*, **45**, 1805–1809.

267 Ono, S., Wada, Ch. and Asoh, H. (2005) *Electrochim. Acta*, **50**, 5103–5110.

268 Takahashi, H., Fujimoto, K., Konno, H. and Nagayama, M. (1984) *J. Electrochem. Soc.*, **131**, 1856–1861.

269 Habazaki, H., Shimizu, K., Skeldon, P., Thompson, G.E. and Zhou, X. (1997) *Corros. Sci.*, **39**, 719–730.

270 Ono, S. and Masuko, N. (1992) *Corros. Sci.*, **33**, 503–507.

271 Patermarakis, G. and Pavlidou, C. (1994) *J. Catal.*, **147**, 140–155.

272 Patermarakis, G., Moussoutzanis, K. and Nikolopoulos, N. (1999) *J. Solid State Electrochem.*, **3**, 193–204.

273 Patermarakis, G., Chandrinos, J. and Moussoutzanis, K. (2001) *J. Electroanal. Chem.*, **510**, 59–66.

274 Thompson, G.E., Furneaux, R.C., Wood, G.C., Richardson, J.A. and Goode, J.S. (1978) *Nature*, **272**, 433–435.

275 Ono, S. and Masuko, N. (1992) *Corros. Sci.*, **33**, 841–850.

276 Patermarakis, G. and Kerassovitou, P. (1992) *Electrochim. Acta*, **3**, 125–137.

277 Palibroda, E. and Marginean, P. (1994) *Thin Solid Films*, **240**, 73–75.

278 Alwitt, R.S., Dyer, C.K. and Noble, B. (1982) *J. Electrochem. Soc.*, **129**, 711–717.

279 Ono, S., Ichinose, H. and Masuko, N. (1991) *J. Electrochem. Soc.*, **138**, 3705–3710.

280 Ono, S., Ichinose, H. and Masuko, N. (1992) *J. Electrochem. Soc.*, **139**, L80–L81.

281 Mei, Y.F., Wu, X.L., Shao, X.F., Huang, G. S. and Siu, G.G. (2003) *Phys. Lett. A*, **309**, 109–113.

282 Pu, L., Chen, Z-Q., Tan, Ch., Yang, Z., Zou, J-P., Bao, X-M., Feng, D., Shi, Y. and Zheng, Y-D. (2002) *Chin. Phys. Lett.*, **19**, 391–394.

283 Macdonald, D.D. (1992) *J. Electrochem. Soc.*, **139**, 3434–3449.

284 Macdonald, D.D., Biaggio, S.R. and Song, H. (1992) *J. Electrochem. Soc.*, **139**, 170–177.

285 Macdonald, D.D. (1993) *J. Electrochem. Soc.*, **140**, L27–L30.

286 Thompson, G.E., Furneaux, R.C. and Wood, G.C. (1978) *Corros. Sci.*, **18**, 481–498.

287 Thompson, G.E., Xu, Y., Skeldon, P., Shimizu, K., Han, S.H. and Wood, G.C. (1987) *Phil. Mag. B*, **55**, 651–667.

288 Shimizu, K., Thompson, G.E. and Wood, G.C. (1981) *Thin Solid Films*, **81**, 39–44.

289 Thompson, G.E., Wood, G.C. and Williams, J.Q. (1986) *Chemtronics*, **1**, 125–129.

290 Ono, S., Ichinose, H., Kawaguchi, T. and Masuko, N. (1990) *Corros. Sci.*, **31**, 249–254.

291 Parkhutik, V.P., Belov, V.T. and Chernyckh, M.A. (1990) *Electrochim. Acta*, **35**, 961–966.

292 Brown, I.W.M., Bowden, M.E., Kemmitt, T. and MacKenzie, K.J.D. (2006) *Curr. Appl. Phys.*, **6**, 557–561.

293 Yakovleva, N.M., Yakovlev, A.N. and Chupakhina, E.A. (2000) *Thin Solid Films*, **366**, 37–42.

294 Gabe, D.R. (2000) *Trans. IMF*, **78**, 207–209.

295 Liu, Y., Alwitt, R.S. and Shimizu, K. (2000) *J. Electrochem. Soc.*, **147**, 1382–1387.

296 Lu, Q., Skeldon, P., Thompson, G.E., Habazaki, H. and Shimizu, K. (2005) *Thin Solid Films*, **471**, 118–122.

297 Hernández, A., Martínez, F., Martín, A. and Prádanos, P. (1995) *J. Coll. Interface Sci.*, **173**, 284–296.

298 Theodoropoulou, M., Karahaliou, P.K., Georgia, S.N., Krontiras, C.A., Pisanias, M.N., Kokonou, M. and Nassiopoulou, A. G. (2005) *Ionics*, **11**, 236–239.

299 Lee, C.W., Kang, H.S., Chang, Y.H. and Hahm, Y.M. (2000) *Korean J. Chem. Eng.*, **17**, 266–272.

300 Yang, S.G., Li, T., Huang, L.S., Tang, T., Zhang, J.R., Gu, B.X., Du, Y.W., Shi, S.Z. and Lu, Y.N. (2003) *Phys. Lett. A*, **318**, 440–444.

301 Hoang, V.V. and Oh, S.K. (2004) *Physica B*, **352**, 73–85.

302 Mata-Zamora, M.E. and Saniger, J.M. (2005) *Rev. Mex. Fis.*, **51**, 502–509.

303 Xu, W.L., Zheng, M.J., Wu, S. and Shen, W.Z. (2004) *Appl. Phys. Lett.*, **85**, 4364–4366.

304 Borca-Tasciuc, D-A. and Chen, G. (2005) *J. Appl. Phys.*, **97**, 084303/1-9.

305 Chen, C.C., Chen, J.H. and Chao, Ch.G. (2005) *Jpn. J. Appl. Phys.*, **44**, 1529–1533.

306 Xia, Z., Riester, L., Sheldon, B.W., Curtin, W.A., Liang, J., Yin, A. and Xu, J.M. (2004) *Rev. Adv. Mater. Sci.*, **6**, 131–139.

307 Chen, C.H., Takita, K., Honda, S. and Awaji, H. (2005) *J. Eur. Ceram. Soc.*, **25**, 385–391.

308 Kato, S., Nigo, S., Uno, Y., Onisi, T. and Kido, G. (2006) *J. Phys.: Conference Series*, **38**, 148–151.

309 Fernandes, J.C.S., Picciochi, R., Da Cunha Belo, M., Moura e Silva, T., Ferreira, M.G.S. and Fonseca, I.T.E. (2004) *Electrochim. Acta*, **49**, 4701–4707.

310 Karahaliou, P.K., Theodoropulou, M., Krontiras, C.A., Xanthopoulos, N., Georga, S.N. and Pisanias, M.N. (2004) *J. Appl. Phys.*, **95**, 2776–2780.

311 Theodoropoulou, M., Karahaliou, P.K., Georgia, S.N., Krontiras, C.A., Pisanias, M.N., Kokonou, M. and Nassiopoulou, A. G. (2005) *J. Phys.: Conference Series*, **10**, 222–225.

312 Zabala, N., Pattantyus-Abraham, A.G., Rivacoba, A., García de Abajo, F.J. and Wolf, M.O. (2003) *Phys. Rev. B*, **68**, 245407/1-13.

313 Oh, H-J., Park, G-S., Kim, J-G., Jeong, Y. and Chi, Ch-S. (2003) *Mater. Chem. Phys.*, **82**, 331–334.

314 Redón, R., Vázquez-Olmos, A., Mata-Zamora, M.E., Ordóñez-Medrano, A., Rivera-Torres, F. and Saniger, J.M. (2006) *Rev. Adv. Mater. Sci.*, **11**, 79–87.

315 Alvine, K.J., Shpyrko, O.G., Pershan, P.S., Shin, K. and Russell, T.P. (2006) *Phys. Rev. Lett.*, **97**, 175503/1-4.

316 Thompson, D.W., Snyder, P.G., Castro, L. and Yan, L. (2005) *J. Appl. Phys.*, **97**, 113511/1-9.

317 Zhang, D-X., Zhang, H-J., Lin, X-F. and He, Y-L. (2006) *Spectroscopy Spectral Anal.*, **26**, 411–414. (in Chinese).

318 Xu, W.L., Chen, H., Zheng, M.J., Ding, G. Q. and Shen, W.Z. (2006) *Optital Mater.*, **28**, 1160–1165.

319 Hohlbein, J., Rehn, U. and Wehrspohn, R.B. (2004) *Phys. Stat. Sol. A*, **201**, 803–807.

320 Chen, J., Cai, W-L. and Mou, J-M. (2001) *J. Inorgan. Mater.*, **16**, 677–682. (in Chinese).

321 Kokonou, M., Nassiopoulou, A.G. and Travlos, A. (2003) *Mater. Sci. Eng. B*, **101**, 65–70.

322 Yang, Y., Chen, H-L. and Bao, X-M. (2003) *Acta Chim. Sinica*, **61**, 320–324 (in Chinese).

323 Huang, G.S., Wu, X.L., Siu, G.G. and Chu, P.K. (2006) *Solid State Commun.*, **137**, 621–624.

324 Chen, J.H., Huang, C.P., Chao, C.G. and Chen, T.M. (2006) *Appl. Phys. A*, **84**, 297–300.

325 Du, Y., Cai, W.L., Mo, C.M., Chen, J., Zhang, L.D. and Zhu, X.G. (1999) *Appl. Phys. Lett.*, **74**, 2951–2953.

326 Huang, G.S., Wu, X.L., Kong, F., Cheng, Y.C., Siu, G.G. and Chu, P.K. (2006) *Appl. Phys. Lett.*, **89**, 073114/1–3.

327 Yang, Y. and Gao, Q. (2004) *Phys. Lett. A*, **333**, 328–333.

328 Shi, Y.-L., Zhang, X-G. and Li, H-L. (2001) *Spectroscopy Lett.*, **34**, 419–426.

329 de Azevedo, W.M., de Carvalho, D.D., Khoury, H.J., de Vasconcelos, E.A. and da Silva, E.F. Jr. (2004) *Mater. Sci. Eng. B*, **112**, 171–174.

330 Stojadinovic, S., Zekovic, Lj., Belca, I., Kasalica, B. and Nikolic, D. (2004) *Electrochem. Commun.*, **6**, 708–712.

331 Kasalica, B., Stojadinovic, S., Zekovic, Lj., Belca, I. and Nikolic, D. (2005) *Electrochem. Commun.*, **7**, 735–739.

332 Stojadinovic, S., Belca, I., Kasalica, B., Zekovic, Lj. and Tadic, M. (2006) *Electrochem. Commun.*, **8**, 1621–1624.

333 Hoar, T.P. and Yahalom, J. (1963) *J. Electrochem. Soc.*, **110**, 614–621.

334 Kanakala, R., Singaraju, P.V., Venkat, R. and Das, B. (2005) *J. Electrochem. Soc.*, **152**, J1–J5.

335 Tsangaraki-Kaplanoglou, I., Theohari, S., Dimogerontakis, Th., Wang, Y-M., Kuo, H-H. and Kia, S. (2006) *Surf. Coat. Technol.*, **200**, 2634–2641.

336 Dimogerontakis, Th. and Kaplanoglou, I. (2001) *Thin Solid Films*, **385**, 182–189.

337 Dimogerontakis, Th. and Kaplanoglou, I. (2002) *Thin Solid Films*, **402**, 121–125.

338 Dimogerontakis, T. and Tsangaraki-Kaplanoglou, I. (2003) *Plating Surf. Finish.*, May, 80–82.

339 Li, Y., Zheng, M., Ma, L. and Shen, W. (2006) *Nanotechnology*, **17**, 5101–5105.

340 Inada, T., Uno, N., Kato, T. and Iwamoto, Y. (2005) *J. Mater. Res.*, **20**, 114–120.

341 Kneeshaw, J.A. and Gabe, D.R. (1984) *Trans. IMF*, **62**, 59–63.

342 Gabe, D.R. (1987) *Trans. IMF*, **65**, 152–154.

343 Li, L. (2000) *Solar Energ. Mater. Solar Cells*, **64**, 279–289.

344 De Graeve, I., Terryn, H. and Thompson, G.E. (2006) *Electrochim. Acta*, **52**, 1127–1134.

345 Setoh, S. and Miyata, A. (1932) *Sci. Pap. Inst. Phys.Chem. Res. Tokyo*, **17**, 189–236.

346 Wernick, S. (1934) *J. Electrodepos. Tech. Soc.*, **9**, 153–176.

347 Rummel, T. (1936) *Z. Physik*, **99**, 518–551 (in German).

348 Baumann, W. (1936) *Z. Physik*, **102**, 59–66 (in German).

349 Baumann, W. (1939) *Z. Physik*, **111**, 707–736 (in German).

350 Akahori, H. (1961) *J. Electron Microscopy (Tokyo)*, **10**, 175–185.

351 Murphy, J.F. and Michaelson, C.E. (1962) in Proceedings Conference on Anodizing, University of Notthingham, UK, 12–14 September 1961, Aluminium Development Association, London pp. 83–95.

352 Csokan, P. (1980) in *Advances in Corrosion Science and Technology,* (eds M.G. Fontana and R.W. Staehle), Plenum Press New York and London Vol. 7, pp. 239–356.

353 Ginsberg H. and Wefers, K. (1962) *Metall.*, **16**, 173–175 (in German).

354 Ginsberg, H. and Wefers, K. (1963) *Metall.*, **17**, 202–209 (in German).

355 Ginsberg, H. and Wefers, K. (1961) *Aluminium (Dusseldorf)*, **37**, 19–28 (in German).

356 Ginsberg, H. and Kaden, W. (1963) *Aluminium (Dusseldorf)*, **39**, 33–41 (in German).

357 De Graeve, I., Terryn, H. and Thompson, G.E. (2002) *J. Appl. Electrochem.*, **32**, 73–83.

358 Garcia-Vergara, S.J., Skeldon, P., Thompson, G.E. and Habazaki, H. (2006) *Electrochim. Acta*, **52**, 681–687.

359 Siejka, J. and Ortega, C. (1977) *J. Electrochem. Soc.*, **124**, 883–891.

360 Crossland, A.C., Habazaki, H., Shimizu, K., Skeldon, P., Thompson, G.E., Wood, G.C., Zhou, X. and Smith, C.J.E. (1999) *Corros. Sci.*, **41**, 1945–1954.

361 Shimizu, K., Habazaki, H. and Skeldon, P. (2002) *Electrochim. Acta*, **47**, 1225–1228.

362 Zhuravlyova, E., Iglesias-Rubianes, L., Pakes, A., Skeldon, P., Thompson, G.E., Zhou, X., Quance, T., Graham, M.J., Habazaki, H. and Shimizu, K. (2002) *Corros. Sci.*, **44**, 2153–2159.

363 Chu, S.Z., Wada, K., Inoue, S. and Todoroki, S. (2002) *J. Electrochem. Soc.*, **149**, B321–B327.

364 Patermarakis, G., Lenas, P., Karavassilis, Ch. and Papayiannis, G. (1991) *Electrochim. Acta*, **36**, 709–725.

365 Patermarakis, G. (1996) *Electrochim. Acta*, **41**, 2601–2611.

366 Patermarakis, G. and Papandreadis, N. (1993) *Electrochim. Acta*, **38**, 2351–2361.

367 Patermarakis, G. and Tzouvelekis, D. (1994) *Electrochim. Acta*, **39**, 2419–2429.

368 Patermarakis, G. and Moussoutzanis, K. (1995) *J. Electrochem. Soc.*, **142**, 737–743.

369 Patermarakis, G. (1998) *J. Electroanal. Chem.*, **447**, 25–41.

370 Patermarakis, G. and Moussoutzanis, K. (2001) *Corros. Sci.*, **43**, 1433–1464.

371 Patermarakis, G. and Moussoutzanis, K. (2003) *Chem. Eng. Commun.*, **190**, 1018–1040.

372 Patermarakis, G. and Moussoutzanis, K. (2002) *Corros. Sci.*, **44**, 1737–1753.

373 Patermarakis, G. and Moussoutzanis, K. (2002) *J. Solid State Electrochem.*, **6**, 475–484.

374 Patermarakis, G. and Moussoutzanis, K. (2005) *J. Solid State Electrochem.*, **9**, 205–233.

375 Patermarakis, G. and Masavetas, K. (2006) *J. Electroanal. Chem.*, **588**, 179–189.

376 Patermarakis, G. and Moussoutzanis, K. (1995) *Electrochim. Acta*, **40**, 699–708.

377 Patermarakis, G., Moussoutzanis, K. and Chandrinos, J. (2001) *J. Solid State Electrochem.*, **6**, 39–54.

378 Patermarakis, G., Moussoutzanis, K. and Chandrinos, J. (2001) *J. Solid State Electrochem.*, **6**, 71–72.

379 Heber, K. (1978) *Electrochim. Acta*, **23**, 127–133.

380 Heber, K. (1978) *Electrochim. Acta*, **23**, 135–139.

381 Wada, K., Shimohira, T., Yamada, M. and Baba, N. (1986) *J. Mater. Sci.*, **21**, 3810–3816.

382 Morlidge, J.R., Skeldon, P., Thompson, G.E., Habazaki, H., Shimizu, K. and Wood, G.C. (1999) *Electrochim. Acta*, **44**, 2423–2435.

383 Nelson, J.C. and Oriani, R.A. (1993) *Corros. Sci.*, **34**, 307–326.

384 Jessensky, O., Müller, F. and Gösele, U. (1998) *Appl. Phys. Lett.*, **72**, 1173–1175.

385 Ba, L. and Li, W.S. (2000) *J. Phys. D: Appl. Phys.*, **33**, 2527–2531.

386 Palibroda, E. (1984) *Surf. Technol.*, **23**, 353–365 (in French).

387 Palibroda, E., Lupsan, A., Pruneanu, S. and Savos, M. (1995) *Thin Solid Films*, **256**, 101–105.

388 Shimizu, K. and Tajima, S. (1979) *Electrochim. Acta*, **24**, 309–311.

389 Shimizu, K., Brown, G.M., Kobayashi, K., Thompson, G.E. and Wood, G.C. (1993) *Corros. Sci.*, **34**, 1853–1857.

390 Zhang, L., Cho, H.S., Li, F., Metzger, R.M. and Doyle, W.D. (1998) *J. Mater. Sci. Lett.*, **17**, 291–294.

391 Makushok, Yu.E., Parkhutik, V.P., Martinez-Duart, J.M. and Albella, J.M. (1994) *J. Phys. D: Appl. Phys.*, **27**, 661–669.

392 Parkhutik, V.P., Albella, J.M., Makushok, Yu.E., Montero, I., Martinez-Duart, J.M. and Shershulskii, V.I. (1990) *Electrochim. Acta*, **35**, 955–960.

393 Wu, H., Zhang, X. and Hebert, K.R. (2000) *J. Electrochem. Soc.*, **147**, 2126–2132.

394 Hebert, K.R. (2001) *J. Electrochem. Soc.*, **148**, B236–B242.

395 Huang, R. and Hebert, K.R. (2004) *J. Electroanal. Chem.*, **565**, 103–114.

396 Randon, J., Mardilovich, P.P., Govyadinov, A.N. and Paterson, R. (1995) *J. Colloid Interface Sci.*, **169**, 335–341.

397 Singaraju, P., Venkat, R., Kanakala, R. and Das, B. (2006) *Eur. Phys. J. Appl. Phys.*, **35**, 107–111.

398 Singh, G.K., Golovin, A.A., Aranson, I.S. and Vinokur, V.M. (2005) *Europhys. Lett.*, **70**, 836–842.

399 Pan, H., Lin, J., Feng, Y. and Gao, H. (2004) *IEEE Trans. Nanotechnol.*, **3**, 462–467.

400 Aroutiounian, V.M. and Ghulinyan, M.Zh. (2000) *Modern Phys. Letters B*, **14**, 39–46.

401 Leppänen, T., Karttunen, M., Barrio, R.A. and Kaski, K. (2004) *Brazil. J. Phys.*, **34**, 368–372.

402 Boissonade, J., Dulos, E. and De Kepper, P. (1995) *Chemical Waves and Patterns* (eds R. Kapral and K. Showalter), Kluwer Academic Publishers, pp. 221–268.

403 Li, A-P., Müller, F., Birner, A., Nielsch, K. and Gösele, U. (1998) *J. Appl. Phys.*, **84**, 6023–6026.

404 Vrublevsky, I., Parkoun, V., Sokol, V., Schreckenbach, J. and Marx, G. (2004) *Appl. Surf. Sci.*, **222**, 215–225.

405 Vrublevsky, I., Parkoun, V., Schreckenbach, J. and Marx, G. (2003) *Appl. Surf. Sci.*, **220**, 51–59.

406 Takahashi, H. and Nagayama, M. (1978) *Corros. Sci.*, **18**, 911–925.

407 Sulka, G.D., Stroobants, S., Moshchalkov, V., Borghs, G. and Celis, J-P. (2002) *J. Electrochem. Soc.*, **149**, D97–D103.

408 Nagayama, M. and Tamura, K. (1967) *Electrochim. Acta*, **12**, 1097–1107.

409 Sulka, G.D., Stroobants, S., Moshchalkov, V., Borghs, G. and Celis, J-P. (2002) *Bulletin du Cercle d'Etudes des Métaux*, **17**, P1/1-8.

410 Masuda, H., Kanezawa, K. and Nishio, K. (2002) *Chem. Lett.*, 1218–1219.

411 Shingubara, S., Murakami, Y., Morimoto, K. and Takahagi, T. (2003) *Surf. Sci.*, **532–535**, 317–323.

412 Iwasaki, T. and Den, T. (2002) Patent US 6 476 409 B2.

413 Aiba, T., Nojiri, H., Motoi, T., Den, T. and Iwasaki, T. (2003) Patent US 6 541 386 B2.

414 Liu, C.Y., Datta, A. and Wang, Y.L. (2001) *Appl. Phys. Lett.*, **78**, 120–122.

415 Peng, C.Y., Liu, C.Y., Liu, N.W., Wang, H. H., Datta, A. and Wang, Y.L. (2005) *J. Vac. Sci. Technol. B*, **23**, 559–562.

416 Sun, Z. and Kim, H.K. (2002) *Appl. Phys. Lett.*, **81**, 3458–3460.

417 Liu, N.W., Datta, A., Liu, C.Y. and Wang, Y.L. (2003) *Appl. Phys. Lett.*, **82**, 1281–1283.

418 Cojocaru, C.S., Padovani, J.M., Wade, T., Mandoli, C., Jaskierowicz, G., Wegrowe, J.E., Fontcuberta i Morral, A. and Pribat, D. (2005) *Nano Lett.*, **5**, 675–680.

419 Li, A-P., Müller, F., Birner, A., Nielsch, K. and Gösele, U. (1999) *Adv. Mater.*, **11**, 483–486.

420 Masuda, H., Yamada, H., Satoh, M., Asoh, H., Nakao, M. and Tamamura, T. (1997) *Appl. Phys. Lett.*, **71**, 2770–2772.

421 Asoh, H., Nishio, K., Nakao, M., Yokoo, A., Tammamura, T. and Masuda, H. (2001) *J. Vac. Sci. Technol. B*, **19**, 569–572.

422 Masuda, H., Yotsuya, M., Asano, M., Nishio, K., Nakao, M., Yakoo, A. and Tamamura, T. (2001) *Appl. Phys. Lett.*, **78**, 826–828.

423 Asoh, H., Nishio, K., Nakao, M., Tammamura, T. and Masuda, H. (2001) *J. Electrochem. Soc.*, **148**, B152–B156.

424 Asoh, H., Ono, S., Hirose, T., Nakao, M. and Masuda, H. (2003) *Electrochim. Acta*, **48**, 3171–3174.

425 Asoh, H., Ono, S., Hirose, T., Takatori, I. and Masuda, H. (2004) *Jpn. J. Appl. Phys.*, **43** (9A), 6342–6346.

426 Masuda, H. (2001) *Electrochemistry*, **69**, 879–883 (in Japanese).

427 Masuda, H., Asoh, H., Watanabe, M., Nishio, K., Nakao, M. and Tamamura, T. (2001) *Adv. Mater.*, **13**, 189–192.

428 Masuda, H., Abe, A., Nakao, M., Yokoo, A., Tamamura, T. and Nishio, K. (2003) *Adv. Mater.*, **15**, 161–164.

429 Matsumoto, F., Harada, M., Nishio, K. and Masuda, H. (2005) *Adv. Mater.*, **17**, 1609–1612.

430 Choi, J., Nielsch, K., Reiche, M., Wehrspohn, R.B. and Gösele, U. (2003) *J. Vac. Sci. Technol. B*, **21**, 763–766.

431 Choi, J., Wehrspohn, R.B. and Gösele, U. (2003) *Adv. Mater.*, **15**, 1531–1534.

432 Choi, J., Wehrspohn, R.B. and Gösele, U. (2005) *Electrochim. Acta*, **50**, 2591–2595.

433 Matsui, Y., Nishio, K. and Masuda, H. (2005) *Jpn. J. Appl. Phys.*, **44**, 7726–7728.

434 Lee, W., Ji, R., Ross, C.A., Gösele, U. and Nielsch, K. (2006) *Small*, **2**, 978–982.

435 Yasui, K., Nishio, K., Nunokawa, H. and Masuda, H. (2005) *J. Vac. Sci. Technol. B*, **23**, L9–L12.

436 Nishio, K., Fukushima, T. and Masuda, H. (2006) *Electrochem. Solid-State Lett.*, **9**, B39–B41.

437 Masuda, H., Matsui, Y., Yotsuya, M., Matsumoto, F. and Nishio, K. (2004) *Chem. Lett.*, **33**, 584–585.

438 Matsui, Y., Nishio, K. and Masuda, H. (2006) *Small*, **2**, 522–525.

439 Asoh, H. and Ono, S. (2005) *Appl. Phys. Lett.*, **87**, 103102/1-3.

440 Zhao, X., Jiang, P., Xie, S., Feng, J., Gao, Y., Wang, J., Liu, D., Song, L., Liu, L., Dou, X., Luo, S., Zhang, Z., Xiang, Y., Zhou, W. and Wang, G. (2006) *Nanotechnology*, **17**, 35–39.

441 Terryn, H., Vereecken, J. and Landuyt, J. (1990) *Trans. IMF*, **68**, 33–37.

442 Fratila-Apachitei, L.E., Terryn, H., Skeldon, P., Thompson, G.E., Duszczyk, J. and Katgerman, L. (2004) *Electrochim. Acta*, **49**, 1127–1140.

443 Jessensky, O., Müller, F. and Gösele, U. (1998) *J. Electrochem. Soc.*, **145**, 3735–3740.

444 Nagayama, M., Tamura, K. and Takahashi, H. (1970) *Corros. Sci.*, **10**, 617–627.

445 Da Silva, M.F., Shimizu, K., Kobayashi, K., Skeldon, P., Thompson, G.E. and Wood, G.C. (1995) *Corros. Sci.*, **37**, 1511–1514.

446 van den Brand, J., Snijders, P.C., Sloof, W.G., Terryn, H. and de Witt, J.W.H. (2004) *J. Phys. Chem. B***108**, 6017–6024.

447 Wang, Y-L., Tseng, W-T. and Chang, S-Ch. (2005) *Thin Solid Films*, **474**, 36–43.

448 Jagminienė, A., Valinčius, G., Riaukaitė, A. and Jagminas, A. (2005) *J. Cryst. Growth*, **274**, 622–631.

449 Holló, M.Gy. (1960) *Acta Metall.*, **8**, 265–268.

450 Shimizu, K., Kobayashi, K., Skeldon, P., Thompson, G.E. and Wood, G.C. (1997) *Corros. Sci.*, **39**, 701–718.

451 Wu, M.T., Leu, I.C. and Hon, M.H. (2002) *J. Vac. Sci. Technol. B*, **20**, 776–782.

452 Ricker, R.E., Miller, A.E., Yue, D-F., Banerjee, G. and Bandyopadhyay, S. (1996) *J. Electron. Mater.*, **25**, 1585–1592.

453 Bandyopadhyay, S., Miller, A.E., Chang, H.C., Banerjee, G., Yuzhakov, V., Yue, D-F., Ricker, R.E., Jones, S., Eastman, J.A., Baugher, E. and Chandrasekhar, M. (1996) *Nanotechnology*, **7**, 360–371.

454 Konovalov, V.V., Zangari, G. and Metzger, R.M. (1999) *Chem. Mater.*, **11**, 1949–1951.

455 Yuzhakov, V.V., Takhistov, P.V., Miller, A. E. and Chang, H-Ch. (1999) *Chaos*, **9**, 62–77.

456 Kong, L-B., Huang, Y., Guo, Y. and Li, H-L. (2005) *Mater. Lett.*, **59**, 1656–1659.

457 Liu, H.W., Guo, H.M., Wang, Y.L., Wang, Y.T., Shen, C.M. and Wei, L. (2003) *Appl. Surf. Sci.*, **219**, 282–289.

458 Miney, P.G., Colavita, P.E., Schiza, M.V., Priore, R.J., Haibach, F.G. and Myrick, M.L. (2003) *Electrochem. Solid-State Lett.*, **6**, B42–B45.

459 Inoue, S., Chu, S-Z., Wada, K., Li, D. and Haneda, H. (2003) *Sci. Technol. Adv. Mater.*, **4**, 269–276.

460 Chu, S.Z., Wada, K., Inoue, S. and Todoroki, S. (2003) *Surf. Coat. Technol.*, **169–170**, 190–194.

461 Chu, S.Z., Wada, K., Inoue, S. and Todoroki, S. (2003) *Electrochim. Acta*, **48**, 3147–3153.

462 Chu, S.Z., Wada, K., Inoue, S., Hishita, S-ichi. and Kurashima, K. (2003) *J. Phys. Chem. B*, **107**, 10180–10184.

463 Chu, S-Z., Inoue, S., Hishita, S-ichi. and Kurashima, K. (2004) *J. Phys. Chem. B*, **108**, 5582–5587.

464 Chu, S.Z., Inoue, S., Wada, K. and Hishita, S. (2004) *J. Electrochem. Soc.*, **151**, C38–C44.

465 Chu, S.Z., Inoue, S., Wada, K. and Kurashima, K. (2005) *Electrochim. Acta*, **51**, 820–826.

466 Chu, S.Z., Inoue, S., Wada, K., Kanke, Y. and Kurashima, K. (2005) *J. Electrochem. Soc.*, **152**, C42–C47.

467 Kemell, M., Färm, E., Leskelä, M. and Ritala, M. (2006) *Phys. Stat. Sol. A*, **203**, 1453–1458.

468 Rabin, O., Herz, P.R., Lin, Y-M., Akinwande, A.I., Cronin, S.B. and Dresselhaus, M.S. (2003) *Adv. Funct. Mater.*, **13**, 631–638.

469 Crouse, D., Lo, Yu-Hwa Miller, A.D. and Crouse, M. (2000) *Appl. Phys. Lett.*, **76**, 49–51.

470 Asoh, H., Matsuo, M., Yoshihama, M. and Ono, S. (2003) *Appl. Phys. Lett.*, **83**, 4408–4410.

471 Choi, J., Sauer, G., Göring, P., Nielsch, K., Wehrspohn, R.B. and Gösele, U. (2003) *J. Mater. Chem.*, **13**, 1100–1103.

472 Toh, C-S., Kayes, B.M., Nemanick, E.J. and Lewis, N.S. (2004) *Nano Lett.*, **4**, 767–770.

473 Pu, L., Shi, Y., Zhu, J.M., Bao, X.M., Zhang, R. and Zheng, Y.D. (2004) *Chem. Commun.*, 942–943.

474 Le Paven-Thivet, C., Fusil, S., Aubert, P., Malibert, C., Zozime, A. and Houdy, Ph. (2004) *Thin Solid Films*, **446**, 147–154.

475 Myung, N.V., Lim, J., Fleurial, J-P., Yun, M., West, W. and Choi, D. (2004) *Nanotechnology*, **15**, 833–838.

476 Wu, M.T., Leu, I.C., Yen, J.H. and Hon, M.H. (2004) *Electrochem. Solid-State Lett.*, **7**, C61–C63.

477 Shiraki, H., Kimura, Y., Ishii, H., Ono, S., Itaya, K. and Niwano, M. (2004) *Appl. Surf. Sci.*, **237**, 369–373.

478 Chen, Z. and Zhang, H. (2005) *J. Electrochem. Soc.*, **152**, D227–D231.

479 Kokonou, M., Nassiopoulou, A.G., Giannakopoulos, K.P. and Boukos, N. (2005) *J. Phys.: Conference Series*, **10**, 159–162.

480 Mei, Y.F., Wu, X.L., Qiu, T., Shao, X.F., Siu, G.G. and Chu, P.K. (2005) *Thin Solid Films*, **492**, 66–70.

481 Kimura, Y., Shiraki, H., Ishibashi, K-I., Ishii, H., Itaya, K. and Niwano, M. (2006) *J. Electrochem. Soc.*, **153**, C296–C300.

482 Yang, Y., Chen, H., Mei, Y., Chen, J., Wu, X. and Bao, X. (2002) *Solid State Commun.*, **123**, 279–282.

483 Xu, C-L., Li, H., Zhao, G-Y. and Li, H-L. (2006) *Mater. Lett.*, **60**, 2335–2338.

484 Xu, C-L., Li, H., Xue, T. and Li, H-L. (2006) *Scripta Mater.*, **54**, 1605–1609.

485 Mei, Y.F., Wu, X.L., Shao, X.F., Siu, G.G. and Bao, X.M. (2003) *Europhys. Lett.*, **62**, 595–599.

486 Briggs, E.P., Walpole, A.R., Wilshaw, P.R., Karlsson, M. and Pålsgård, E. (2004) *J. Mater. Sci. Mater. Med.*, **15**, 1021–1029.

487 Yasui, K., Sakamoto, Y., Nishio, K. and Masuda, H. (2005) *Chem. Lett.*, **34**, 342–343.

488 Zhou, H.Y., Qu, S.C., Wang, Z.G., Liang, L.Y., Cheng, B.C., Liu, J.P. and Peng, W.Q. (2006) *Mater. Sci. Semicond. Process.*, **9**, 337–340.

489 Yakovlev, N.M., Yakovlev, A.N. and Denisov, A.I. (2003) *Investigated in Russia*, **6**, 673–582 (in Russian).

490 Garcia-Vergara, S.J., El Khazmi, K., Skeldon, P. and Thompson, G.E. (2006) *Corros. Sci.*, **48**, 2937–2946.

491 Yoo, B-Y., Hendricks, R.K., Ozkan, M. and Myung, N.V. (2006) *Electrochim. Acta*, **51**, 3543–3550.

492 Masuda, H., Hesegwa, F. and Ono, S. (1997) *J. Electrochem. Soc.*, **144**, L127–L130.

493 Li, A-P., Müller, F., Birner, A., Nielsch, K. and Gösele, U. (1999) *J. Vac. Sci. Technol. A*, **17**, 1428–1431.

494 Masuda, H., Nagae, M., Morikawa, T. and Nishio, K. (2006) *Jpn. J. Appl. Phys.*, **45**, L406–L408.

495 Shingubara, S., Okino, O., Sayama, Y., Sakaue, H. and Takahagi, T. (1997) *Jpn. J. Appl. Phys.*, **36**, 7791–7795.

496 Almasi Kashi, M. and Ramazani, A. (2005) *J. Phys. D: Appl. Phys.*, **38**, 2396–2399.

497 Masuda, H., Yada, K. and Osaka, A. (1998) *Jpn. J. Appl. Phys.*, **37**, L1340–L1342.

498 Li, A.P., Müller, F. and Gösele, U. (2000) *Electrochem. Solid State Lett.*, **3**, 131–134.

499 Lee, W., Ji, R., Gösele, U. and Nielsch, K. (2006) *Nature Mat.*, **5**, 741–747.

500 Masuda, H. and Satoh, M. (1996) *Jpn. J. Appl. Phys.*, **35**, L126–L129.

501 Zhao, Y., Chen, M., Zhang, Y., Xu, T. and Liu, W. (2005) *Mater. Lett.*, **59**, 40–43.

502 Schneider, J.J., Engstler, J., Budna, K.P., Teichert, Ch. and Franzka, S. (2005) *Eur. J. Inorg. Chem.*, 2352–2359.

503 Yuan, J.H., Chen, W., Hui, R.J., Hu, Y.L. and Xia, X.H. (2006) *Electrochim. Acta*, **51**, 4589–4595.

504 Zhou, W.Y., Li, Y.B., Liu, Z.Q., Tang, D.S., Zou, X.P. and Wang, G. (2001) *Chin. Phys.*, **10**, 218–222.

505 Suh, J.S. and Lee, J.S. (1999) *Appl. Phys. Lett.*, **75**, 2047–2049.

506 Yan, J., Rama Rao, G.V., Barela, M., Brevnov, D.A., Jiang, Y., Xu, H., López, G.P. and Atanassov, P.B. (2003) *Adv. Mater.*, **15**, 2015–2018.

507 Ding, G.Q., Zheng, M.J., Xu, W.L. and Shen, W.Z. (2005) *Nanotechnology*, **16**, 1285–1289.

508 Hou, K., Tu, J.P. and Zhang, X.B. (2002) *Chin. Chem. Lett.*, **13**, 689–692.

509 Ono, T., Konoma, Ch., Miyashita, H., Kanaori, Y. and Esashi, M. (2003) *Jpn. J. Appl. Phys. Part 1*, **42** (6B), 3867–3870.

510 Nielsch, K., Castaño, F.J., Ross, C.A. and Krishnan, R. (2005) *J. Appl. Phys.*, **98**, 034318/1-6.

511 Ding, G.Q., Shen, W.Z., Zheng, M.J. and Zhou, Z.B. (2006) *Nanotechnology*, **17**, 2590–2594.

512 Brändli, Ch., Jaramillo, T.F., Ivanovskaya, A. and McFarland, E.W. (2001) *Electrochim. Acta*, **47**, 553–557.

513 Ono, S., Takeda, K. and Masuko, N. (2000–2001) *ATB Metall.*, **40/41**, 398–403.

514 Sadasivan, V., Richter, C.P., Menon, L. and Williams, P.F. (2005) *AIChE J.*, **51**, 649–655.

515 Bocchetta, P., Sunseri, C., Chiavarotti, G. and Quarto, F.D. (2003) *Electrochim. Acta*, **48**, 3175–3183.

516 Wang, H. and Wang, H-W. (2004) *Trans. Nonferrous Met. Soc. China*, **14**, 166–169.

517 Shimizu, K., Alwitt, R.S. and Liu, Y. (2000) *J. Electrochim. Soc.*, **147**, 1388–1392.

518 Masuda, H. and Fukuda, K. (1995) *Science*, **268**, 1466–1468.

519 Ghorbani, M., Nasirpouri, F., Iraji zad, A. and Saedi, A. (2006) *Mater. Design*, **27**, 983–988.

520 Yu, W.H., Fei, G.T., Chen, X.M., Xue, F.H. and Xu, X.J. (2006) *Phys. Lett. A*, **350**, 392–395.

521 da Fontoura Costa, L., Riveros, G., Gómez, H., Cortes, A., Gilles, M., Dalchiele, E.A. and Marotti, R.E. (2005) *Cond-mat/0504573v*, 11–12.

522 Sui, Y-Ch. and Saniger, J.M. (2001) *Mater. Lett.*, **48**, 127–136.

523 Xu, X.J., Fei, G.T., Zhu, L.Q. and Wang, X.W. (2006) *Mater. Lett.*, **60**, 2331–2334.

524 Rehn, L.E., Kestel, B.J., Baldo, P.M., Hiller, J., McCormick, A.W. and Birchter, R.C. (2003) *Nuc. Instrum. Meth. Phys. Res. B*, **206**, 490–494.

525 Wehrspohn, R.B., Li, A.P., Nielsch, K., Müller, F., Erfurth, W. and Gösele U. (2000) in *Oxide Films* (eds K.R. Hebert R.S. Lillard and B.R. MacDougall), PV-2000-4, Toronto, Canada, Spring, pp. 271–282.

526 Wehrspohn, R.B., Nielsch, K., Birner, A., Schilling, J., Müller, F., Li, A-P. and Gösele, U. (2001) in *Pits and Pores II: Formation Properties and Significance for Advanced Materials* (eds P. Schumki D.J. Lockwood, Y.H. Ogata and H.S. Isaacs), PV 2000-25, Phoenix, Arizona, Fall 2000, pp. 168–179.

527 Choi, D.H., Lee, P.S., Hwang, W., Lee, K.H. and Park, H.C. (2006) *Curr. Appl. Phys.*, **6S1**, e125–e129.

528 Xu, T., Zangari, G. and Metzger, R.M. (2002) *Nano Lett.*, **2**, 37–41.

529 Choi, J., Sauer, G., Nielsch, K., Wehrspohn, R.B. and Gösele, U. (2003) *Chem. Mater.*, **15**, 776–779.

530 Das, B. and Garman, Ch. (2006) *Microelectron. J.*, **37**, 695–699.

531 Tang, M., He, J., Zhou, J. and He, P. (2006) *Mater. Lett.*, **60**, 2098–2100.

532 Stein, N., Rommelfangen, M., Hody, V., Johann, L. and Lecuire, J.M. (2002) *Electrochim. Acta*, **47**, 1811–1817.

533 Brevnov, D.A., Rama Rao, G.V., López, G. P. and Atanassov, P.B. (2004) *Electrochim. Acta*, **49**, 2487–2494.

534 Lefeuvre, O., Pang, W., Zinin, P., Comins, J.D., Every, A.G., Briggs, G.A.D., Zeller, B.D. and Thompson, G.E. (1999) *Thin Solid Films*, **350**, 53–58.

535 Girginov, A., Popova, A., Kanazirski, I. and Zahariev, A. (2006) *Thin Solid Films*, **515**, 1548–1551.

536 Jagminas, A., Kurtinaitienė, M., Angelucci, R. and Valinčius, G. (2006) *Appl. Surf. Sci.*, **252**, 2360–2367.

537 Vrublevsky, I., Parkoun, V., Schreckenbach, J. and Goedel, W.A. (2006) *Appl. Surf. Sci.*, **252**, 5100–5108.

538 Vrublevsky, I., Parkoun, V., Sokol, V. and Schreckenbach, J. (2004) *Appl. Surf. Sci.*, **236**, 270–277.

539 Furneaux, R.C., Rigby, W.R. and Davidson, A.P. (1989) *Nature*, **337**, 147–149.

540 Nielsch, K., Müller, F., Li, A.P. and Gösele, U. (2000) *Adv. Mater.*, **12**, 582–586.

541 Girginov, A.A., Zahariev, A.S. and Klein, E. (2002) *J. Mater. Sci.: Mater. Electron.*, **13**, 543–548.

542 Zahariev, A. and Girginov, A. (2003) *Bull. Mater. Sci.*, **26**, 349–353.

543 Girginov, A., Kanazirski, I., Zahariev, A. and Popova, A. (2004) *Bull. Electrochem.*, **20**, 103–106.

544 Girginov, A., Zahariev, A., Kanazirski, I. and Tzvetkoff, T. (2004) *Bull. Electrochem.*, **20**, 405–407.

545 Girginov, A.A., Zahariev, A.S. and Machakova, M.S. (2002) *Mater. Chem. Phys.*, **76**, 274–278.

546 Liang, J., Chik, H. and Xu, J. (2002) *IEEE J. Selected Topics Quant. Electron.*, **8**, 998–1008.

547 Shimizu, T., Nagayanagi, M., Ishida, T., Sakata, O., Oku, T., Sakaue, H., Takahagi, T. and Shingubara, S. (2006) *Electrochem. Solid-State Lett.*, **9**, J13–J16.

548 Masuda, H., Yasui, K. and Nishio, K. (2000) *Adv. Mater.*, **12**, 1031–1033.

549 Park, S.K., Noh, J.S., Chin, W.B. and Sung, D.D. (2007) *Curr. Appl. Phys.*, **7**, 180–185.

550 Zhao, H., Jiang, Z., Zhang, Z., Zhai, R. and Bao, X. (2006) *Chinese J. Catalysis*, **27**, 381–385 (in Chinese).

551 Kordás, K., Tóth, G., Levoska, J., Huuhtanen, M., Keiski, R., Härkönen, M., George, T.F. and Vähäkangas, J. (2006) *Nanotechnology*, **17**, 1459–1463.

552 Pang, Y.T., Meng, G.W., Fang, Q. and Zhang, L.D. (2003) *Nanotechnology*, **14**, 20–24.

553 Xu, X.J., Fei, G.T., Wang, X.W., Jin, Z., Yu, W.H. and Zhang, L.D. (2007) *Mater. Lett.*, **61**, 19–22.

554 Sander, M.S. and Tan, L-S. (2003) *Adv. Funct. Mater.*, **13**, 393–397.

555 Pan, S.L., Zeng, D.D., Zhang, H.L. and Li, H.L. (2000) *Appl. Phys. A*, **70**, 637–640.

556 Evans, P., Hendren, W.R., Atkinson, R., Wurtz, G.A., Dickson, W., Zayats, A.V. and Pollard, R.J. (2006) *Nanotechnology*, **17**, 5746–5753.

557 Chaure, N.B., Stamenov, P., Rhen, F.M.F. and Coey, J.M.D. (2005) *J. Magn. Magn. Mater.*, **290–291**, 1210–1213.

558 Yasui, K., Morikawa, T., Nishio, K. and Masuda, H. (2005) *Jpn. J. Appl. Phys.*, **44**, L469–L471.

559 Xu, J. and Xu, Y. (2006) *Mater. Lett.*, **60**, 2069–2072.

560 Pang, Y.T., Meng, G.W., Zhang, Y., Fang, Q. and Zhang, L.D. (2003) *Appl. Phys. A*, **76**, 533–536.

561 Nielsch, K., Wehrespohn, R.B., Barthel, J., Kirschner, J., Gösele, U., Fisher, S.F. and Kronmüller, H. (2001) *Appl. Phys. Lett.*, **79**, 1360–1362.

562 Nielsch, K., Wehrspohn, R.B., Fischer, S. F., Kronmüller, H., Barthel, J., Kirschner, J., Schweinböck, T., Weiss, D. and Gösele, U. (2002) *Mat. Res. Soc. Symp. Proc.*, **705**, Y9.3.1–Y9.3.6.

563 Nielsch, K., Wehrspohn, R.B., Barthel, J., Kirschner, J., Fischer, S.F., Kronmüller, H., Schweinböck, T., Weiss, D. and Gösele, U. (2002) *J. Magn. Magn. Mater.*, **249**, 234–240.

564 Nielsch, K., Hertel, R., Wehrspohn, R.B., Barthel, J., Kirschner, J., Gösele, U.,

Fischer, S.F. and Kronmüller, H. (2002) *IEEE Trans. Magn.*, **38**, 2571–2573.

565 Sauer, G., Brehm, G., Schneider, S., Graener, H., Seifert, G., Nielsch, K., Choi, J., Göring, P., Gösele, U., Miclea, P. and Wehrspohn, R.B. (2006) *Appl. Phys. Lett.*, **88**, 023106/1-3.

566 Kumar, A., Fähler, S., Schlörb, H., Leistner, K. and Schultz, L. (2006) *Phys. Rev. B*, **73**, 064421/1-5.

567 Pang, Y-T., Meng, G-W., Zhang, L-D., Qin, Y., Gao, X-Y., Zhao, A-W. and Fang, Q. (2002) *Adv. Funct. Mater.*, **12**, 719–722.

568 Kim, K., Kim, M. and Cho, S.M. (2006) *Mater. Chem. Phys.*, **96**, 278–282.

569 Vlad, A., Mátéfi-Tempfli, M., Faniel, S., Bayot, V., Melinte, S., Piraux, L. and Mátéfi-Tempfli, S. (2006) *Nanotechnology*, **17**, 4873–4876.

570 Tang, X-T., Wang, G-C. and Shima, M. (2006) *J. Appl. Phys.*, **99**, 033906/1-7.

571 Chaure, N.B. and Coey, J.M.D. (2006) *J. Magn. Magn. Mater.*, **303**, 232–236.

572 Gao, T.R., Yin, L.F., Tian, C.S., Lu, M., Sang, H. and Zhou, S.M. (2006) *J. Magn. Magn. Mater.*, **300**, 471–478.

573 Dahmane, Y., Cagnon, L., Voiron, J., Pairis, S., Bacia, M., Ortega, L., Benbrahim, N. and Kadri, A. (2006) *J. Appl. Phys. D: Appl. Phys.*, **39**, 4523–4528.

574 Fei, X.L., Tang, S.L., Wang, R.L., Su, H.L. and Du, Y.W. (2007) *Solid State Commun.*, **141**, 25–28.

575 Losic, D., Shapter, J.G., Mitchell, J.G. and Voelcker, N.H. (2005) *Nanotechnology*, **16**, 2275–2281.

576 Gu, X., Nie, Ch., Lai, Y. and Lin, Ch. (2006) *Mater. Chem. Phys.*, **96**, 217–222.

577 Ren, X., Huang, X-M. and Zhang, H-H. (2006) *Acta Phys-Chim. Sin.*, **22**, 102–105 (in Chinese).

578 Cao, H., Wang, L., Qiu, Y., Wu, Q., Wang, G., Zhang, L. and Liu, X. (2006) *ChemPhysChem.*, **7**, 1500–1504.

579 Lee, W., Scholz, R., Nielsch, K. and Gösele, U. (2005) *Angew. Chem. Int. Ed.*, **44**, 6050–6054.

580 Nielsch, K., Castaño, F.J., Matthias, S., Lee, W. and Ross, C.A. (2005) *Adv. Eng. Mater.*, **7**, 217–221.

581 Steinhart, M., Jia, Z., Schaper, A.K., Wehrspohn, R.B., Gösele, U. and Wendorff, J.H. (2003) *Adv. Mater.*, **15**, 706–709.

582 Steinhart, M., Wendorff, J.H. and Wehrspohn, R.B. (2003) *Chem. Phys. Chem.*, **4**, 1171–1176.

583 Steinhart, M., Wehrspohn, R.B., Gösele, U. and Wendorff, J.H. (2004) *Agnew. Chem. Int. Ed.*, **43**, 1334–1344.

584 Lee, M., Hong, S. and Kim, D. (2006) *Appl. Phys. Lett.*, **89**, 043120/1-3.

585 Lahav, M., Sehayek, T., Vaskevich, A. and Rubinstein, I. (2003) *Agnew. Chem. Int. Ed.*, **42**, 5576–5579.

586 Wang, W., Li, N., Li, X., Geng, W. and Qiu, S. (2006) *Mater. Res. Bull.*, **41**, 1417–1423.

587 Sung, D.D., Choo, M.S., Noh, J.S., Chin, W.B. and Yang, W.S. (2006) *Bull. Korean Chem. Soc.*, **27**, 1159–1163.

588 Li, Y., Meng, G.W., Zhang, L.D. and Phillipp, F. (2000) *Appl. Phys. Lett.*, **76**, 2011–2013.

589 Ko, E., Choi, J., Okamoto, K., Tak, Y. and Lee, J. (2006) *ChemPhysChem.*, **7**, 1505–1509.

590 Ding, G.Q., Shen, W.Z., Zheng, M.J. and Zhou, Z.B. (2006) *Appl. Phys. Lett.*, **89**, 063113/1-3.

591 Wu, C-T., Ko, F-H. and Hwang, H-Y. (2006) *Microelectron. Eng.*, **83**, 1567–1570.

592 Park, I.H., Lee, J.W. and Chung, C.W. (2006) *Integrated Ferroelectrics*, **78**, 245–253.

593 Fan, H.J., Lee, W., Scholz, R., Dadgar, A., Krost, A., Nielsch, K. and Zacharias, M. (2005) *Nanotechnology*, **16**, 913–917.

594 Masuda, H., Nishio, K. and Baba, N. (1992) *Jpn. J. Appl. Phys.*, **31**, L1775–L1777.

595 Nishio, K., Iwata, K. and Masuda, H. (2003) *Electrochem. Solid-State Lett.*, **6**, H21–H23.

596 Sander, M.S., Côte, M.J., Gu, W., Kile, B.M. and Tripp, C.P. (2004) *Adv. Mater.*, **16**, 2052–2057.

597 Min, H-S. and Lee, J-K. (2006) *Ferroelectics*, **336**, 231–235.

598 Alonso-González, P., Martín-González, M.S., Martín-Sánchez, J., González, Y. and González, L. (2006) *J. Cryst. Growth*, **294**, 168–173.

599 Wang, Y.D., Zang, K.Y. and Chua, S.J. (2006) *J. Appl. Phys.*, **100**, 054306/1-4.

600 Jung, M., Lee, H.S., Park, H.L., Lim, H-J. and Mho, S-I. (2006) *Curr. Appl. Phys.*, **6**, 1016–1019.

601 Jung, M., Lee, H.S., Park, H.L. and Mho, S-I. (2006) *Curr. Appl. Phys.*, **6S1**, e187–e191.

602 Wang, Y., Zang, K., Chua, S., Sander, M.S., Tripathy, S. and Fonstad, C.G. (2006) *J. Phys. Chem. B*, **110**, 11081–11087.

603 Konkonou, M., Nassiopoulou, A.G., Giannakopolous, K.P., Travlos, A., Stoica, T. and Kennou, S. (2006) *Nanotechnology*, **17**, 2146–2151.

604 Ding, G.Q., Zheng, M.J., Xu, W.L. and Shen, W.Z. (2006) *Thin Solid Films*, **508**, 182–185.

605 Nakao, M., Oku, S., Tamamura, T., Yasui, K. and Masuda, H. (1999) *Jpn. J. Appl. Phys.*, **38**, 1052–1055.

606 Sai, H., Fujii, H., Arafune, K., Ohshita, Y., Yamaguchi, M., Kanamori, Y. and Yugami, H. (2006) *Appl. Phys. Lett.*, **88**, *201116/*, 1–3.

607 Wu, C., Shi, J-B., Chen, C-J. and Lin, J-Y. (2006) *Mater. Lett.*, **60**, 3618–3621.

608 Aguilera, A., Jayaraman, V., Sanagapalli, S., Singh, R.S., Jayaraman, V., Sampson, K. and Singh, V.P. (2006) *Solar Energy Mater. Solar Cells*, **90**, 713–726.

609 Yang, W., Wu, Z., Lu, Z., Yang, X. and Song, L. (2006) *Microelectron. Eng.*, **83**, 1971–1974.

610 Varfolomeev, A., Zaretsky, D., Pokalyakin, V., Tereshin, S., Pramanik, S. and Bandyopadhyay, S. (2006) *Appl. Phys. Lett.*, **88**, 113114/1-3.

611 Zhang, X.Y., Xu, L.H., Dai, J.Y., Cai, Y. and Wang, N. (2006) *Mater. Res. Bull.*, **41**, 1729–1734.

612 Zhang, J., Xu, B., Jiang, F., Yang, Y. and Li, J. (2005) *Phys. Lett. A*, **337**, 121–126.

613 Zhu, X., Ma, J., Wang, Y., Tao, J., Zhou, J., Zhao, Z., Xie, L. and Tian, H. (2006) *Mater. Res. Bull.*, **41**, 1584–1588.

614 Yan, H., Zhang, L., Shen, J., Chen, Z., Shi, G. and Zhang, B. (2006) *Nanotechnology*, **17**, 3446–3450.

615 O'Brien, G.A., Quinn, A.J., Iacopino, D., Pauget, N. and Redmond, G. (2006) *J. Mater. Chem.*, **16**, 3237–3241.

616 Shin, H-W., Cho, S.Y., Choi, K-H., Oh, S-L. and Kim, Y-R. (2006) *Appl. Phys. Lett.*, **88**, 263112/1-3.

617 Zhao, L., Yang, W., Ma, Y., Yao, J., Li, Y. and Liu, H. (2003) *Chem. Commun.*, 2442–2443.

618 Yang, S.M., Chen, K.H. and Yang, Y.F. (2005) *Synth. Metals*, **152**, 65–68.

619 Steinhart, M., Wendorff, J.H., Greiner, A., Wehrspohn, R.B., Nielsch, K., Schilling, J., Choi, J. and Gösele, U. (2002) *Science*, **296**, 1997.

620 Niu, Z-W., Li, D. and Yang, Z-Z. (2003) *Chin. J. Polymer Sci.*, **21**, 381–384.

621 Schneider, J.J. and Engstler, J. (2006) *Eur. J. Inorg. Chem.*, 1723–1736.

622 Sun, L., Dai, J., Baker, G.L. and Bruening, M.L. (2006) *Chem. Mater.*, **18**, 4033–4039.

623 Nishio, K., Nakao, M., Yokoo, A. and Masuda, H. (2003) *Jpn. J. Appl. Phys. Part 2*, **42** (1A/B), L83–L85.

624 Yanagishita, T., Nishio, K. and Masuda, H. (2005) *Adv. Mater.*, **17**, 2241–2243.

625 Al-Kaysi, R.O. and Bardeen, Ch.J. (2006) *Chem. Commun.*, 1224–1226.

626 Ravindran, S., Andavan, G.T.S., Tsai, C., Ozkan, C.S. and Hollis, T.K. (2006) *Chem. Commun.*, 1616–1618.

627 Wang, Y., Ye, Ch., Wang, G., Zhang, L., Liu, Y. and Zhao, Z. (2003) *Appl. Phys. Lett.*, **82**, 4253–4255.

628 Piao, Y., Lim, H., Chang, J.Y., Lee, W-Y. and Kim, H. (2005) *Electrochim. Acta*, **50**, 2997–3013.

629 Johansson, A., Widenkvist, E., Lu, J., Boman, M. and Jansson, U. (2005) *Nano Lett.*, **5**, 1603–1606.

630 Wang, W., Wang, S-Y., Gao, Y-L., Wang, K-Y. and Liu, M. (2006) *Mater. Sci. Eng. B*, **133**, 167–171.

631 Kyotani, T., Tsai, L-fu. and Tomita, A. (1996) *Chem. Mater.*, **8**, 2109–2113.

632 Zhang, X.Y., Zhang, L.D., Zheng, M.J., Li, G.H. and Zhao, L.X. (2001) *J. Crystal Growth*, **223**, 306–310.

633 Sui, Y.C., Cui, B.Z., Guardían, R., Acosta, D.R., Martiínez, L. and Perez, R. (2002) *Carbon*, **40**, 1011–1016.

634 Chen, Q-L., Xue, K-H., Shen, W., Tao, F-F., Yin, S-Y. and Xu, W. (2004) *Electrochim. Acta*, **49**, 4157–4161.

635 Yin, A., Tzolov, M., Cardimona, D.A. and Xu, J. (2006) *IEEE Trans. Nanotechnol.*, **5**, 564–567.

636 Wen, S., Jung, M., Joo, O-S. and Mho, S-i. (2006) *Curr. Appl. Phys.*, **6**, 1012–1015.

637 Yu, K., Ruan, G., Ben, Y. and Zou, J.J. (2007) *Mater. Lett.*, **61**, 97–100.

638 Yanagishita, T., Sasaki, M., Nishio, K. and Masuda, H. (2004) *Adv. Mater.*, **16**, 429–432.

639 Masuda, H., Ohya, M., Asoh, H., Nakao, M., Nohtomi, M. and Tamamura, T. (1999) *Jpn. J. Appl. Phys.*, **38**, L1403–L1405.

640 Masuda, H., Ohya, M., Nishio, K., Asoh, H., Nakao, M., Nohtomi, M., Yakoo, A. and Tamamura, T. (2000) *Jpn. J. Appl. Phys.*, **39**, L1039–L1041.

641 Masuda, H., Ohya, M., Asoh, H. and Nishio, K. (2001) *Jpn. J. Appl. Phys.*, **40**, L1217–L1219.

642 Masuda, H., Yamada, M., Matsumoto, F., Yakoyama, S., Mashiko, S., Nakao, M. and Nishio, K. (2006) *Adv. Mater.*, **18**, 213–216.

643 Wehrspohn, R.B. and Schilling, J. (2001) *MRS Bullet.*, August, 623–626.

644 Mikulskas, I., Juodkazis, S., Tomašiunas, R. and Dumas, J.G. (2001) *Adv. Mater.*, **13**, 1574–1577.

645 Choi, J., Schilling, j., Nielsch, K., Hillebrand, R., Reiche, M., Wehrspohn, R.B. and Gösele, U. (2002) *Mat. Res. Soc. Symp. Proc.*, **722**, L5.2.1–L.5.2.6.

646 Choi, J., Luo, Y., Wehrspohn, R.B., Hillebrand, R., Schilling, J. and Gösele, U. (2003) *J. Appl. Phys.*, **94**, 4757–4762.

647 Yanagishita, T., Nishio, K. and Masuda, H. (2006) *Jpn. J. Appl. Phys.*, **45**, L804–L806.

648 Vázquez, M., Hernández-Vélez, M., asenjo, A., Navas, D., Pirota, K., Prida, V., Sánchez, O. and Badonedo, J.L. (2006) *Physica B*, **384**, 36–40.

649 Masuda, H., Hogi, H., Nishio, K. and Matsumoto, F. (2004) *Chem. Lett.*, **33**, 812–813.

650 Lee, W., Alexe, M., Nielsch, K. and Gösele, U. (2005) *Chem. Mater.*, **17**, 3325–3327.

651 Masuda, H., Matsumoto, F. and Nishio, K. (2004) *Electrochemistry*, **72**, 389–394.

652 Masuda, H., Watanabe, M., Yasui, K., Tryk, D., Rao, T. and Fujishima, A. (2000) *Adv. Mater.*, **12**, 444–447.

653 Masuda, H., Yasui, K., Watanabe, H.M., Nishio, K., Nakao, M., Tamamura, T., Rao, T.N. and Fujishima, A. (2001) *Electrochem. Solid State Lett.*, **4**, G101–G103.

654 Matsumoto, F., Nishio, K. and Masuda, H. (2004) *Adv. Mater.*, **16**, 2105–2108.

655 Matsumoto, F., Nishio, K., Miyasaka, T. and Masuda, H. (2004) *Jpn. J. Appl. Phys.*, **43** (5A), L640–L643.

656 Matsumoto, F., Kamiyama, M., Nishio, K. and Masuda, H. (2005) *Jpn. J. Appl. Phys.*, **44**, L355–L358.

657 Grasso, V., Lambertini, V., Ghisellini, P., Valerio, F., Stura, E., Perlo, P. and Nicolini, C. (2006) *Nanotechnology*, **17**, 795–798.

658 Myler, S., Collyer, S.D., Bridge, K.A. and Higson, S.P.J. (2002) *Biosens. Bioelectron.*, **17**, 35–43.

659 Walpole, A.R., Briggs, E.P., Karlsson, M., Pålsgård, E. and Wilshaw, P.R. (2003) *Mat-wiss. u. Werkstofftech.*, **34**, 1064–1068.